

---

Doctoral Dissertations

Student Theses and Dissertations

---

Fall 2020

## Fabrication and characterization of multifunctional composites

Aditya R. Thakur

Follow this and additional works at: [https://scholarsmine.mst.edu/doctoral\\_dissertations](https://scholarsmine.mst.edu/doctoral_dissertations)



Part of the [Aerospace Engineering Commons](#), and the [Mechanical Engineering Commons](#)

**Department: Mechanical and Aerospace Engineering**

---

### Recommended Citation

Thakur, Aditya R., "Fabrication and characterization of multifunctional composites" (2020). *Doctoral Dissertations*. 3113.

[https://scholarsmine.mst.edu/doctoral\\_dissertations/3113](https://scholarsmine.mst.edu/doctoral_dissertations/3113)

This thesis is brought to you by Scholars' Mine, a service of the Missouri S&T Library and Learning Resources. This work is protected by U. S. Copyright Law. Unauthorized use including reproduction for redistribution requires the permission of the copyright holder. For more information, please contact [scholarsmine@mst.edu](mailto:scholarsmine@mst.edu).

FABRICATION AND CHARACTERIZATION OF MULTIFUNCTIONAL  
COMPOSITES

by

ADITYA RAGHVENDRA THAKUR

A DISSERTATION

Presented to the Graduate Faculty of the

MISSOURI UNIVERSITY OF SCIENCE AND TECHNOLOGY

In Partial Fulfillment of the Requirements for the Degree

DOCTOR OF PHILOSOPHY

in

AEROSPACE ENGINEERING

2020

Approved by:

Dr. Xiangyang Dong, Advisor

Dr. Charles S. Wojnar

Dr. Lokeswarappa Dharani

Dr. Frank W. Liou

Dr. Chenglin Wu

© 2020

Aditya Raghvendra Thakur

All Rights Reserved

## PUBLICATION DISSERTATION OPTION

This dissertation consists of the following five articles, formatted in the style used by the Missouri University of Science and Technology:

Paper I, found on pages 7 - 50, has been published in the *International Journal of Fracture* in January 2020.

Paper II, found on pages 51 - 87, has been prepared to be submitted to the *Journal of Manufacturing Science and Engineering*.

Paper III, found on pages 88 - 103, has been published in the *Manufacturing Letters Journal* in October 2020.

Paper IV, found on pages 104 - 117, has been published in the *Multifunctional Materials Journal* in April 2020.

Paper V, found on pages 118 - 169, has been prepared to be submitted to *Additive Manufacturing*.

## ABSTRACT

This study details the research to facilitate fabrication and characterization of novel structural composites reinforced with carbon fibers. Across industries, materials with high performance-to-weight ratio are sought after. Using carbon fibers as secondary phases in these proposed composites, specific characteristics can be tailored in these materials to manufacture strong, lightweight, high performance structures. The first part of the research focused on the improvement in the mechanical properties of the composites using carbon fiber reinforcement. As a part of this study, toughened ceramic composites with predictable failure patterns were produced using carbon fiber inclusions. A closed-form analytical model was developed to enable expedited analyses of various composite designs. A high-speed additive manufacturing process to fabricate high-strength, lightweight structural components using short, long and continuous carbon fiber reinforcement was also established. Therefore, enabling component-level improvement by delivering customizable structures with high strength-to-weight performance at a low cost. The second part of the research expanded this further to a system wide performance-to-weight improvement through the fabrication and characterization of multifunctional composites. As a part of this research multifunctional structural energy composites were additively manufactured with active-conductive material doped polymer matrix cathode and conductive carbon fiber reinforcement as anode. A systematic study conducting mechanical, electrochemical and microstructural analyses helped in establishing the feasibility of the developed composites to facilitate system-level improvements, making them attractive for widespread multifunctional structural applications.

## ACKNOWLEDGMENTS

I would like to convey my gratitude to my advisor Dr. Xiangyang Dong. His enthusiasm and vigor is contagious! His constructive guidance throughout my doctoral study helped me cruise through this rigorous but enlightening course.

I express my heartfelt appreciation to Dr. Charles S. Wojnar and Dr. Chenglin Wu, for their intellectual insight that laid the foundation for my graduate research. Their technical advice and emotional counsel helped me grow professionally and personally.

I appreciate Dr. Lokeswarappa Dharani and Dr. Frank Liou for taking the time to serve on my dissertation committee. Their recommendations and queries were invaluable in polishing my study, and the courses taken with Dr. Dharani were indispensable.

I would also like to extend my appreciation to Dr. Ashok Midha. My interactions with him have been some of my best learning experiences.

I would want to thank my lab partners, particularly, John Pappas and Charng-Yuh Lee who worked with me extensively during my graduate program. I appreciate Getter Vader, especially for assistance with illustrations; and I esteem Yash, Partab and Sarbjit for their support and friendship over the years.

Finally, I would like to thank my family for their love, patience and encouragement. My parents (Raghvendra Thakur & Sangita Thakur) and sister (Shruti Thakur) have always provided me with the moral support that gave me an impetus to earn my Ph.D.

## TABLE OF CONTENTS

	Page
PUBLICATION DISSERTATION OPTION .....	iii
ABSTRACT.....	iv
ACKNOWLEDGMENTS .....	v
LIST OF ILLUSTRATIONS.....	xi
LIST OF TABLES.....	xvii
 SECTION	
1. INTRODUCTION.....	1
 PAPER	
I. A COMPUTATIONALLY EFFICIENT APPROACH FOR PREDICTING TOUGHNESS ENHANCEMENT IN CERAMIC COMPOSITES WITH TAILORED INCLUSION .....	7
ABSTRACT .....	7
1. INTRODUCTION.....	9
2. MIXED MODE STRESS INTENSITY FACTOR OF A KINKED CRACK.....	10
2.1. MODE I STRESS INTENSITY FACTOR ON A STRAIGHT CRACK .....	11
2.2. APPROXIMATE STRESS INTENSITY FACTOR OF A KINKED CRACK .....	12
2.3. INFLUENCE OF A NEARBY INCLUSION ON A STRAIGHT CRACK ....	13
2.4. COMBINED EFFECT OF CRACK KINKING AND INCLUSIONS .....	15
2.5. FINITE ELEMENT VALIDATION FOR FRACTURE INITIATION.....	16
3. FRACTURE PROPAGATION.....	22

3.1. INCREMENTAL CRACK EXTENSION METHOD.....	22
3.2. PHASE-FIELD MODEL.....	24
3.3. SPECIMEN PREPARATION FOR 4-POINT BENDING EXPERIMENTS .....	26
4. DISCUSSION .....	32
4.1. VALIDATION OF PROPOSED APPROACH.....	32
4.2. RELATIVE CRACK LENGTH INCREASE METRIC.....	33
4.3. INFLUENCE OF INCLUSION SEPARATION DISTANCE ON FRACTURE .....	34
4.4. EFFECT OF THE INCLUSION PATTERN ON THE TOUGHNESS .....	37
4.4.1. Crack Guiding using a Rotated Cubic Array. ....	37
4.4.2. Crack Deflection using a Body-centered Cubic Array .....	40
4.4.3. Crack Deflection in a Multi-phase Array.....	42
5. CONCLUSION .....	44
ACKNOWLEDGEMENT.....	47
REFERENCES.....	47
II. A COMPARATIVE STUDY OF EXTRUSION DEPOSITION OF SHORT, LONG, AND CONTINUOUS CARBON FIBER REINFORCED COMPOSITES FOR LARGE-SCALE ADDITIVE MANUFACTURING .....	51
ABSTRACT .....	51
1. INTRODUCTION.....	52
2. EXPERIMENTAL PROCEDURE.....	56
2.1. MATERIAL PREPARATION .....	56
2.2. EXPERIMENTAL SETUP.....	58

2.3. MECHANICAL AND MICROSTRUCTURE CHARACTERIZATION ....	62
3. RESULTS AND DISCUSSION .....	64
3.1. MORPHOLOGY COMPARISON OF THE PRINTED SAMPLES .....	64
3.2. PRINTED SAMPLES.....	66
3.3. MICROSTRUCTURAL CHARACTERIZATION.....	69
3.3.1. Carbon Fiber Distribution.....	69
3.3.2. Carbon Fiber Orientation and Length.....	73
3.4. DEMONSTRATION OF 3D PRINTED CARBON FIBER REINFORCED COMPOSITE STRUCTURES.....	79
4. CONCLUSION .....	80
ACKNOWLEDGEMENT.....	82
REFERENCES.....	82
III. ADDITIVE MANUFACTURING OF 3D STRUCTURAL BATTERY COMPOSITES WITH COEXTRUSION DEPOSITION OF CONTINUOUS CARBON FIBERS.....	88
ABSTRACT .....	88
1. INTRODUCTION.....	89
2. EXPERIMENTAL PROCEDURE.....	90
2.1. 3D STRUCTURAL BATTERY ARCHITECTURE.....	90
2.2. EXPERIMENTAL SETUP.....	93
3. RESULTS AND DISCUSSION .....	95
4. CONCLUSION .....	100
ACKNOWLEDGEMENT.....	100
REFERENCES.....	101

IV. PRINTING WITH 3D CONTINUOUS CARBON FIBER MULTIFUNCTIONAL COMPOSITES VIA UV-ASSISTED COEXTRUSION DEPOSITION .....	104
ABSTRACT .....	104
1. INTRODUCTION.....	105
2. EXPERIMENTAL SETUP .....	106
3. RESULTS AND DISCUSSION .....	109
4. CONCLUSION .....	114
REFERENCES.....	114
V. ADDITIVE MANUFACTURING OF A POLYMER LITHIUM-ION STRUCTURAL BATTERY WITH 3D CONTINUOUS CARBON FIBER ANODE VIA COEXTRUSION DEPOSITION.....	118
ABSTRACT .....	118
1. INTRODUCTION.....	119
2. EXPERIMENTAL PROCEDURE.....	123
2.1. MATERIAL PREPARATION .....	123
2.1.1. Polymer Cathode.....	123
2.1.2. Carbon Fiber Anode and Current Collector.....	128
2.2. EXPERIMENTAL SET-UP .....	129
2.2.1. Electro-grafting Setup for Solid Polymer Electrolyte (SPE) .....	129
2.2.2. Coextrusion Deposition Setup .....	132
2.3. TESTING AND CHARACTERIZATION.....	138
2.3.1. Electrochemical Characterization.....	138
2.3.2. Mechanical Tests .....	138

2.3.3. Microstructural Analyses .....	139
3. RESULTS AND DISCUSSION .....	139
3.1. ELECTRICAL CHARACTERIZATION OF CATHODE MATRIX.....	139
3.2. BATTERY PERFORMANCE CHARACTERIZATION .....	142
3.2.1. Effect of Solvent Volume Ratio on the Electrochemical Performance.....	143
3.2.2. Effect of Binder Weight Percent on the Electrochemical Performance.....	146
3.3. CARBON FIBER CONTENT .....	147
3.4. MECHANICAL PERFORMANCE .....	150
4. MICROSTRUCTURAL ANALYSES.....	153
4.1. POROSITY ANALYSES .....	153
5. CONCLUSIONS .....	159
REFERENCES.....	161
SECTION	
2. CONCLUSIONS AND RECOMMENDATIONS.....	170
BIBLIOGRAPHY .....	175
VITA.....	177

## LIST OF ILLUSTRATIONS

PAPER I	Page
Figure 1. Illustration of (A) the 4-point bending geometry and (B) the geometry of a kinked crack between two inclusions in a specimen subjected to far field mixed loading.....	12
Figure 2. A schematic of the specimen in (A) shows the geometry, loading and boundary conditions for the 4-point bending test, which includes the dimension of the inclusions and kinked crack (in mm).....	18
Figure 3. Comparison between analytical model (lines) and linear elastic finite element simulation (dots) .....	21
Figure 4. Contour plots of the (A) J-integral and (B) kink angle in the preferred direction.....	24
Figure 5. Illustration of specimen fabrication process showing the (A) carbon mixture for inclusions, (B) ZrB <sub>2</sub> powder for matrix, (C) carbon feed rod, (D) ZrB <sub>2</sub> green billet, (E) periodic holes drilled into the green billet, (F) carbon feed rod extruded into filaments, (G) co-sintered ZrB <sub>2</sub> -C billet, (H) sintering schedule, (I) ceramic composite with inclusions, and (J, K) the test specimens cut and notched. ....	28
Figure 6. Images of the (A) experimental set-up, (B) micro-tensile tester equipped with 4-point bending test fixture, (C) specimen with kinked notch and inclusions, and (D) the crack-tip .....	31
Figure 7. (A) Experimental crack paths after complete fracture for varying notch locations. (B) Crack paths from the proposed method, phase field model and experiment. (C) Load vs. load point displacement curve from experiment and phase field model illustrating variation in failure load and subsequently toughness between specimens with centered and off-set notch.....	35
Figure 8. Simulation of (A) crack propagation for different initial crack offset positions and (B) crack length increase versus inclusion separation and offset position predicted from the crack extension method .....	38
Figure 9. Example cubic array of stiff inclusions, denoted by the shaded circles, oriented at an angle $\gamma=7^\circ$ .....	40

Figure 10. (A) Plot of the maximum allowable orientation angle of the inclusions versus relative inclusion radius. (B) Plot of the corresponding relative crack length increase versus relative inclusion radius.....	41
Figure 11. (A) Body-centered cubic array of stiff inclusions used (shaded area) to increase the crack length (blue line). (B) Plot of the relative crack length increase versus relative inclusion radius .....	43
Figure 12. (A) Inclusion arrangement in the multi-phase, cubic composite and resulting crack path. The dark and light shaded circles correspond to the stiff and soft inclusions, respectively. The crack path is denoted by the solid blue line. (B) Plot of relative crack length increase versus inclusion radius for different elastic mismatch ratios .....	46
 PAPER II	
Figure 1. Schematic of the AM setup to fabricate (A) SFRC/pure thermoplastic, (B) LFRC, and (C) CFRC samples.....	59
Figure 2. Schematics of setup used in preparation of continuous carbon fiber reinforced composites.....	61
Figure 3. Three-point bending test set-up with LFRC sample used for demonstration....	62
Figure 4. A direct comparison of additively manufactured (A) pure PLA, (B) SFRC, (C) LFRC, and (D) CFRC samples printed at printing parameters exhibiting acceptable printing resolution and consistent layer deposition.....	65
Figure 5. Measured stress and strain data through three-point bending tests on pure PLA, SFRC, LFRC and CFRC samples.....	66
Figure 6. Comparison of measured flexural strength and modulus between pure PLA, SFRC, LFRC and CFRC samples.....	67
Figure 7. Transverse cross-section of a single deposition layer of the printed (A) SFRC, (B) LFRC, and (C) CFRC samples with highlighted carbon fibers within the PLA matrix.....	70
Figure 8. Distribution mapping of carbon fibers (marked dots) across the transverse cross section with the distribution of fiber dot counts in (A) SFRC, (B) LFRC and (C) CFRC composite deposition. ....	71
Figure 9. Longitudinal cross-section of each deposition layer of the printed (A) SFRC, (B) LFRC, and (C) CFRC samples with a the distribution of carbon fibers (dark phase) within transparent PLA matrix. ....	72

Figure 10. Fiber orientation distribution within the printed (A) SFRC and (B) LFRC samples. ....	74
Figure 11. Fiber length distribution within the printed (A) SFRC and (B) LFRC samples. ....	75
Figure 12. Micrographs illustrating the transverse cross sections of (A) SFRC, (B) LFRC, and (C) CFRC samples with 6% fiber reinforcement. ....	78
Figure 13. Void fraction within the printed fiber reinforced thermoplastic samples for short, long and continuous fiber reinforcement.....	78
Figure 14. A large-scale wing rib structure printed at a deposition rate of 13.3 g/min and a print speed of 200 mm/min.....	80

### PAPER III

Figure 1. Schematics of the 3D structural battery composite architecture .....	91
Figure 2. Schematics of the proposed AM method to print structural battery composites with SPE-coated continuous carbon fibers.....	96
Figure 3. Characterization of the printed samples (A) shows optimization of cathode doped matrix materials; (B) shows capacity and Columbic efficiency of the printed structural battery at a current density of 10 mA/cm <sup>3</sup> at C/2 for 10 cycles; (C) shows flexural strength and modulus measured through 4-point bending tests in comparison of printed cathode matrix and structural battery composite samples (80 mm × 10 mm × 5 mm).....	97
Figure 4. Printed structural battery composites illuminating LEDs with a ring-shaped structure shown in (A) and the schematics of its full battery assembly shown in (B). A similar full battery assembly process has been used for a disc-shaped structure in (C), a triangle structure in (D), and a star-shaped structure in (E).....	99

### PAPER IV

Figure 1. (A) Shows the schematics of the UV-assisted coextrusion deposition of 3D continuous carbon fiber multifunctional composites, as demonstrated by a printed free-standing spiral spring structure in (B), a hollow cylinder structure in (C), and a free-standing tapered spiral spring structure in (D) reinforced with continuous carbon fibers. ....	108
Figure 2. Printed functional parts with continuous carbon fibers.....	110

Figure 3. (A) shows the schematics of 3D continuous carbon fiber structural battery structure; (B) shows a printed functional, full cylindrical structural battery; (C) reveals the cross-section of the printed battery structure; (D) shows a close-up optical microscope image of the sample in (C), demonstrating SPE coated carbon fibers embedded within cathode materials; (E) shows a printed functional full hollow cylindrical battery structure. .... 112

Figure 4. (A) Tensile strength and modulus in comparison of the 3D printed cylindrical structural battery and polymer matrix materials; (B) Capacity and Columbic efficiency of the printed cylindrical structural battery at a current density of  $10 \text{ mA/cm}^3$  for 10 cycles. .... 113

#### PAPER V

Figure 1. Viscosity vs. shear rate for cathode slurry with (A) varying solid load: DMF solvent volume ratio with 25 wt.% binder in the solid load, and (B) varying binder wt.% in the solid load with consistent solid load:DMF solvent volume ratio of 1:4.5. .... 127

Figure 2. (A). Schematics of the set-up for SPE coating on carbon fiber tows, and (B) SEM images comparing uncoated and coated carbon fibers procured through the electro-grafting process. .... 131

Figure 3. Schematic diagram depicting (A) coextrusion deposition of full lithium-ion battery with 3D continuous carbon fiber anode. (B) The cross section of the fabricated concentric structural battery composite with each individual SPE-coated carbon fiber dispersed in cathode matrix working as micro-battery cells. .... 133

Figure 4. Shear stress vs. shear rate for cathode slurries (A) varying solid load:DMF solvent volume ratio with 25 wt.% binder in the solid load, and (B) varying binder wt.% in the solid load with solid load:DMF solvent volume ratio of 1:4.5. .... 136

Figure 5. (A) Schematic image of the cross section of the fabricated structural battery composite, and (B) SEM image of the battery composite, with (C) highlighting the SPE coating on the carbon fiber anode embedded within cathode matrix. .... 137

Figure 6. Resistivity and ionic conductivity measured for the cathode material with varying binder weight percent within the solid load. .... 141

- Figure 7. Capacity and Coulombic efficiency at a current density of  $10 \text{ mA g}^{-1}$  for 100 cycles for a disc shaped battery with solid load composition of  $\text{LiFePO}_4$ :Super-P carbon:Milled short carbon fiber:PVDF at 45:12:18:25 ratio..... 143
- Figure 8. Charging (black circle) and discharging (blue square) capacity of a disc shaped battery with solid load composition of  $\text{LiFePO}_4$ :Super-P carbon:milled short carbon fiber:PVDF at 45:12:18:25 ratio cycled at varying C rates..... 144
- Figure 9. (A) Weight normalized discharge voltage vs. capacity curves of the battery composites printed using cathode slurries with varying viscosities, and (B) the summary of discharge capacities for the battery composites ..... 145
- Figure 10. (A) Weight normalized discharge voltage vs. capacity curves of the battery composites printed using cathode slurries with varying binder, and (B) the summary of discharge capacities for the battery composites ..... 148
- Figure 11. Continuous fiber volume fraction for varying binder weight percent of solid load within the cathode matrix. .... 149
- Figure 12. (A) Measured tensile strength and modulus, and (B) stress vs. strain curve for the the battery composites with varying solvent volume ratio with solid load composition of  $\text{LiFePO}_4$ :Super-P carbon:Milled short carbon fiber:PVDF at 45:12:18:25 ratio by weight..... 151
- Figure 13. (A) Measured tensile strength and modulus, and (B) stress vs. strain curve for the battery composites with varying binder weight percent in the solid load with solvent volume ratio of 1:4.5 ..... 151
- Figure 14. SEM images illustrating the overall deposition and an inset image providing an example of magnified view for the battery composite samples with varying viscosity of (A) 1:3, (B) 1:4 and (C) 1:5 solid load: DMF solvent ratio. .... 154
- Figure 15. SEM images illustrating the overall deposition and inset image providing an example magnified view for the battery composite samples with varying binder percent of (A) 25%, (B) 35%, and (C) 45% within the solid load of the cathode slurry ..... 155
- Figure 16. Comparison of the total porosity area within the battery composite deposition for (A) varying viscosity with solid load composition containing 25% binder by weight, and (B) varying binder percentage at fixed solvent volume ratio of 1:4.5 ..... 156

- Figure 17. Weighted histogram illustrating average changes in pore size distribution within the battery composite deposition for samples with (A) varying viscosity with solid load composition containing 25% binder by weight, and (B) varying binder percentage at fixed solvent volume ratio of 1:4.5..... 158
- Figure 18. (A) Printed disc-shaped structural battery composite assembled with aluminum current collector, illuminating LED, along with (B) triangular and (C) square shaped 3D batteries. (D) The disc-shaped structural battery composite being used as a replacement for CR2032 lithium coin cell battery. .... 160

**LIST OF TABLES**

PAPER I	Page
Table 1. Material properties of the matrix and inclusion materials used in experiments and finite element analysis. ....	23
Table 2. The Euler-Lagrange equations of the potential energy used in the phase-field model. ....	26
Table 3. Constituents of the composite specimens .....	29

## 1. INTRODUCTION

Lightweight materials with high strength and stiffness are highly sought after in aerospace and automotive industries due to their influence on vehicular weight which could offer myriads of benefits, specifically from a performance and economic point of view [1]. Modern fiber reinforced composites, due to their potential for excellent mechanical properties and low density, are being actively studied to address the limitations that the traditional structural materials face while delivering high strength-to-weight performance [2]. In addition to the conventional structural composite materials, tailored multifunctional composites inspired by biological analogues are also being investigated to instill useful combinations of functionalities, simultaneously [3]. These multifunctional composites could assist in delivering system-level improvements in weight-to-functionality performance of the components.

Often in nature, secondary phases and hierarchies in materials have been observed to inculcate multifunctionality [4], [5]. Composite materials of such stripes are studied via experimental, theoretical and numerical analyses to determine the influence of these secondary phases, and to facilitate fabrication of composites with controlled features to derive tailored characteristics. Advancements in material processing and fabrication have enabled monitoring and control of these secondary phases from the macro to nano-scale. As a part of this study, different innovative fabrication approaches were explored to design and manufacture multifunctional composites with a variety of distinct properties. The designed composites were systematically characterized and studied with an intent to enhance and tailor precise characteristics in them.

Specifically, carbon fibers were selected for this study as reinforcement for the composites due to their high strength-to-weight ratio [6], [7], high specific properties [8], and potential multifunctionality [9] owing to their electrical and thermal characteristics [10]–[12]. Such a transformative class of high-performance composites are deemed material-efficient [13]. This efficiency could be further improved through additive manufacturing which assists in shortening the design manufacturing cycle, reduce production costs and improve competitiveness through the ease of use [14]–[16].

The main objective of this research is to address the bottle-neck imposed by the conventional materials and manufacturing approaches that inhibits development in industries requiring customized structures with high strength-to-weight performance. This was addressed through the development and characterization of multiphase composites with tailored inclusion properties which instilled multifunctionality in the resulting composites. Simultaneously, the development of additive manufacturing approaches throughout this research, to fabricate the proposed composites, are intended to aid in producing functional customizable components with intricate geometries at a relatively low cost, material waste, and complexity, compared to the conventional manufacturing approaches.

This dissertation is organized based on five journal publications. As a part of the research conducted in Paper I titled, “A Computationally Efficient Approach for Predicting Toughness Enhancement in Ceramic Composites with Tailored Inclusion”, zirconium diboride ceramic composites with precisely positioned carbon fiber inclusions were fabricated. A closed-form analytical model for the mixed-mode stress intensity factor in such composites with selected inclusion arrangements was developed, which

expedites the analysis for various composite designs. The accuracy of this model was validated by linear elastic fracture mechanics analysis, a phase-field model, as well as experiments. The model was applied to analyze composite inclusion arrangements to study the effect of various material combinations and geometries on the overall toughness of the resulting composite. The results drew correlation between inclusion spacing, sizes and elastic mismatch. These characteristics had a notable influence over the crack propagation direction, which indicates the possibility of increasing the fracture surface area (and thus increasing toughness by increasing the dissipation) by adjusting material and geometric parameters of the inclusion phase. Toughened ceramics with predictable failure patterns require smaller factors of safety [17], [18]. This facilitates cost and weight savings which otherwise are a considerable penalty when using conventional ceramics with uncertain failure strengths.

As a part of the research conducted in Paper II titled, “A Comparative Study of Extrusion Deposition of Short, Long, and Continuous Carbon Fiber Reinforced Composites for Large-Scale Additive Manufacturing”, a large-format, high-speed additive manufacturing process to fabricate fiber reinforced thermoplastics was developed. The feasibility of the process was established by printing carbon fiber reinforced polylactic acid (PLA) samples which have low weight and high directional strength and stiffness. By directly using commercial thermoplastic pellets and continuous fiber tows, inexpensive yet complex high-performance composite structures were manufactured. A comparative study of the samples with continuous and discontinuous fiber reinforcement was conducted with deposition morphology, mechanical performance, nature of reinforcing fibers and prevalence of intra-deposition voids as the

primary focus. Microstructural analyses along with the study of the fiber length and the orientation distribution within the thermoplastic matrix assisted in the characterization of the mechanical behavior of the resulting composites.

As a part of the study detailed in Paper III titled, “Additive Manufacturing of 3D Structural Battery Composites with Coextrusion Deposition of Continuous Carbon Fibers”, the component level strength-to-weight improvement that was secured through carbon fiber reinforced composites, was promoted to the system level improvement by designing and constructing multifunctional thermoplastic composites. Multiaxis coextrusion technique was developed that enabled fabrication of the 3D structural battery composites with customizable form factor. The proposed technique was used to fabricate structural battery composites with continuous carbon fibers coated by solid polymer electrolyte (SPE). The SPE-coated carbon fibers were coextruded with cathode doped thermoplastic matrix. Mechanical and electrochemical characterization of the 3D printed composites demonstrated their potentials in simultaneous electrical energy storage and load bearing. Thus, potentially improving system-wide energy and power densities upon being used as integrated multifunctional structural components. This assists in weight savings as conventional battery packages within systems would typically be of auxiliary nature.

The mechanical and electrochemical performance of the structural energy composite is dictated by the impregnation of the reinforcing conductive fiber (anode). The inherently high viscosity of the thermoplastic binders hinders the impregnation of the fibers [19], [20]. An additive fabrication process that enables coextrusion of continuous fiber reinforced thermoset polymer composite was thus developed as a part of the

research encapsulated in Paper IV titled, “Printing With 3D Continuous Carbon Fiber Multifunctional Composites via UV-Assisted Coextrusion Deposition”. Using conductive continuous carbon fiber allowed incorporation of functionalities in addition to the added strength such as mechanical compliance, support free additive manufacturing and latent structural health monitoring. Using lithium-ion infused monomer coating added to the reinforcing carbon fibers, and active-conductive material doped surrounding thermoset photopolymer, support-free, net-shaped, solid state lithium-ion structural batteries were additively fabricated.

Although the use of thermoset binder within cathode helped in improving the fiber impregnation when compared to the thermoplastic (PLA) binder, there is a limitation to the amount of active and conductive dopants that could be added to the thermoset material. Higher volume of active and conductive dopants is desirable for higher battery performance. However, excessive dopants could render the thermoset binder to be uncurable. As a part of the research conducted in Paper V titled, “Additive Manufacturing of Polymer Lithium-ion Structural Battery with 3D Continuous Carbon Fiber Anode via Coextrusion Deposition”, these limitations associated with the aforementioned additively fabricated thermoplastic and thermoset structural energy composites was addressed. Inadequate fiber impregnation (for thermoplastic cathode matrix) and active-conductive material threshold (for thermoset cathode matrix) was overcome through the use of polyvinylidene fluoride (PVDF), a mechanically weak but electrochemically compliant binder that is used extensively in commercial lithium-ion batteries [21]. This helped in elevating the electrochemical performance of the additively manufactured energy composite, while simultaneously improving the mechanical

performance of the printed structure due to the reinforcing continuous carbon fibers. In addition to the modifications made to the fabrication process, preliminary characterizations were also carried out to establish the feasibility of the proposed composite material. This aided in establishing an additive fabrication approach to manufacture mechanically and electrochemically functional net-shaped, solid state lithium-ion structural batteries with potential applications in the industries where power sources with high energy and power densities are desired. The mechanically adept nature of the energy composite facilitate its usage as a structural component while simultaneously being an energy component, offering potentially significant savings in system-level weight and volume.

**PAPER****I. A COMPUTATIONALLY EFFICIENT APPROACH FOR PREDICTING TOUGHNESS ENHANCEMENT IN CERAMIC COMPOSITES WITH TAILORED INCLUSION**

Aditya R. Thakur <sup>1</sup>, Congjie Wei <sup>2</sup>, Chenglin Wu <sup>2\*</sup>, Jeremy L. Watts <sup>3</sup>, Charles S. Wojnar <sup>4</sup>

<sup>1</sup> Department of Mechanical and Aerospace Engineering, Missouri University of Science and Technology, Rolla, MO 65409

<sup>2</sup> Department of Civil, Architectural, and Environmental Engineering, Missouri University of Science and Technology, Rolla, MO 65409

<sup>3</sup> Department of Materials Science and Engineering, Missouri University of Science and Technology, Rolla, MO 65409

<sup>4</sup> Computational Engineering Division, Lawrence Livermore National Laboratory, Livermore, CA 94550

**ABSTRACT**

Advanced manufacturing techniques such as extrusion based methods have enabled the fabrication of ceramic composites with ordered inclusion phases (i.e. the size and position of the inclusion can be precisely controlled) to improve their overall strength and toughness. Conventional theories, simulation approaches, and experimental methods for analyzing fracture in composites with randomly dispersed inclusion phases (resulting in homogeneous, isotropic effective properties) become inadequate at understanding and designing composites with ordered inclusions for enhancing effective properties such as toughness. In addition, existing methods for analyzing fracture in composites can be

computationally expensive and pose challenges in accurately capturing experimentally observed fracture growth. For example, extended finite element and phase-field methods are computationally expensive in evaluating the large design space of possible inclusion arrangements enabled by the new manufacturing techniques. In this work, a closed-form analytical model for the mixed-mode stress intensity factor in a composite with selected inclusion arrangements is presented, which expedites the analysis for various composite designs. Moreover, the fracture initiation calculation is adapted to approximate crack propagation with computational efficiency. The accuracy of this model for predicting fracture initiation is validated by linear elastic fracture mechanics analysis using the finite element method. The prediction of fracture propagation is validated using a phase-field model, as well as a 4-point bending experiment. Finally, the model is applied to analyze three different composite inclusion arrangements to study the effect of various material combinations and geometries on the overall toughness of the composite; a complete sampling of (and optimization) over the entire design space, however, is beyond the scope of this work. The relative increase in crack length (compared to a homogeneous material) is used as a metric to compare the relative toughness of three different composite designs. Within these designs, using the fast-running approximate method, the effect of the ratio of inclusion radius to inclusion spacing, and the elastic mismatch on the resulting crack length are compared to determine the composite arrangements that result in the greatest toughness enhancement for selected material properties. In particular, a multi-phase cubic array resulted in the greatest toughness enhancement of the designs considered.

*Keywords: Patterned inclusion, Fracture, Ceramic composite, Analytical approximation.*

## 1. INTRODUCTION

Ceramic materials exhibit many useful properties such as high strength, stiffness, melting temperatures, and chemical stability. However, the fundamental problem preventing their widespread use in structural applications is their low fracture toughness. The brittle nature of ceramics renders such structures susceptible to complex crack paths. Thus, the failure of ceramic structures is difficult to predict. As a result, the safety of ceramic structures is often given by probability distribution functions [1, 2]. Uncertainty in the failure strength of such structures requires large safety factors that increase cost, require more material, and increase weight. Due to these issues, a longstanding goal has been to find ways of increasing the toughness of ceramics.

One approach to increase toughness, which is often found in nature, is to create ceramic composites and hierarchical structures [3,4]. This approach has been explored in experiments and theoretical analysis [5–7] to determine how inclusion phases at different scales affect overall strength and toughness. The introduction of secondary phases and hierarchy leads to toughening mechanisms such as crack deflection, interface de-bonding, and fracture branching.

Currently, particulate ceramic composites are generally manufactured using the conventional process of powder sintering where secondary phase particles are mixed with the matrix material. After sintering, the secondary particles form the randomly distributed inclusions; the precise arrangement of these inclusions cannot be controlled. However, co-extrusion techniques have been developed that enable the position and geometry of inclusion to be tailored [8]. This method will be adapted to create ceramic composites

with precisely positioned cylindrical inclusions. With the newly available composite geometry parameters (such as inclusion spacing and the periodic pattern) enabled by this manufacturing technique, a wide range of composites can be created that result in different fracture behavior. However, with the large design space, an efficient and sufficiently accurate method is necessary to quickly discover optimal composite arrangements.

To analyze fracture initiation and propagation in different composite arrangements, we developed an analytical model for the mixed-mode stress intensity factor of a kinked crack within a multi-phase composite with multiple inclusions, which was validated with experiments and was compared with linear elastic fracture mechanics (for initiation) and phase-field simulations (for propagation). Our approach combines the previous analytical models for the mode I [10] and mode II [11] stress intensity factors of a straight crack near an inclusion and a model for the local mode I and II stress intensity factors of a kinked crack tip under far-field mode I and II loading [12]. Using this model and an incremental crack extension method (described later), the toughness of several different composite arrangements was computed based on a crack length metric.

## **2. MIXED MODE STRESS INTENSITY FACTOR OF A KINKED CRACK**

In the following, we analyze the mixed-mode stress intensity factor at a kinked crack tip in the vicinity of two nearby inclusions as shown in Figure 1. The approach is general and can be applied to different composite arrangements with more than two inclusions (as will be shown later), but as a starting example, we restrict to the geometry

in Figure 1. In particular, the change in stress field due to inclusions decays to the far-field stress away from the inclusions. It is therefore a reasonable assumption that only the two nearest inclusions (in a possible array of inclusions) will significantly affect the crack. As will be seen in subsequent sections, experiments will be performed on notched specimens in a 4-point bending configuration. In our analysis, we zoom in on the crack tip in the specimen assuming a far-field loading is applied (due to 4-point bending), which results in a mode I and II stress intensity factor in a homogeneous material with a straight crack,  $K_I$  and  $K_{II}$ , respectively. We now assume there is a kinked crack with length,  $a$ , at an angle,  $\omega$ , relative to the initial straight crack. The radius and angle from the center of the two circular inclusions (relative to the tip of the kinked crack segment) are  $(r_1, \theta_1)$  and  $(r_2, \theta_2)$ , respectively. The radius of the inclusions (assumed equal) is  $R$  and their separation distance is  $D$  as shown in Figure 1(B).

## 2.1. MODE I STRESS INTENSITY FACTOR ON A STRAIGHT CRACK

As a first step, we assume a moment,  $M$ , is applied to the 4-point bending specimen. To analyze the influence of the inclusions on the stress intensity factor, we first compute the stress intensity factor at the notch in the specimen due to the applied moment (assuming at this point the specimen is homogeneous without inclusions). For a 4-point bending experiment with a single edge notched specimen, the stress intensity factors (in mode I and mode II) due to the applied global loading on a straight crack without a kink is given by [13],

$$K_I = \frac{\sqrt{2 \tan\left(\frac{\pi\bar{a}}{2}\right)}}{\cos\left(\frac{\pi\bar{a}}{2}\right)} \left(0.923 + 0.199 \left(1 - \sin\left(\frac{\pi\bar{a}}{2}\right)\right)^4\right) \frac{6M}{BW^{3/2}}, \quad K_{II} = 0, \quad (1)$$

where  $B$  is the depth of the specimen,  $W$  is the width of the specimen, and  $\bar{a} = a/w$  is the ratio of the notch length to the width of the specimen as shown in Figure 1(A).

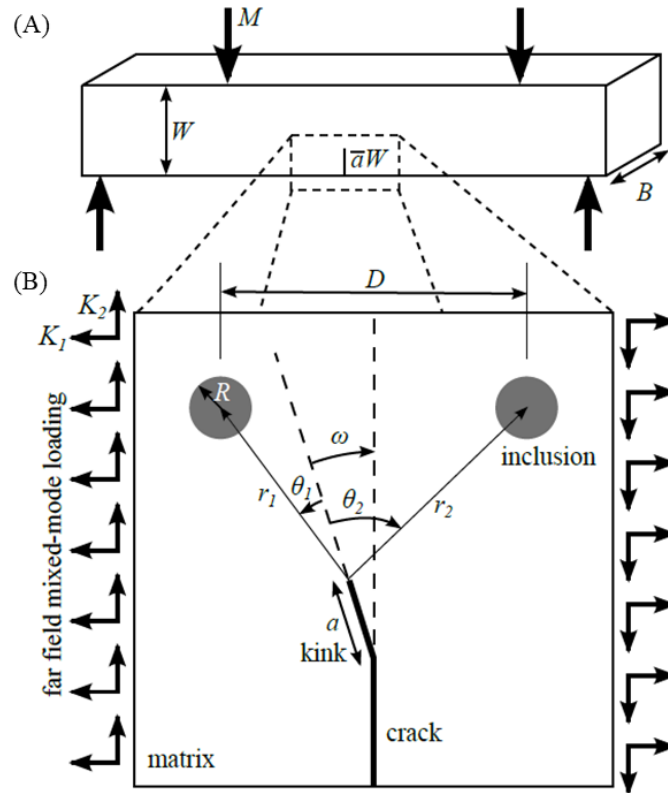


Figure 1. Illustration of (A) the 4-point bending geometry and (B) the geometry of a kinked crack between two inclusions in a specimen subjected to far field mixed loading (zoomed in region near the notch in the 4-point bending specimen).

## 2.2. APPROXIMATE STRESS INTENSITY FACTOR OF A KINKED CRACK

Next, the stress intensity factor of a kinked crack tip (added to the initial straight notch crack) is determined in order to mimic material defects at the crack tip. Due to the presence of nearby inclusions, the crack will prefer to propagate in a certain direction, which is initiated by small-scale defects that we approximate as an infinitesimal kink.

The mode I and II stress intensity factors at a kinked crack in a linear elastic, isotropic, homogeneous material are, respectively, of the form [12]

$$K_I = \text{Re}[c + d]K_1, \quad K_{II} = \text{Im}[c - d]K_1, \quad (2)$$

where  $K_I$  is the mode-I stress intensity factors due to the applied global loading on a straight crack without a kink given in (1), which is in turn related to the applied moment to the specimen. The parameters  $c$  and  $d$  are functions of the kink angle,  $\omega$ , for an infinitesimal kink length (see A). Note that we have proceeded by assuming an initial straight crack and setting  $K_2 = 0$  in the result of [12] to obtain (2).

### 2.3. INFLUENCE OF A NEARBY INCLUSION ON A STRAIGHT CRACK

We now consider the influence of the inclusions on the stress intensity factors (mode I and II) of the kinked crack. Here we follow the analysis [10] and [11] who derived an approximate form for the change in the mode I and II stress intensity factors, respectively, around a straight crack due to the presence of a nearby inclusion. Their approach is based on the influence of a perturbation in material properties on the stress intensity factor of a straight crack [17, 18]. For circular inclusions, the changes in stress intensity factor in mode I and II (for the  $i = 1, 2$  inclusion) are, respectively,

$$\Delta K_{Ii} = K_I \left(\frac{R}{r_i}\right)^2 \left( C_1 \cos\left(\frac{\theta_i}{2}\right) \cos\left(\frac{3\theta_i}{2}\right) + C_2 (\sin^2 \theta_i) \cos \theta_i \right), \quad (3)$$

$$\Delta K_{IIi} = K_{II} \left(\frac{R}{r_i}\right)^2 (C_3 \cos \theta_i + C_4 \cos(2\theta_i) + C_5 \cos(3\theta_i))$$

where  $R$  is the (equal) radius of the inclusions,  $r_i$  is the distance of the  $i$ th inclusion from the crack tip,  $\theta_i$  is the angle of the  $i$ th inclusion relative to the crack (cf. Figure 1). Note that the integral results in [10, 11] have been simplified by assuming the inclusion radius

$R$  is small compared to the distance between the inclusion and crack tip,  $r_i$ , to obtain (3); the original integral expression is computed by evaluating the integrand at the center of the inclusion and multiplying it by the inclusion area. It should also be noted that here we assume the kink length, while small compared to the initial crack, may not be small compared to the distance to the inclusions. Hence, the radius to the inclusions,  $r_i$ , is taken relative to the tip of the kinked crack (not the tip of the initial straight crack). Likewise, the angles of the inclusions are taken relative to the axis of the kinked portion of the crack as shown in Figure 1(B). The coefficients  $C_1$ ,  $C_2$ ,  $C_3$ , and  $C_4$  are defined based on material properties.

$$C_1 = \frac{(1-\alpha)(1-2\nu)}{(1+\alpha-2\nu)}, \quad C_2 = \frac{3(1-\alpha)}{2(1+3\alpha-4\nu\alpha)}, \quad (4)$$

$$C_3 = \frac{(1-\alpha)(11+19\alpha+32\nu^2\alpha-22\nu-40\nu\alpha)}{16(1+\alpha-2\nu)(1+3\alpha-4\nu\alpha)}, \quad (5)$$

$$C_4 = \frac{-(1-\alpha)(1-2\nu)}{4(1+\alpha-2\nu)}, \quad C_5 = \frac{9(1-\alpha)}{16(1+3\alpha-4\nu\alpha)}, \quad (6)$$

where  $\nu$  is Poisson's ratio (assumed to be same for the inclusions and the matrix) and

$$\alpha = \frac{E_{inc}}{E_{mat}} \quad (7)$$

is the ratio of the Young modulus of the inclusion,  $E_{inc}$ , to the Young modulus of the matrix,  $E_{mat}$ . Note that in most cases, the Poisson ratio of the composite materials will not be identical. Hence, the results predicted from this model will be most accurate when the Poisson ratios of the constituents are nearly the same value. Despite this assumption, the model is still able to accurately capture experimental results (to be discussed in subsequent sections). Once the change in stress intensity factor (for mode I and II) due to the  $i^{th}$  inclusion is determined,  $\Delta K_{Ii}$  and  $\Delta K_{IIi}$ , the total stress intensity factor at the crack

tip is found by adding to the stress intensity factor of the straight crack in a homogeneous material,

$$K_{I,total} = K_I + \sum_{i=1}^n \Delta K_{Ii} , K_{II,total} = K_{II} + \sum_{i=1}^n \Delta K_{IIi}, \quad (8)$$

where  $n$  is the number of inclusions. Only two inclusions are shown in Figure 1(b) ( $n = 2$ ), but more can be included as necessary.

Finally, to establish a criteria for crack propagation, the energy release rate for the composite system is defined as (assuming the crack is inside the matrix)

$$J = \frac{(K_{I,total})^2}{E_{mat}} + \frac{(K_{II,total})^2}{\mu_{mat}}, \quad (9)$$

where  $\mu_{mat}$  is shear modulus of matrix material. That is, the crack will tend to propagate in the direction of a kink angle corresponding to the maximum value of  $J$ .

## 2.4. COMBINED EFFECT OF CRACK KINKING AND INCLUSIONS

The total mode I and mode II stress intensity factors  $K_{I,total}$  and  $K_{II,total}$ , are computed via (4), where the stress intensity factors for the kinked crack (without inclusions),  $K_I$  and  $K_{II}$ , are computed via (2). To relate quantities to the experiment, the far field mode I stress intensity factor,  $K_I$ , used to compute the kinked crack stress intensity factors is computed using (1) as a function of the moment,  $M$ , applied to the 4-point bending specimen. Using these relations, the total stress intensity factor at a kinked crack in the vicinity of inclusions can be computed from the load in the 4-point bending test, inclusion properties, inclusion geometry, and inclusion arrangement.

At this point, the important assumptions in our analysis are highlighted: (i) the effect of kinking on the stress intensity factor assumes the kink length is infinitesimally small relative to the overall specimen (but not relative to the inclusion separation

distance), (ii) the inclusions were circular with radii much smaller than their distance to the crack, and (iii) the analysis was simplified by assuming one-way coupling between the inclusions and the K-field. That is, the K-field around a crack was used to compute the stress inside the inclusions, which in turn, via the solution in [19], was used to compute the change in stress at the crack tip (and subsequently the change in stress intensity factor). In reality, the change in stress intensity factor would again influence the stress in the inclusion. This effect is neglected for simplicity. (iv) The matrix and inclusion materials are assumed to have the same Poisson ratio and comparable coefficients of thermal expansion to simplify the equations. This assumption yields reasonably accurate results compared to numerical results for the material system under consideration. Finally, (v) while the kinked crack length is assumed to be infinitesimally small, we treat the kinked portion of the crack as a straight crack when applying equation (3), which would be slightly different than non-straight cracks induced by defects in the specimen.

## **2.5. FINITE ELEMENT VALIDATION FOR FRACTURE INITIATION**

In the following, the accuracy of the proposed analytical model for the mixed-mode stress intensity factor of a kinked crack in the presence of inclusions was examined through a case study using linear elastic fracture mechanics (LEFM) finite element analysis. The stress intensity factor and J-integral predictions were extracted from the finite element analysis.

The mode I and mode II stress intensity factors and J-integral from (10) and (11) were compared to the result from LEFM obtained via finite element analysis using

Abaqus. When simulating dual-phase composites using finite element analysis, the interaction between the crack and the inclusions is generally predicted more accurately through a 3-dimensional model. However, finite element analysis produces similar stress maxima for 2-dimensional plane strain as well as 3-dimensional analyses in comparison to plane stress as the cracks are believed to mostly originate at the core of the specimen [20]. A 2-dimensional plane strain model (using shell elements) with circular inclusions was thus preferred over a 3-dimensional model to simplify the analyses [21-26]. The elements were 4-node bilinear plane strain quadrilaterals with reduced integration scheme.

A representative sample geometry of the 4-point bending test with a 1 mm long centered notch and 0.2 mm kink was selected (see Figure 2(A)). The two-phases of material in the specimen were represented using a partition function. A ramped displacement of 0.1 mm was applied via two contact points on the top, and the resulting stress and strain field was computed. A dense mesh with a smallest element size of 4  $\mu\text{m}$  was generated and a square-root singularity was defined near the crack-tip (see Figure 2(B)). Note that the mesh shown in Figure 2(C) was used in the phase-field simulation discussed in a later section. The material properties are shown in Table 1. Note that the Poisson ratios for the two materials in Table 1 are not identical. Nonetheless, the values are similar such that selecting  $\nu = 0.16$  in the finite element simulation (in order to compare with the analytical model) resulted in an accurate approximation. A representative sample geometry of the 4-point bending test with a 1 mm long centered notch and 0.2 mm kink was selected (see Figure 2(A)).

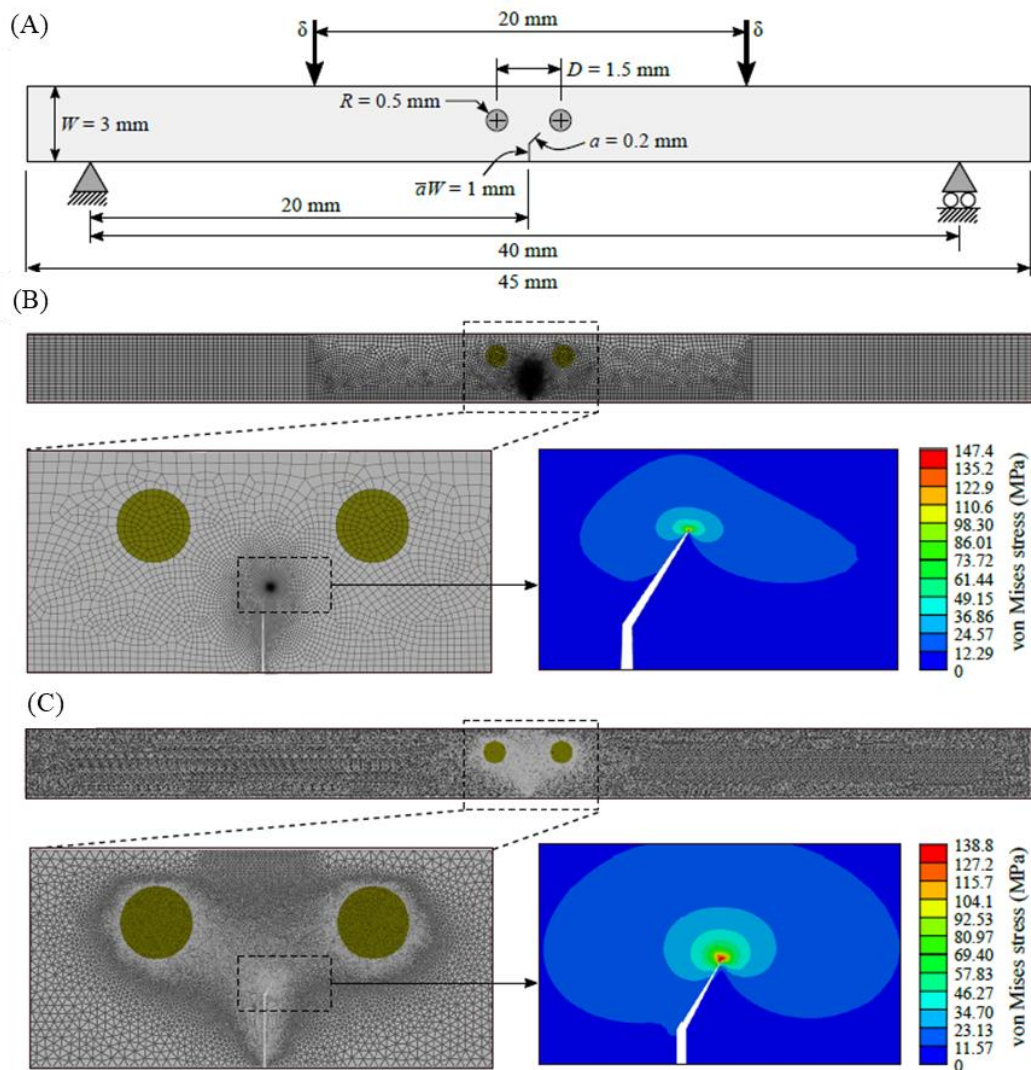


Figure 2. A schematic of the specimen in (A) shows the geometry, loading and boundary conditions for the 4-point bending test, which includes the dimension of the inclusions and kinked crack (in mm). The mesh detail and von Mises stress contours are shown for the (B) LEFM model and (C) phase-field model.

The two-phases of material in the specimen were represented using a partition function. A ramped displacement of 0.1 mm was applied via two contact points on the top, and the resulting stress and strain field was computed. A dense mesh with a smallest element size of 4  $\mu\text{m}$  was generated and a square-root singularity was defined near the crack-tip (see Figure 2(B)). Note that the mesh shown in Figure 2(C) was used in the

phase-field simulation discussed in a later section. The material properties are shown in Table 1. Note that the Poisson ratios for the two materials in Table 1 are not identical. Nonetheless, the values are similar such that selecting  $\nu = 0.16$  in the finite element simulation (in order to compare with the analytical model) resulted in an accurate approximation.

The distance between the inclusions,  $D$ , and the radius of the inclusions,  $R$ , were varied to characterize the accuracy of the analytical model by comparing the stress intensity factors and J-integral predicted by the analytical model and finite element solution. The two different inclusion radii examined were 300  $\mu\text{m}$  and 500  $\mu\text{m}$ . These two radii were considered for the simulation based on their practicality to be fabricated using the co-sintering manufacturing process. This is because exceedingly large inclusions lead to undesirable micro-cracks at the interface, while extremely small inclusions will result in negligible changes in the fracture behavior. The distances between the inclusions were varied from 1.5 mm to 2 mm. It was observed that the influence of the inclusions diminished as the distance between them was increased. Thus, the maximum separation distance was limited to 2 mm as increasing the distance resulted in little change in the stress intensity factor. A contour integral (for evaluating the J-integral) that encircled the crack tip but that did not intersect the inclusions was introduced into the simulation.

For each geometric combination of inclusion radius and separation distance, the mode I and mode II stress intensity factors (see (4)) and the J-integral (see (5)) were plotted versus the kink angle at the end of the notch from  $0^\circ$  to  $90^\circ$  as shown in Figure 3 (negative angles were not considered here due to symmetry). The markers represent the

finite element prediction and the solid lines correspond to the analytical solution.

Figures 3(A), (B), and (C), plot the relative stress intensity factors in model I and II, and the relative J-integral, respectively, versus kink angle for different inclusion separation distances,  $D$ , and fixed radius,  $R$ . The relative  $K_I$  and  $J$  were normalized by their value at zero kink angle  $\omega = 0$ . The relative  $K_{II}$  was normalized by its maximum value in the homogeneous specimen. Figure 3(C), (D), and (E), also show the same plots, but now with different radii,  $R$ , but fixed separation distance,  $D$ .

The analytical model accurately captures the variation of the stress intensity factors and J-integral in the range of kink angles considered (up to  $90^\circ$ ). As postulated through the small kink angle assumption, the accuracy of the analytical model is higher for smaller kink angles. Moreover, at larger kink angles, the analytical model is less accurate for the cases with inclusions than the one without inclusions (owing to the assumptions made when incorporating inclusions in the model). To summarize, for this specimen geometry, the analytical model predictions are within 5% (at most) of the result from finite element analysis. The addition of the inclusions causes an increase in the stress intensity factors and J-integral relative to the homogeneous case. This is expected for the case of compliant inclusions considered here (cf. Table 1), which tend to increase the stress field near the crack tip. Furthermore, as shown in Figure 3, increasing the size of the inclusion results in an increased J-integral. The reduced accuracy of the analytical model for large inclusion sizes is consistent with the underlying assumption of the inclusion radius being small compared to the crack length.

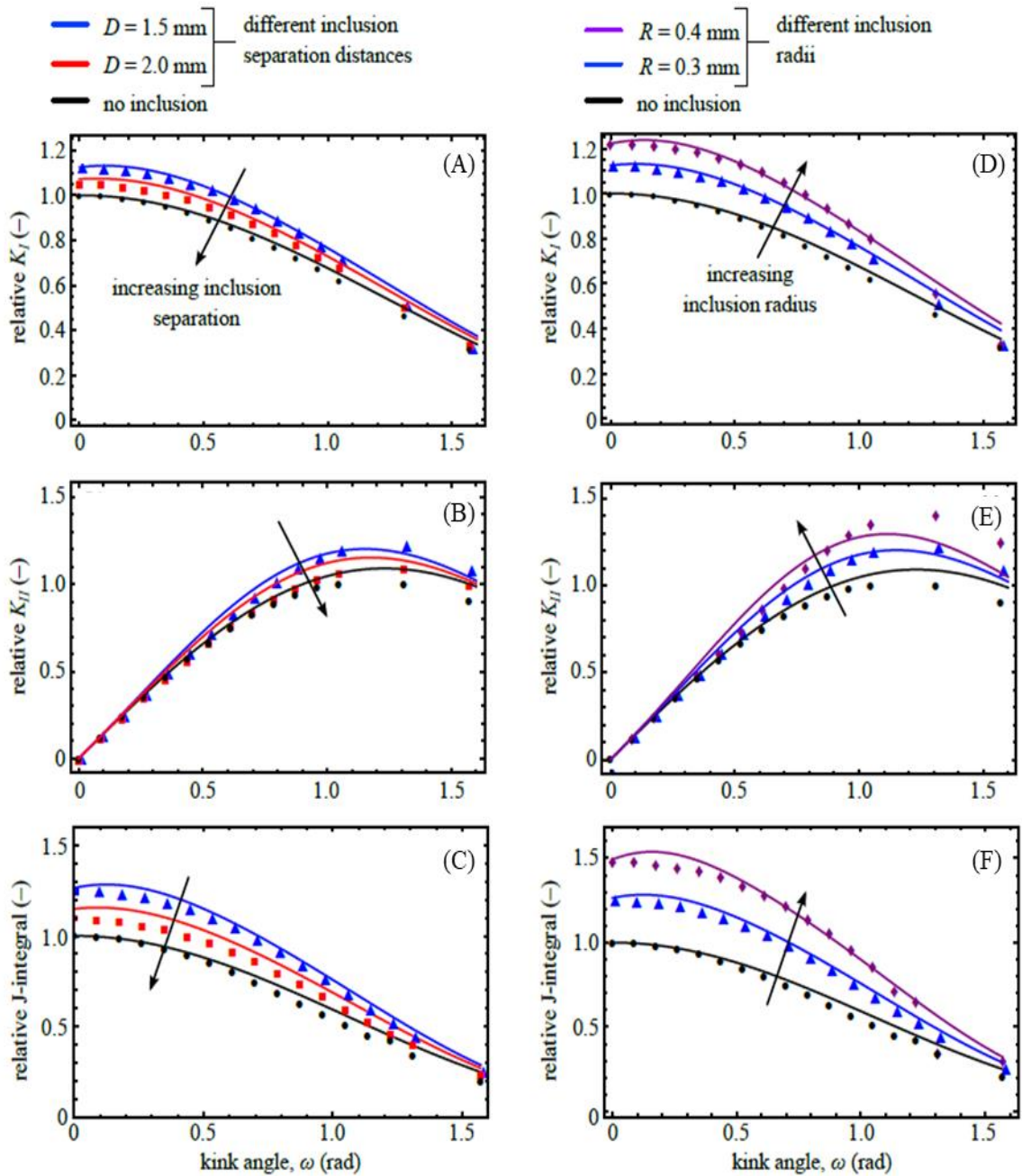


Figure 3. Comparison between analytical model (lines) and linear elastic finite element simulation (dots). Each row shows, respectively, the mode I and II stress intensity factors, and the J-integral versus kink angle. The plots of  $K_I$  and J are normalized by their value for the homogeneous case with zero kink angle while  $K_{II}$  was normalized by its maximum value in the homogeneous case. The left column shows the effect of different inclusion separation and the right column illustrates the effect of different inclusion radii.

### 3. FRACTURE PROPAGATION

#### 3.1. INCREMENTAL CRACK EXTENSION METHOD

To predict the propagation of a crack, we propose an incremental crack extension method. First, an initial crack tip location is chosen. Then a small kink is added to the end of the crack. Using the fracture initiation model based on the J-integral of the kinked crack, the kink angle resulting in the maximum J-integral is found numerically. That is, find the kink angle,  $\omega$ , that maximizes  $J$  in (5). This kink angle is taken to be the preferred propagation direction. Once the preferred propagation direction is determined, the new crack tip is found by adding a small crack increment of length,  $\Delta a = 0.001$  mm, in the preferred direction. Then, the process is repeated to find the new preferred propagation direction from the current crack tip. Contour plots of the spatial variation of the maximum J-integral and its corresponding kink angle are shown in Figure 4(A) and (B), respectively. The inclusion separation distance was  $D = 1.5$  mm and the inclusion radii were  $R = 0.3$  mm. The material properties used were the same as Table 1 (and taking  $\nu = 0.16$ ). One can see in Figure 4(a) that the maximum J-integral (of all kink directions) increases closer to the inclusions. In addition, the kink angle giving rise to the greatest J-integral tends to point towards the left inclusion when the crack is on the left half of the specimen and vice-versa on the right-half, as shown in Figure 4(B).

This is, of course, an approximation because the crack path behind the tip is not accounted for (each iteration assumes a straight crack up to the current crack tip location). However, this approach does provide a first approximation of the crack path as

most of the material behind the crack tip becomes unloaded and thus does not significantly affect the stress at the crack tip.

Table 1. Material properties of the matrix and inclusion materials used in experiments and finite element analysis. The elastic properties of the matrix were measured via the impulse excitation technique while the remaining properties were obtained from the supplier (H. C. Starck). The properties of the inclusion were also obtained from the supplier (Goodfellow).

<b>Parameter:</b>	<b>Symbol:</b>	<b>Value:</b>
Matrix <sup>12</sup>		
<b>Young's modulus</b>	$E_{mat}$	512 GPa
<b>Poisson's ratio</b>	$\nu_{mat}$	0.16
<b>Coefficient of thermal expansion (300K to 1073K)</b>	$CTE_{mat}$	$6.6 \times 10^{-6}/K$
<b>Energy release rate</b>	$G_{cmat}$	0.02674 N/mm
Inclusions <sup>3</sup>		
<b>Young's modulus</b>	$E_{inc}$	2.55 GPa
<b>Poisson's ratio</b>	$\nu_{inc}$	0.17
<b>Coefficient of thermal expansion (273K to 373K)</b>	$CTE_{inc}$	$4.3 \times 10^{-6}/K$
<b>Energy release rate</b>	$G_{cinc}$	0.035 N/mm

---

<sup>1</sup> measured using impulse excitation technique

<sup>2</sup> supplier (H.C. Starck) information

<sup>3</sup> supplier (Goodfellow) information

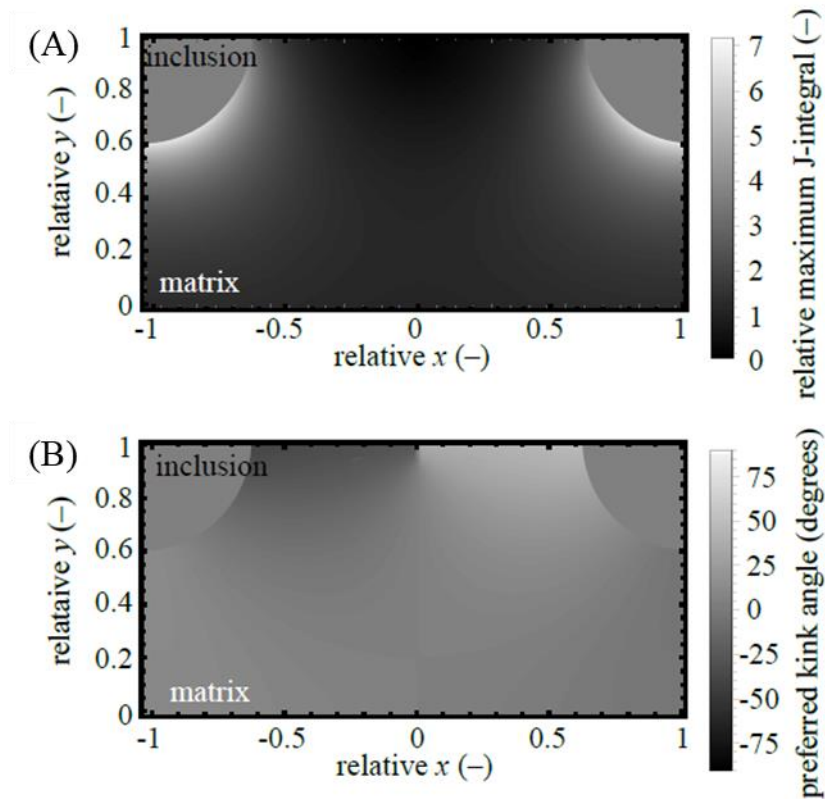


Figure 4. Contour plots of the (A) J-integral and (B) kink angle in the preferred direction. The J-integral was normalized by its value for the straight kink at the origin. The coordinate axes are normalized by the inclusion separation distance,  $D/2$ .

### 3.2. PHASE-FIELD MODEL

To gauge the accuracy of the crack extension method, we compare the estimated crack paths from the proposed approach with those predicted from a phase-field simulation and experiments. While the phase-field approach is common for predicting crack paths, the incremental crack extension method is a more computationally efficient alternative to obtain a first approximation of the crack paths through the composite. This is especially helpful as a first pass to sample the very large space of possible composite materials and geometric combinations.

The fundamental idea in brittle fracture is that a crack forms in order to minimize the internal energy (a combination of strain energy and crack surface energy), which dates back to the work in [27]. Assuming linearized kinematics, the internal energy of a solid occupying a region  $\Omega$  with a crack surface  $\Gamma$  is

$$U = \int_{\Omega/\Gamma} \psi(\varepsilon) d\Omega + \int_{\Gamma} G_c dA, \quad (10)$$

where  $\psi$  is the strain energy density defined such that the stress is given by  $\sigma = \frac{\partial \psi}{\partial \varepsilon}$  and  $\varepsilon$  is the small-strain tensor (since ceramic composites are being considered, the assumption of linearized kinematics is appropriate). The crack surface energy is  $G_c$ . Note that the crack surface energy takes on different values,  $G_{cinc}$  and  $G_{cmat}$ , depending on if the crack is in the matrix or inclusion, respectively. In the phase-field approach, the surface integral is transformed into a volume integral to simplify the numerical implementation of the model via a degradation function [22], [23],  $\phi(x) \in [0,1]$ ,

$$U = \int_{\Omega} ((1 - \phi)^2 + k) \psi(\varepsilon) d\Omega + \int_{\Omega} \frac{G_c}{2} \left( l_0 \nabla \phi \cdot \nabla \phi + \frac{1}{l_0} \phi^2 \right) d\Omega, \quad (11)$$

where now the degraded stress is  $\sigma = \frac{\partial \varphi}{\partial \varepsilon}$ , with  $\varphi = ((1 - \phi)^2 + k) \psi(x, \varepsilon)$ . The material is completely fractured where  $\phi = 1$  and is undamaged where  $\phi = 0$ . Also, we let  $\psi$  depend on the spatial position  $x$  since we will be considering composite materials with different elastic moduli. Hence, the strain energy function will vary with position. The parameter,  $k = 10^{-5}$ , is a small number for numerical conditioning. The crack width is characterized by  $l_0$ .

The results for the Euler-Lagrange (equilibrium) equations that minimize the potential energy based on internal energy given in the previous section are shown in Table 2. We implement this material model within the finite element method framework

of Abaqus using subroutines including UMAT and UEL. Constant strain triangle elements were used with a single integration point (cf. Figure 2 (c)). The material parameters used in the phase-field model are the same as those used in the finite element simulation and analytical model, which are shown in Table 1. However, in addition to Table 1, the intrinsic length scale parameter,  $l_0$  in the phase-field model was taken to be 1% of the inclusion diameter.

Table 2. The Euler-Lagrange equations of the potential energy used in the phase-field model. Note that the summation convention is implied in the index notation form and commas denote differentiation with respect to the spatial coordinates.

Symbolic	Index notation	Description
$\nabla \cdot \boldsymbol{\sigma} = \mathbf{0}$	$\sigma_{ij,j} = 0$	Stress equilibrium
$\boldsymbol{\sigma} \mathbf{n} = \mathbf{t}$	$\sigma_{ij,j} n_j = t_i$	Traction relation
$\frac{\partial \phi}{\partial \phi} + \frac{G_C \phi}{l_0} + G_C l_0 \nabla^2 \phi = 0$	$\frac{\partial \phi}{\partial \phi} + \frac{G_C \phi}{l_0} + G_C l_0 \nabla^2 \phi_{,ii} = 0$	Degradation function PDE
$\nabla \phi \cdot \mathbf{n} = 0$	$\phi_{,i} n_i = 0$	Boundary condition of degradation function

### 3.3. SPECIMEN PREPARATION FOR 4-POINT BENDING EXPERIMENTS

To fabricate composite specimens, a powder-based sintering approach was used [24]. The procedure is detailed in Figure 5. Fabricating composites comprised of multi-phase constituents depends on their thermo-mechanical properties, geometry, size, and nature of the interface between them [25]. For the experiments, materials were selected that best mimicked the system analyzed in Figure 1. In particular, materials with similar Poisson ratios and comparable coefficients of thermal expansion (to reduce residual stress and interface cracking from the sintering process) were selected. To this end, a zirconium

diboride matrix and graphite inclusions were chosen (refer to Table 1 for material properties). A batch of powdered grade B zirconium diboride (93.86 wt.%) by H.C. Starck with phenolic resin (2.3 wt.%), boron carbide (0.98 wt.%), and traces of polyethylene glycol and polyvinyl butyral (PVB) were added as a binder and plasticizer, respectively, to the mix for the matrix. A batch of graphite (47.42 wt.%), methoxy polyethylene glycol MPEG (0.91 wt.%), heavy mineral oil (3.67 wt.%), polyether block amide PEBA-7 (24.83 wt.%), zirconium diboride (23.17 wt.%) and phenolic resin was prepared for the inclusion. These compositions are summarized in Table 3. The carbon and boron carbide additives to the  $ZrB_2$  batch promote its densification [26]. These batches were ball milled in acetone for 24 hours at ambient temperature and pressure using tungsten carbide milling media. The solution was then dried via rotary vacuum evaporation to obtain powder mixtures suitable for densification.

For the inclusion material, graphite powder was blended with the thermoplastic polymer and plasticizers (Table 3) using a torque rheometer at 130°C and 30 RPM. This material was formed into a cylindrical feed-rod using a heated hydraulic press. This feedrod was then extruded into finer filaments with the desired diameters using a ram extruder. For the matrix, the powdered mixture batch (Table 3) was molded into billets of desired dimensions using a rectangular die and hydraulic press before drilling at selected inclusion locations using fine 0.5 mm diameter, tungsten carbide drill bits.

Then the graphite filaments were threaded through the matrix and the resulting sample was co-sintered in a graphite hot-press (Model HP20-3060; Thermal Technology Inc., Santa Rosa, CA) to form the precursor to the final specimen (typical overall billet dimensions were  $40 \times 30 \times 5 \text{ mm}^3$  with 500  $\mu\text{m}$  diameter inclusions).

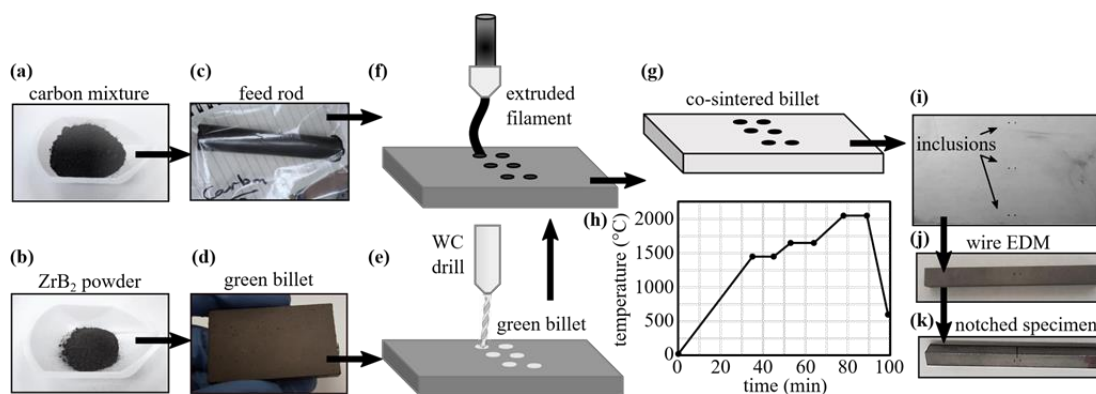


Figure 5. Illustration of specimen fabrication process showing the (A) carbon mixture for inclusions, (B) ZrB<sub>2</sub> powder for matrix, (C) carbon feed rod, (D) ZrB<sub>2</sub> green billet, (E) periodic holes drilled into the green billet, (F) carbon feed rod extruded into filaments, (G) co-sintered ZrB<sub>2</sub>-C billet, (H) sintering schedule, (I) ceramic composite with inclusions, and (J, K) the test specimens cut and notched.

The specimens were heated under vacuum (200 mTorr) with approximately 1 hour isothermal holds at both 1450°C and 1650°C. Following the 1650°C hold the atmosphere was changed to flowing argon and a pressure of 32 MPa was applied. The specimen was then ramped to the final densification temperature of 2050°C. . A ramp rate of 75°C/min was maintained for the first two holds and then a ramp rate of 60°C/min was applied until the densification temperature was attained. The ram travel was monitored upon reaching the final temperature to determine when the densification process ceased before cooling. The planar surfaces of the resulting sintered billets were ground using a Chevalier FSG-618 surface grinder with a 400 grit diamond grinding wheel with progressively finer diamond abrasives from National Diamond Lab. The resulting surface finish facilitated the observation of the specimen under the microscope during experiments. The polished billets were then cut into desired specimen size through wire electrical discharge machining.

Table 3. Constituents of the composite specimens.

<b>Material</b>	<b>Quantity (wt.%)</b>
Matrix zirconium diboride (grade B)	96.67
Phenolic resin	2.35
Boron carbide	0.98
Polyethylene glycol	Trace
Polyvinyl butyral (PVB)	Trace
inclusion graphite	47.42
methoxy polyethylene glycol (MPEG)	0.91
heavy mineral oil	3.67
polyether block amide (PEBA-7)	24.83
zirconium diboride	23.17

A straight notch centered between the inclusions was introduced in one specimen and an off-set notch was introduced in the second specimen via wire electrical discharge machining. These specimens were subjected to a four-point-bend test using a 200 N leadscrew micro-tensile tester by Deben-GATAN and were observed under Hirox Digital KH-8700 optical microscope as illustrated in Figure 6.

The bonding between the inclusion and matrix is of great importance when attempting to alter crack propagation using the inclusions. A key factor towards improving the bond strength is to use materials for the matrix and inclusion with comparable coefficients of thermal expansion since the main cause of debonding is residual stress arising during the sintering process (due to mismatched coefficients of thermal expansion), which cause cracks to form. Composites with second-phase inclusions are particularly susceptible to stress-induced micro cracking due to the localized stress fields formed during the co-sintering process [27]. In addition,

spontaneous interface failures are particularly prominent in materials with large elastic mismatch.

The inclusion size required to reduce interface fracture during sintering is a function of critical stress intensity factor, Poisson's ratio, and residual stress [27]. Generally, smaller inclusions have smaller interaction volume with surrounding matrix; thus, lesser residual stress. This in turn reduces the likelihood of cracking. In addition, selecting materials with comparable coefficients of thermal expansion will mitigate interface fracture. Preliminary composite specimens containing zirconium diboride with graphite inclusions with diameters of approximately 500  $\mu\text{m}$  resulted in no noticeable crack formation at the interfaces.

With the above manufacturing constraints, it would appear that the possible choices of materials and geometries are quite restricted. However, if certain material combinations are found to be desirable based on simulation results, but manufacturing such specimen results in interface debonding, there are other manufacturing routes that could be employed to reduce residual stresses. For example, recent work [28], [29] has focused on creating spiral shaped inclusions whose geometry reduces the residual stress. The spiral inclusion shape is formed by rolling layers of the inclusion and matrix material together, followed by co-extrusion into fibers to obtain the desired inclusion composition and geometry. Such spirals could be used in place of cylindrical inclusions. The spiral would practically behave as a cylindrical inclusion with its effective elastic modulus based on the relative volume fractions of materials forming the spiral. However, the introduction of such spiral inclusions is beyond the scope of this project.

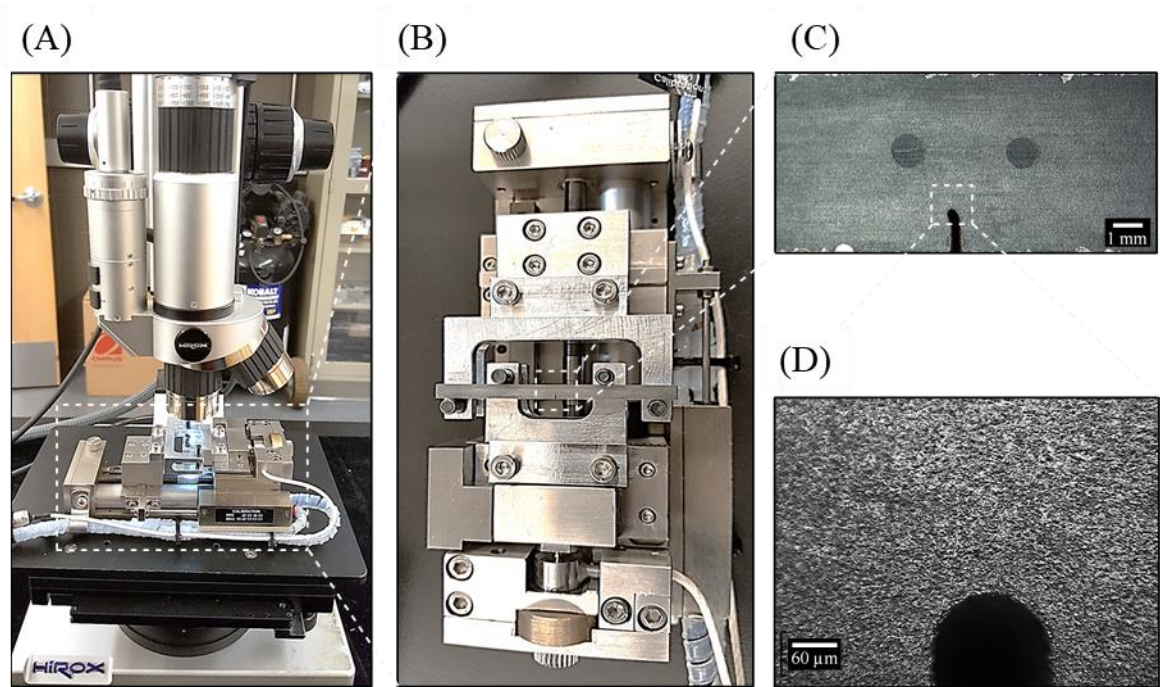


Figure 6. Images of the (A) experimental set-up, (B) micro-tensile tester equipped with 4-point bending test fixture, (C) specimen with kinked notch and inclusions, and (D) the crack-tip.

Two types of specimens were produced with different crack offsets (relative to the central axis between the inclusions). For the specimens, the separation distance between the inclusions was the same,  $D = 1.8$  mm. The diameter of the inclusions was  $500 \mu\text{m}$ . For one type, the initial notch was half way between the inclusions while for the other, the initial notch was placed  $0.5$  mm to the right of the central axis. Both were loaded to failure. The fracture path is shown for each specimen in Figure 7 (A). From the experiments, the maximum load before the ultimate failure of the specimen was 28% higher for the specimen with the off-set notch than the centered notch,  $66$  N and  $52$  N, respectively. This illustrates the result that purely geometrical effects can be used to alter (and increase) the failure load (i.e. strength). Moreover, by examining the fracture paths

between the two cases, fracture surface area in the specimen with the off-set notch is higher than in the centered notch. Thus, inclusions near the initial crack result in increased crack surface area (and subsequently increased energy dissipation and toughness) by solely altering the geometry.

## 4. DISCUSSION

### 4.1. VALIDATION OF PROPOSED APPROACH

To validate the proposed analytical framework, the experimentally observed crack path was compared with the computed crack paths from the shooting method and the phase field model as shown in Figure 7. Figure 7 (A) shows the experimentally observed crack path for the two specimens with different initial notch positions and angles. Figure 7 (B) combines the crack paths obtained from the experiments (transcribed from microscope images), phase-field model, and shooting method. The phase-field crack prediction was determined by plotting the line of maximum crack set parameter,  $\phi$ . The trend of the fracture path predicted by the shooting method follows the experimentally measured crack initially but deviates as the crack approaches the inclusion, which is consistent with the various assumptions in the model. Also, the phase-field prediction follows both the experimentally measured crack and the shooting method result. While the phase-field result is slightly closer to the experimentally measured crack than the shooting method, the phase-field method required significantly more time to compute. For comparison, the shooting method approximation required on the order of seconds to generate the path shown in Figure 7, while the phase field method required on the order

of hours to simulate the corresponding path. While a detailed comparison of the run time between the two methods is beyond the scope of the paper, the order of magnitude difference in run time illustrates, qualitatively, the efficiency of the shooting method approach over the phase-field approach, while maintaining accuracy.

Upon establishing the accuracy of the analytical model through LEFM finite element analysis, phase field modeling, and an experimental case study, it was applied to investigate the influence of the inclusion properties and arrangement on the crack behavior in the matrix. The material characteristics, especially the Young's modulus mismatch, geometry and the location of the inclusions with respect to the crack-tip is shown to affect the crack initiation and subsequently the propagation through the matrix material.

#### **4.2. RELATIVE CRACK LENGTH INCREASE METRIC**

In order to quantitatively compare the effectiveness of different composite design on increasing the overall toughness of material, the relative crack length increase metric is used,  $L/L_H$ , where  $L$  is the total length of the crack as it passes through a unit cell of inclusions and  $L_H$  is the length of a straight crack passing the same unit cell (if the material was replaced by a homogeneous one). In linear elastic fracture mechanics, the energy dissipated due to crack propagation is transferred into the energy of the new surface area. In two dimensions, the size of the crack surface area is proportional to the length of the crack. In the following, we restrict our analysis to consider the case where the fracture propagates through the matrix (i.e. it does not intersect with inclusions). This is due to the corresponding assumption made in the stress intensity factor calculation. In

other words, the following study of the effect of composite design on toughness focuses on the mechanism of crack deflection within the matrix. In this setting, the ratio of the energy dissipated in one unit cell between a homogeneous and composite specimen (quantifying the relative toughness), is equal to the relative crack length increase metric,

$$\frac{G_{c,matA}}{G_{c,matA_H}} = \frac{L}{L_H}, \quad (12)$$

where  $A$  and  $A_H$  are the surface areas of the crack in the composites compared to a homogeneous material. In the two dimensional analysis, a unit depth is assumed.

### 4.3. INFLUENCE OF INCLUSION SEPARATION DISTANCE ON FRACTURE

An obvious factor to consider when designing a composite with an array of inclusions is to examine the effect of the spacing between the inclusions. In particular, it is important to understand the ability of the inclusions to affect the fracture process. To illustrate this effect, fracture paths from the phase-field simulation and the crack extension method are computed assuming different initial starting points between the center line, at  $x = 0$ , and the inclusion, at  $x = D/2$ , in increments of 0.1 mm as shown in Figure 8(A) (for two different ratios of the inclusion separation to the radius,  $R/D$ ); the crack extension method and phase-field model are compared again here in order to assess the accuracy of the analytical model as crack paths pass closer to the inclusions.

As can be seen in the two plots of Figure 8(A), for larger crack offsets (resulting in a crack path that is also closer to the inclusion), the deviation of the crack extension method from the phase-field simulation increases, which is consistent with the assumptions in the model regarding the coupling between the inclusion and crack tip.

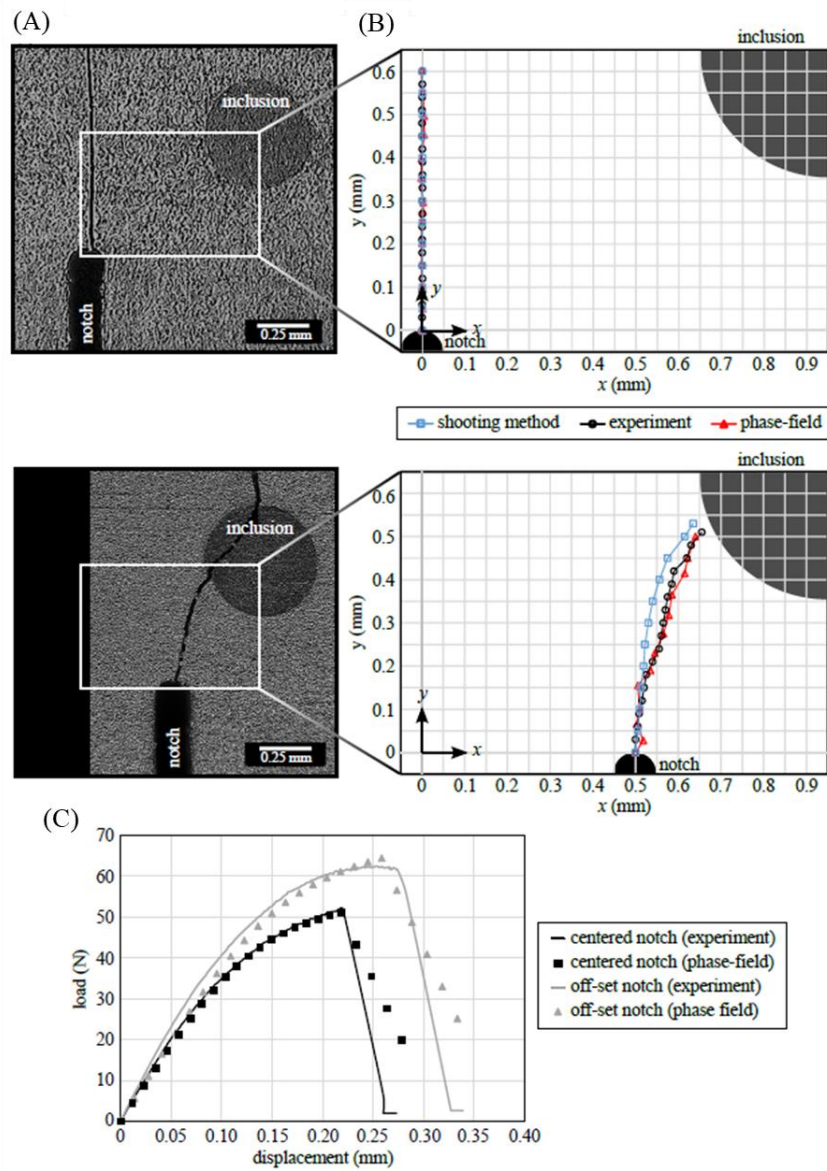


Figure 7. (A) Experimental crack paths after complete fracture for varying notch locations. (B) Crack paths from the proposed method, phase field model and experiment. (C) Load vs. load point displacement curve from experiment and phase field model illustrating variation in failure load and subsequently toughness between specimens with centered and off-set notch.

Quantitatively, in the left plot of Figure 8(A), with  $R/D = 0.15$ , the percent difference between the crack extension method and phasefield simulation (relative to the inclusion separation,  $D$ ) for each crack path is 0.3, 2.5, 6.5, and 12.0%, for the cracks

with initial offsets of  $x = 0, 0.1, 0.2,$  and  $0.3$  mm, respectively. Thus, the error of the extension method increases as the crack path passes closer to the inclusion. Qualitatively, however, the crack extension method is able to capture the same trend of the inclusions having a greater impact on the crack as it passes closer to the inclusion. Again, it should be emphasized that the main advantage of the crack extension method is that it can be used as a first approximation to begin narrowing down the design space due to its computational efficiency. Simulating the entire design space with the phase-field method may not be feasible depending on the computational resources available.

It is intuitive that the smaller the separation distance between the inclusions is, the closer the fracture pathway is to the adjacent inclusion. Consequently, the closer the crack passes to the inclusion, the influence of the inclusion on the crack path is higher. This is illustrated in Figure 8(B), which plots the relative percent increase in crack length (relative to the straight crack) where the separation distance,  $D$ , between the inclusions was changed between 1.5 mm and 2 mm and their radius  $R = 0.3$  mm was held fixed. In dimensionless terms, Figure 8(B) shows the results for specimens with  $R/D = 0.15$  and 0.2. It can be observed that the relative percent increase in the crack length, which correlates with the influence of the inclusion, is more significant for a given crack location offset for specimens with smaller inclusion separation distance for a fixed applied loading condition. An increase in crack length implies a larger crack surface area (and subsequently increased energy dissipation and toughness), thereby altering the fracture toughness of the specimen solely by varying the location of the inclusions within the matrix.

#### 4.4. EFFECT OF THE INCLUSION PATTERN ON THE TOUGHNESS

The crack extension method was used to study three composite designs, motivated by the results of [36], in order to determine the one resulting in the greatest toughness enhancement. The three designs scenarios were (1) a cubic array of stiff inclusions rotated by an angle relative to the initial crack in order to guide the crack, (2) a bodycentered cubic array of stiff inclusions to create a zig-zag pattern that increases crack length, and (3) a multi-phase cubic array of stiff and soft inclusions to also create a zig-zag pattern that increases crack length.

**4.4.1. Crack Guiding using a Rotated Cubic Array.** Altering the direction of crack propagation is useful for increasing the crack length (and therefore also the energy dissipated) as well as deflecting a crack away from a sensitive component in a material or structure. In this design, stiff inclusions are selected in order to contain the crack propagation within the matrix. A cubic array with  $n = 16$  circular inclusions with variable radius  $R$ , and fixed spacing  $D = 1.5$  mm, were simulated, such that  $R/D \in [0.1, 0.8]$ . This is accomplished by using the crack extension method based on the stress intensity factor in (4) where now the number of terms in the summation is increased due to the additional inclusions.

To guide the crack, the cubic array was rotated by an angle  $\gamma$  relative to the initial direction of the notch crack. In this study, we sought to determine the  $R/D$  ratio that gave rise to the largest relative crack length increase  $L/L_H$ . The longest crack length corresponded to the case with the largest possible array orientation angle  $\gamma$ , while containing the crack within the matrix. The simulations were repeated for three different values of elastic mismatch ratio:  $\alpha = 2, 5, \text{ and } 10$  (defined in (12)). To change the elastic

mismatch ratio, the Young modulus of the inclusion was varied while the Young modulus of the matrix was held fixed as the value in Table 1.

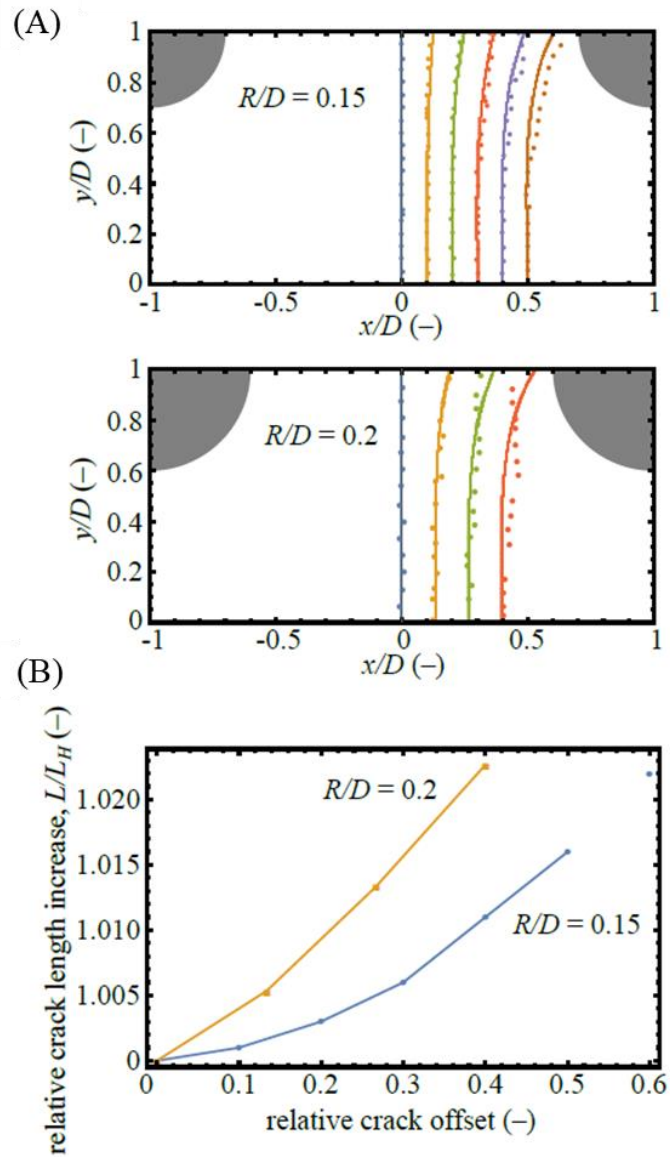


Figure 8. Simulation of (A) crack propagation for different initial crack offset positions (the solid line denotes the crack extension method and the dots show the phase-field simulation) and (B) crack length increase versus inclusion separation and offset position predicted from the crack extension method. All distances are relative to the inclusion separation distance,  $D$ .

The initial notch was assumed to be centered relative to the inclusion array (denoted by the origin in the Figure 9).

As an example, for the case of an elastic mismatch of  $\alpha = 10$ , and  $R/D = 1/3$ , the maximum angle of the array orientation such that the crack remains in the matrix is shown in Figure 9. If the orientation angle of the inclusions is further increased, the crack enters into the inclusions, which is not accounted for in the simplified model. If the orientation of the array is reduced, the crack is deflected was  $L/L_H = 1.0078$ .

In a similar manner the maximum angle of the inclusion orientation and the corresponding relative crack length increase were computed for different inclusion radii and elastic mismatch ratio, and are shown in Figure 10(A) and (B), respectively. One can see in Figure 10(A) that as  $R/D$  increases, the maximum angle that the array can be rotated (while maintaining crack propagation within the matrix) decreases. This is because smaller inclusions can be shifted over a greater distance before intersecting the crack path (due to their smaller radii). The relative crack length increase versus inclusion radius in Figure 10(B) interestingly shows a maximum. Generally, as  $R/D$  increases, it has a greater impact on crack deflection and thus the crack length increases. However, increasing  $R/D$  eventually has a negative impact on the crack deflection because the angle of the inclusion array must be reduced to prevent the crack from intersecting the inclusion. Thus, there is an important trade between array orientation and inclusion size that must be optimized in such a design. Of the cases considered, generally  $R/D = 1/3$  appears to be the optimal geometry for any elastic mismatch ratio when designing a composite for crack guiding.

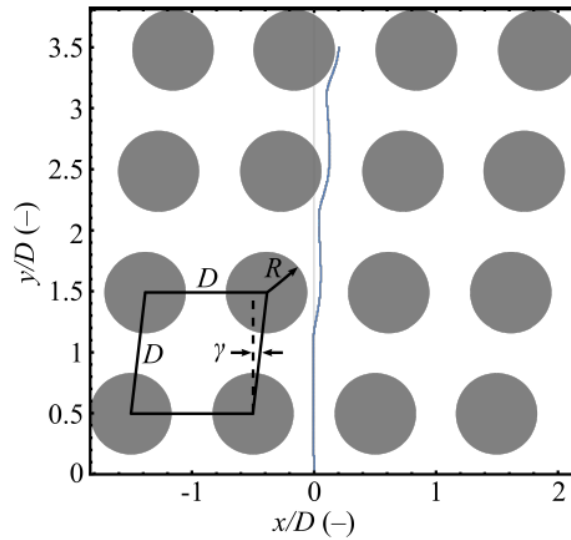


Figure 9. Example cubic array of stiff inclusions ( $a = 10$  and  $R/D = 1/3$ ), denoted by the shaded circles, oriented at an angle  $\gamma = 7^\circ$ . The crack (blue line) is guided by the orientation of the inclusions.

**4.4.2. Crack Deflection using a Body-centered Cubic Array.** In the previous design scenario, the orientation of the array itself was used to deflect the crack and increase its length. In the proposed body-centered cubic array, the relative position of the inclusions is used as a mechanism to control the crack path as illustrated by the example in Figure 11(A). As with the previous example, the inclusion spacing is held fixed at  $D = 1.5$  mm while the radius of the inclusions and elastic mismatch ratio were varied. The number of inclusions used was  $n = 21$ . The initial crack position was centered between the initial inclusion and the body-centered inclusion, i.e. at  $x = D/4$ . The result in Figure 11(A) corresponds to  $R/D = 0.24$  and  $\alpha = 10$ .

For different combinations of inclusion radius and elastic mismatch ratio, the relative crack length increase  $L/L_H$  was computed (see Figure 11(B)). One can see in Figure 11(B) that as  $R/D$  increases, the relative crack length increases.

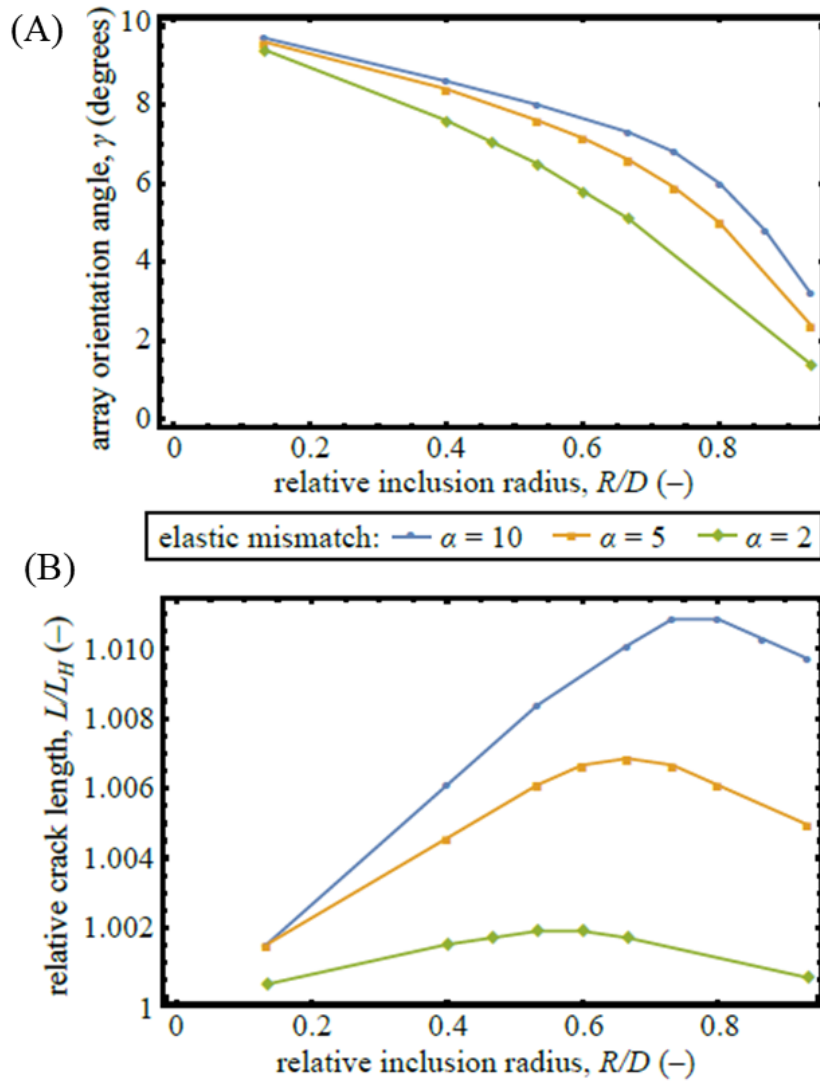


Figure 10. (A) Plot of the maximum allowable orientation angle of the inclusions versus relative inclusion radius. (B) Plot of the corresponding relative crack length increase versus relative inclusion radius.

However, the inclusion size cannot be increased arbitrarily large while containing the crack in the matrix. In this case, for  $R/D > 0.24$ , the crack will propagate in the inclusions (for each of the elastic mismatch ratios considered). For each radii, the crack length increase is higher for greater elastic mismatch. In summary, the maximum

inclusion radius to spacing ratio was determined for the body-centered array and the corresponding crack length increase was computed.

Comparing the results in Figure 11(B) with the previous results for the rotated cubic array in Figure 10(B), for similar combinations of inclusion radius and elastic mismatch ratio, the relative crack length increase is always higher for the body-centered cubic array than for the rotated cubic array. Thus, the local individual position of the inclusions has a greater effect on crack length (per unit cell) than the global deflection of the crack using the rotated cubic array. However, for crack guiding, the rotated cubic array can globally deflect and guide the crack, while changes in the local inclusion arrangement made possible in the body-centered cubic array only locally deflects the path while the global path remains fixed.

**4.4.3. Crack Deflection in a Multi-phase Array.** As a final scenario, we consider the addition of a second (weak/soft) inclusion material to the previous consideration of only stiff inclusions. Motivated by the zig-zag behavior observed in Figure 11(A), the case of an alternating stiff and soft inclusion pattern was hypothesized to further increase the amplitude of zig-zag behavior.

For example, see Figure 12(A), which shows the arrangement of the stiff and soft inclusions in a cubic array. Generally, the crack is attracted to the soft inclusions and repelled by the stiff inclusions, resulting in the zig-zag behavior. With two different sets of inclusions, there are now two elastic mismatch ratios to consider corresponding to the strong/stiff inclusion and to the weak/soft inclusion,

$$\alpha_1 = \frac{E_{stiff}}{E_{mat}}, \quad \alpha_2 = \frac{E_{soft}}{E_{mat}} \quad (9)$$

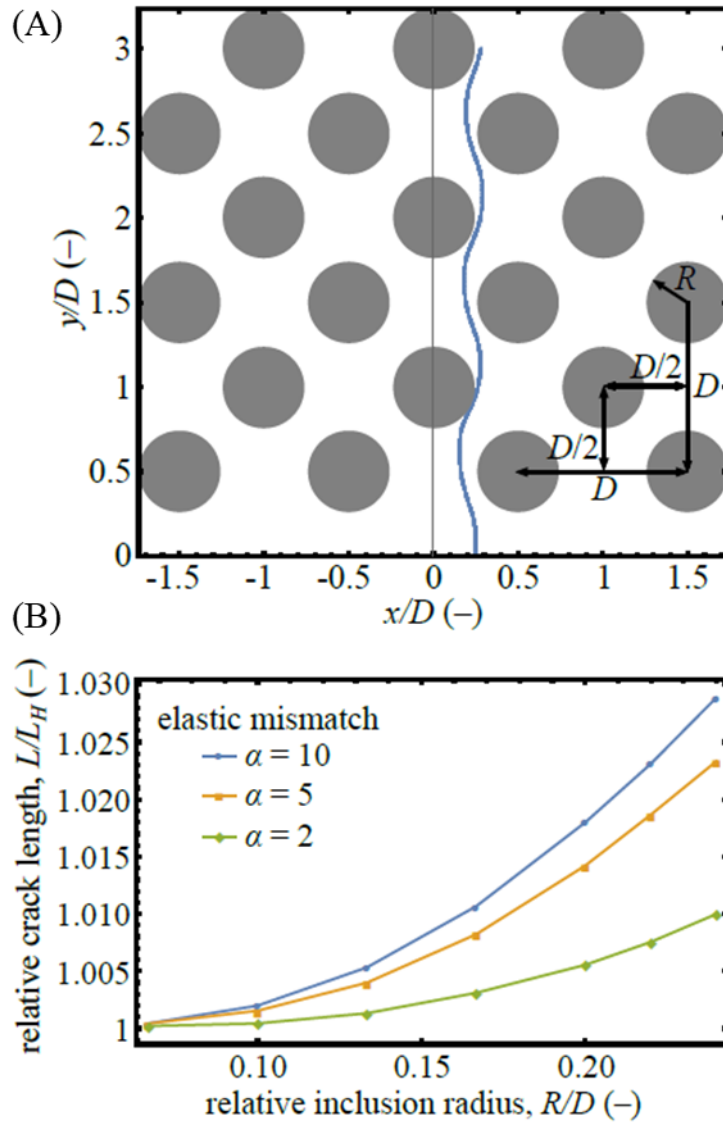


Figure 11. (A) Body-centered cubic array of stiff inclusions used (shaded area) to increase the crack length (blue line). (B) Plot of the relative crack length increase versus relative inclusion radius.

These two values of  $\alpha$  are substituted into the expression for the coefficients in (11) for each inclusion that is added in the summation in (4). The three combinations of stiff and soft inclusions were the pairs:  $(\alpha_1, \alpha_2) \in \{(10, 0), (5, 0.5), (2, 0.1)\}$ . The crack propagation through composites with different inclusion radii and elastic mismatch ratios

was simulated and the resulting relative crack length increase was determined and is shown in Figure 12(B). Generally, as  $R/D$  increases, the relative crack length increases due the increasing impact of larger inclusions on the crack path. However, for each combination of elastic mismatch, there exists a limit to how large the inclusions can be before the crack intersects the inclusions (corresponding to the largest value of  $R/D$  plotted on the axis). For greater elastic mismatch, the largest inclusion radii that can be used is reduced. However, for greater elastic mismatch (even with the limitation in maximum  $R/D$ ), the relative crack length increase is higher for any  $R/D$ . In particular, for the multi-phase array, the relative crack length increase for the case of the greatest elastic mismatch was nearly  $L/L_H = 1.07$ , which is the largest observed (for the same elastic mismatch) of the previous designs, viz. the rotated cubic array and the body-centered cubic array. Therefore, the multi-phase composite design is the best design scheme for increasing crack length of the designs considered (albeit a more complex design due to the multiple inclusion materials); a larger design space of possible inclusion arrangements could result in a design that further improves the toughness but is beyond the scope of this work. Nonetheless, the efficient crack extension method would significantly reduce the computational resources required to sample and analyze the large design space.

## 5. CONCLUSION

New manufacturing methods have enabled a large design space of composites that can be manufactured. In order to search the large space for designs that enhance the

overall toughness of ceramic composites, a computationally efficient crack extension method was developed. The proposed method can be used to predict the fracture behavior of composite designs on the order of seconds (compared to hours when using current approaches such as phase-field modeling), with minimal loss in accuracy. This was demonstrated by comparing the method to LEFM, a phase-field model, and experiments. In particular, the crack extension method was shown to capture the behavior of how nearby inclusions affect the propagation path (and final length) of the crack, which is the main mechanism of interest when designing the composites to increase toughness. Thus, the crack extension method is a useful tool for sampling the large design space of composite arrangements in an efficient manner that lays the groundwork for future optimization studies in order to find the configurations with the largest toughness.

The ability of the crack extension method to analyze different composite arrangements was demonstrated by studying a reduced design space of three different composite arrangements: (1) a rotated cubic array of stiff inclusions used to guide the crack path, (2) a body-centered cubic array of stiff inclusions that resulted in a zig-zag crack pattern that increases crack length, and (3) a cubic array of stiff and soft inclusions that further enhanced the zig-zag behavior.

For each design, the toughness was assessed via the relative crack length increase. In design (1), for elastic mismatch ratios of  $\alpha=2, 5, \text{ and } 10$ , the arrangement should be chosen such that  $R/D = 0.55, 0.67, \text{ and } 0.75$ , respectively, in order to achieve the greatest toughness enhancement for matrix fracture.

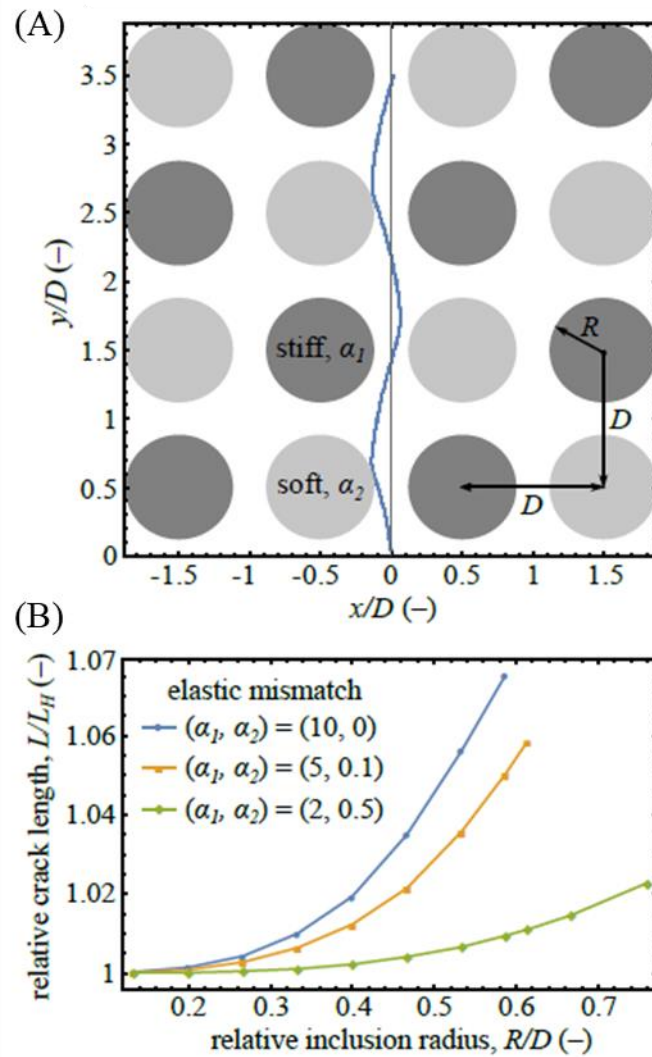


Figure 12. (A) Inclusion arrangement in the multi-phase, cubic composite and resulting crack path. The dark and light shaded circles correspond to the stiff and soft inclusions, respectively. The crack path is denoted by the solid blue line. (B) Plot of relative crack length increase versus inclusion radius for different elastic mismatch ratios.

For design (2), likewise an arrangement with  $R/D = 0.24$  results in the greatest toughening (and is not sensitive to the elastic mismatch ratio). In (3), the inclusion arrangement with greatest matrix fracture toughness depends on  $R/D$ ; for the largest elastic mismatch,  $R/D = 0.6$  is the best design, while for the smallest elastic mismatch,

$R/D = 0.8$  is the best design. Overall, the multi-phase composite demonstrated the greatest toughening for similar material properties compared to the other designs.

These results demonstrate the possibility of controlling crack growth using ordered inclusion arrays, which has been enabled by advanced manufacturing approaches. Furthermore, the computationally efficient crack extension method will aid in uncovering optimal designs of the composites for increasing toughness. Future efforts can utilize this fast-running method to carry out optimization studies where the position of each inclusion is considered as a variable to optimize over in order to span the entire design space.

### ACKNOWLEDGEMENT

The authors acknowledge support from the NSF CMMI Award number 1930881. The authors also thank the Center of Infrastructure Engineering Studies and the Intelligent System Center at the Missouri University of Science and Technology for support.

### REFERENCES

- [1] R. Danzer, "A general strength distribution function for brittle materials," *J. Eur. Ceram. Soc.*, vol. 10, no. 6, pp. 461–472, Jan. 1992.
- [2] A. G. Evans and S. M. Wiederhorn, "Proof testing of ceramic materials: an analytical basis for failure prediction," *Int. J. Fract.*, vol. 26, no. 4, pp. 355–368, Dec. 1984.

- [3] H. Gao, B. Ji, I. L. Jager, E. Arzt, and P. Fratzl, “Materials become insensitive to flaws at nanoscale: Lessons from nature,” *Proc. Natl. Acad. Sci.*, vol. 100, no. 10, pp. 5597–5600, May 2003.
- [4] R. O. Ritchie, M. J. Buehler, and P. Hansma, “Plasticity and toughness in bone,” *Phys. Today*, vol. 62, no. 6, p. 41, 2009.
- [5] A. D’Angio’, J. Zou, J. Binner, H.-B. Ma, G. E. Hilmas, and W. G. Fahrenholtz, “Mechanical properties and grain orientation evolution of zirconium diboride-zirconium carbide ceramics,” *J. Eur. Ceram. Soc.*, vol. 38, no. 2, pp. 391–402, Feb. 2018.
- [6] K. T. Faber and A. G. Evans, “Crack deflection processes—II. Experiment,” *Acta Metall.*, vol. 31, no. 4, pp. 577–584, Apr. 1983.
- [7] K. T. Faber and A. G. Evans, “Crack deflection processes-I. Theory,” *Acta Metall.*, vol. 31, no. 4, pp. 565–576, Apr. 1983.
- [8] R. Miller, M. Ortiz, R. Phillips, V. Shenoy, and E. B. Tadmor, “Quasicontinuum models of fracture and plasticity,” *Eng. Fract. Mech.*, vol. 61, pp. 427–444, 1998.
- [9] C. Van Hoy, A. Barda, M. Griffith, and J. W. Halloran, “Microfabrication of ceramics by co-extrusion,” *J. Am. Ceram. Soc.*, vol. 81, no. 1, pp. 152–158, Jan. 2005.
- [10] Z. Li and Q. Chen, “Crack-inclusion interaction for mode I crack analyzed by Eshelby equivalent inclusion method,” *Int. J. Fract.*, vol. 118, no. 1, pp. 29–40, Nov. 2002.
- [11] L. Yang, Q. Chen, and Z. Li, “Crack-inclusion interaction for mode II crack analyzed by Eshelby equivalent inclusion method,” *Eng. Fract. Mech.*, vol. 71, no. 9–10, pp. 1421–1433, Jun. 2004.
- [12] M.-Y. He and J. W. Hutchinson, “Kinking of a crack out of an Interface,” *J. Appl. Mech.*, vol. 56, no. 2, pp. 270–278, Jun. 1989.
- [13] T. L. Anderson, “Fracture mechanics: fundamentals and applications,” *Angew. Chemie Int. Ed.*, 2001.
- [14] M. L. Williams, “On the stress distribution at the base of a stationary crack,” *J. Appl. Mech.*, vol. 24, no. 1, pp. 109–114, 1956.
- [15] B. Cotterell, “On brittle fracture paths,” *Int. J. Fract. Mech.*, vol. 1, no. 2, pp. 96–103, Jun. 1965.
- [16] H. Ming-Yuan and J. W. Hutchinson, “Crack deflection at an interface between dissimilar elastic materials,” *Int. J. Solids Struct.*, 1989.

- [17] J. C. Lambropoulos, "Shear, shape and orientation effects in transformation toughening," *Int. J. Solids Struct.*, vol. 22, no. 10, pp. 1083–1106, 1986.
- [18] I. D. M., "C. S. Hutchinson 1974. Laboratory Handbook of Petrographic Techniques. xxvii+527 pp., 146 figs. Wiley & Sons, New York, London, Sydney, Toronto. Price £10.60.," *Geol. Mag.*, vol. 112, no. 1, pp. 108–108, Jan. 1975.
- [19] J. D. Eshelby, "The elastic energy-momentum tensor," *J. Elast.*, vol. 5, no. 3–4, pp. 321–335, Nov. 1975.
- [20] R. Twickler, M. Twickler, and W. Dahl, "Two- and three-dimensional elastic-plastic stress analysis for a double edge notched tension specimen," *Eng. Fract. Mech.*, vol. 24, no. 4, pp. 553–565, 1986.
- [21] J. Helsing, "Stress intensity factors for a crack in front of an inclusion," *Eng. Fract. Mech.*, vol. 64, no. 2, pp. 245–253, 1999.
- [22] C. Wang, W. Libardi, and J. B. Baldo, "Analysis of crack extension paths and toughening in a two phase brittle particulate composite by the boundary element method," *Int. J. Fract.*, vol. 94, no. 2, pp. 177–188, Nov. 1998.
- [23] T. Fett, E. Diegele, and G. Rizzi, "Calculation of stress fields near inclusions by use of the fracture mechanics weight function," *Eng. Fract. Mech.*, vol. 53, no. 1, pp. 17–22, 1996.
- [24] P. Lipetzky and Z. Knesl, "Crack-particle interaction in a two-phase composite Part II: crack deflection," *Int. J. Fract.*, vol. 73, no. 1, pp. 81–92, Aug. 1995.
- [25] G. T. M. Stam, E. van der Giessen, and P. Meijers, "Effect of transformation-induced shear strains on crack growth in zirconia-containing ceramics," *Int. J. Solids Struct.*, vol. 31, no. 14, pp. 1923–1948, 1994.
- [26] G. C. Sih, P. D. Hilton, and R. P. Wei, "Exploratory development of fracture mechanics of composite systems." 1970.
- [27] A. A. Griffith, "The phenomena of rupture and flow in solids," *Philos. Trans. R. Soc. London. Ser. A, Contain. Pap. a Math. or Phys. Character*, vol. 221, no. 582–593, pp. 163–198, Jan. 1921.
- [28] B. Bourdin, G. A. Francfort, and J.-J. Marigo, "The variational approach to fracture," *J. Elast.*, vol. 91, no. 1–3, pp. 5–148, Apr. 2008.
- [29] C. Miehe, F. Welschinger, and M. Hofacker, "Thermodynamically consistent phase-field models of fracture: Variational principles and multi-field FE implementations," *Int. J. Numer. Methods Eng.*, vol. 83, no. 10, pp. 1273–1311, 2010.

- [30] G. Hilmas and J. Watts, "Tailoring the properties of ceramic-based composites using co-extrusion processing," in *11th International Ceramics Congress*, 2006, vol. 45, pp. 1385–1393.
- [31] K. Makarian, S. Santhanam, and Z. N. Wing, "Coefficient of thermal expansion of particulate composites with ceramic inclusions," *Ceram. Int.*, vol. 42, no. 15, pp. 17659–17665, Nov. 2016.
- [32] E. W. Neuman, G. E. Hilmas, and W. G. Fahrenholtz, "Processing, microstructure, and mechanical properties of zirconium diboride-boron carbide ceramics," *Ceram. Int.*, vol. 43, no. 9, pp. 6942–6948, Jun. 2017.
- [33] D. J. GREEN, "Stress-induced microcracking at second-phase inclusions," *J. Am. Ceram. Soc.*, vol. 64, no. 3, pp. 138–141, Mar. 1981.
- [34] A. L. Els, "Development and characterization of spiral additions in a ceramic matrix," Missouri University of Science and Technology, 2014.
- [35] G. H. Hilmas, W. Fahrenholtz, and J. Watts, "Method for toughening via the production of spiral architectures through powder loaded polymeric extrusion and toughened materials formed thereby." Google Patents, 2012.

## **II. A COMPARATIVE STUDY OF EXTRUSION DEPOSITION OF SHORT, LONG, AND CONTINUOUS CARBON FIBER REINFORCED COMPOSITES FOR LARGE-SCALE ADDITIVE MANUFACTURING**

Aditya R. Thakur <sup>1</sup>, Ming C. Leu <sup>1</sup>, Xiangyang Dong <sup>1\*</sup>

<sup>1</sup> Department of Mechanical and Aerospace Engineering, Missouri University of Science and Technology, 400 W. 13th St., Rolla, MO 65409.

\* Corresponding author

### **ABSTRACT**

Fiber reinforced thermoplastic composites have been widely investigated due to their ease of processability and recyclability. The advent of high-performance polymers along with high strength, high modulus reinforcing fibers allow these composites to be used for structural applications; while contemporary additive manufacturing (AM) approaches have facilitated their customized, cost-effective fabrication. As a part of this study, a comparative analyses establishing the feasibility of extrusion deposition AM approach to fabricate short fiber reinforced (SFRC), long fiber reinforced (LFRC) and continuous fiber reinforced (CFRC) thermoplastic composites was conducted. A high deposition rate was achieved by the implementation of a single-screw extruder, which directly uses thermoplastic pellets and continuous fiber tows as feedstock materials. Thus, the proposed method was also used as a large-scale additive manufacturing (LSAM) method for printing large-volume components. Using polylactic acid (PLA) pellets and continuous carbon fiber tows, the feasibility of the proposed AM method was investigated through the printing of fiber reinforced composite samples and was further

demonstrated by fabricating large-volume components with complex geometries. The printed samples were compared against their pure thermoplastic counterparts via mechanical tests and microstructural analyses. For flexural strength, there was a steady increase observed in the samples with increasing reinforcing fiber length with SFRC, LFRC, and CFRC reporting flexural strength increment of 11%, 28%, and 52%, respectively, compared to their pure thermoplastic counterpart. Discontinuous short carbon fibers with an average length of 0.3 mm, and long carbon fibers with an average fiber length of 20.1 mm, were successfully incorporated into the printed SFRC and LFRC samples, respectively. The carbon fiber orientation, distribution of fiber length, and dispersion of fiber as well as porosity were further studied through microstructural analyses. The carbon fibers were highly oriented along the printing direction with a uniformly distributed fiber reinforcement across the SFRC and LFRC cross sections. With high deposition rate (up to 0.8 kg/hr) and low material costs (<\$10/kg), this study demonstrated the potentials of the proposed printing method in LSAM of high strength polymer composites reinforced with short, long as well as continuous carbon fibers.

*Keywords: Additive manufacturing, Carbon fiber reinforced composites, High deposition rates.*

## **1. INTRODUCTION**

Thermoplastic polymers have been of growing interest in applications over a large spectrum of consumer and industrial products due to their manufacturing flexibility and recyclability. Specifically, fiber reinforced thermoplastic composites are being

extensively used due to the strength, modulus and weight advantage they provide over their polymer counterparts [1]–[3]. With increasing demands, several manufacturing processes that facilitate large-scale, customized fabrication of fiber reinforced composite parts have been developed, including but not limited to 3D printing, machining, casting, extrusion, molding, etc. Molding is one of the most widely used fabrication approaches for large-scale, tight-tolerance, complex fiber reinforced composite parts but with high manufacturing costs [3]. Additive manufacturing (AM) approaches, e.g., fused deposition modelling (FDM), offer flexible, tool-less and mold-less fabrication processes [4]. Until recently, due to low printing speeds and long fabrication time, AM was mainly limited to printing low-volume components [5]. Advancements in large-scale additive manufacturing (LSAM) have addressed these shortcomings to a certain degree [5]–[8]. Previous studies showed that LSAM with high material deposition rates allowed additive fabrication of large-volume parts without excessive printing time, while reinforcing with fiber additives helped in elevating mechanical performances of the printed parts [9]–[11].

The mechanical and physical properties of fibrous composites largely depend on their reinforcing fiber orientation and length-to-diameter aspect ratio as well as interfacial bonding [12]–[15]. Increasing fiber length typically promoted mechanical properties, such as strength, modulus, impact resistance and wear resistance [2], [16]–[18]; however, processing of these composites becomes increasingly difficult [2], [13]. Nano- and micron-sized [19]–[21], short [22], [23], long [24] and continuous fiber reinforced composites using filament-based FDM approaches [25]–[28] have been extensively studied. The material costs in these manufacturing approaches are relatively high as they need to use specialized fiber reinforced filaments as raw material for fabrication [29].

Low-cost AM of continuous fiber reinforced composites (CFRC) using thermoplastic pellets and continuous fibers has been recently investigated [14], [30]. CFRC filaments were first in-situ prepared from continuous fibers via micro-screw extrusion and then directly used by FDM methods to print CFRC parts. However, these processes were impractical for fabrication of large-volume components, which usually take several hours, or even days, to finish due to low deposition rates (about 0.5 g/min) [27], [31]. Meanwhile, despite high material deposition rates, LSAM of fiber reinforced composites using pellet-based FDM has been limited to short fiber reinforcement [11]. Only a modest improvement in mechanical strength (about 20%) has been achieved compared to thermoplastic counterparts. No previous work can be identified on directly using and comparing continuous or discontinuous reinforcing carbon fibers in LSAM. Typically, CFRC is mechanically superior as it offers longer reinforcing fiber lengths [25]–[28]. However, difficulties in processing of fiber reinforced composites also increase with an increase in fiber length [2]. Inadequate impregnation poses challenges in preparing high-quality CFRC and necessitates post-processing to take advantage of continuous fiber reinforcements [14], [32], [33]. In comparison, long fiber reinforced composites (LFRC) with high-aspect-ratio fibers can provide improved mechanical performance, almost comparable to CFRC samples, while minimizing fabrication limitations related to CFRC, like continuous printing tool-path.

Conventional methods use extrusion of either fiber reinforced pellets or direct fiber injection molding to fabricate fiber reinforced composite parts. It was found that highly oriented fibers in the flow direction with high-aspect-ratio resulted in improved mechanical properties [13]. The randomness of fiber distribution and orientation

increased with an increase in number of processing stages [9]. Meanwhile, high shear forces during these processes resulted in reduction in fiber length by 70%-90% [34]. Thus, single stage processing was preferably used to fabricate high-strength fiber reinforced parts. In this study, a new AM method was proposed to print short fiber reinforced composite (SFRC), LFRC and CFRC parts by combing single-stage extrusion and deposition processes. Continuous fiber tows and thermoplastic pellets were used as feedstock materials. A singular fabrication set-up was used to AM pure thermoplastic, SFRC, LFRC and CFRC components with minor modifications to the employed single-screw extruder set-up. For pure thermoplastic and SFRC samples, respective processed pellets were used. During the printing process of LFRC samples, the continuous fiber bundles were directly fed into the extruder and were chopped into long fibers by the shearing forces of a single-screw extruder prior to being coextruded with the thermoplastic melt and then deposited layer-by-layer on a print bed. CFRC samples were fabricated through in-nozzle impregnation of continuous fiber bundles prior to layer-by-layer deposition on a print bed. Continuous carbon fiber tows and polylactic acid (PLA) pellets were used to investigate the feasibility of the proposed new AM method. Mechanical tests and microstructural analyses were carried out to contrast and compare the mechanical properties and microstructure of the printed SFRC, LFRC and CFRC samples against their pure thermoplastic counterparts.

## 2. EXPERIMENTAL PROCEDURE

### 2.1. MATERIAL PREPARATION

In this study, commercially available pure PLA pellets (4043D by Filabot) were used as thermoplastic matrix materials. 3K carbon fiber tows (3000 fibers in a bundle, AS4C by Hexcel) were mainly used as reinforcement fibers. The PLA pellets were dried in a vacuum oven at 85 °C for at least four hours to eliminate moisture before printing as the presence of moisture could hydrolyze PLA in the melt phase. This in turn reduces its molecular weight, which negatively affects the end-product quality and subsequent mechanical properties of the printed samples [35]. Thorough drying of PLA pellets also assists in minimizing the presence of bubbles in the thermoplastic deposition [36]. Similarly, the carbon fiber tows were dried in a vacuum oven at 120 °C for at least four hours to remove moisture, to minimize the probability of fiber clumping during extrusion. Clumping, aggravated by presence of moisture in the fibers, is detrimental to the deposition quality and subsequently the mechanical properties of the printed fiber reinforced samples [37].

Nature of fiber reinforcement within the CFRC, as the name suggest, is continuous. Thus, is easily distinguishable amongst LFRC and SFRC samples. On the other hand, the critical fiber aspect ratio  $(l/d)_c$  determines whether the sample is distinguished as LFRC or SFRC. When the length of the discontinuous reinforcing fibers within the deposition exceed the critical fiber ratio, they are categorized as LFRC, otherwise the deposition is deemed as SFRC. This critical fiber aspect ratio is given by

$$\left(\frac{l}{d}\right)_c = \frac{\sigma_{fu}}{2\tau} \quad (1)$$

where  $l$  and  $d$  are the carbon fiber length and diameter, respectively.  $\sigma_{fu}$  denotes the ultimate tensile strength of the carbon fibers, and  $\tau$  represents the interfacial shear strength between the fiber and the PLA matrix materials. For the selected carbon fiber tows (AS4C by Hexcel) [38],  $d$  and  $\sigma_{fu}$  were 7  $\mu\text{m}$  and 4.7 GPa, respectively. Thus, the fiber-matrix interfacial bonding determined the critical carbon fiber length needed to be achieved for the LFRC samples. With an estimate of interfacial shear strength of  $\sim 5.0$  MPa [39] for extrusion processes, a critical carbon fiber length of  $\sim 3.3$  mm needs to be at least achieved in the printed LFRC samples. With the estimated critical value, it would be worth further studying the carbon fiber length within the printed samples.

To manufacture LFRC and CFRC samples, the commercial pellets and continuous fiber tows are directly employed during fabrication. For SFRC, the fiber length is required to be maintained lower than the critical fiber length of 3.3 mm. In order to enforce this criteria, SCFR pellets were prepared in-house using the same materials employed in CFRC and LFRC sample fabrication to facilitate direct comparison.

To prepare the SCFR PLA pellets, the commercial PLA pellets were dissolved in 1:10 volume ratio of anhydrous Dichloromethane (DCM) solvent (by Sigma-Aldrich) by agitating vigorously using a magnetic stirrer. The carbon fiber tows were chopped to 3.2 mm in length, to retain SFRC nature of the composite, similar to the compounding and pellet production method reported by Zhong et al. [40] and Takinalp et al. [41] before adding to the agitating solution of PLA and DCM. Mixture with 6 vol.% ( $\sim 8.5$  wt.%) CF was prepared to facilitate adequate dispersion of short carbon fibers within the PLA. After mixing for 8 hours, the mixture was left to dry under a fumed hood at ambient temperature and pressure until all the DCM was completely evaporated and a PLA plate

with short carbon fiber reinforcement was obtained. This plate was palletized and later used to fabricate SFRC structures. The pellets were stored in a vacuum oven at 80 °C to eliminate presence of moisture which is known to be detrimental for printing [35].

## **2.2. EXPERIMENTAL SETUP**

The experimental setup primarily included a single-screw extruder with a conical print nozzle (4 mm inner diameter), and a multi-axis machine (Galaxy G by Automated Precision Inc.). A high torque motor was used to drive the extrusion process as controlled by its rotation speed. An acrylic print bed was employed as a substrate to deposit fiber reinforced composites upon. It should be noted that the thermoplastic nature of the acrylic print bed promoted adhesion between the deposited samples and the print bed. Moreover, the presence of conductive carbon fibers within the deposition was known to reduce the coefficient of thermal expansion (CTE), which in turn minimized thermal contraction and thus warping of the deposited samples [42]. Reduced CTE with increased stiffness due to the fibers made the acrylic print bed a viable substrate without requiring additional setup, e.g., heated substrate bed. This primary AM set-up was slightly modified to facilitate printing of variety of fiber reinforced composites. Figure 1(A), (B), and (C) illustrates the schematics of the set-up used for SFRC, LFRC and CFRC samples, respectively.

The setup to fabricate SFRC samples could also be directly used to AM pure thermoplastic samples, as long as appropriate pellets are used. For SFRC samples, as illustrated in Figure 1(A), the prepared SCFR PLA pellets were directly fed through the hopper. During extrusion, the SCRF PLA pellets were melted by the heater while simultaneously being acted upon by extrusion-screw inducing shearing forces. The PLA

melt and the reinforcing short carbon fibers were further mixed as they were fed through the extruder and coextruded out through the print nozzle.

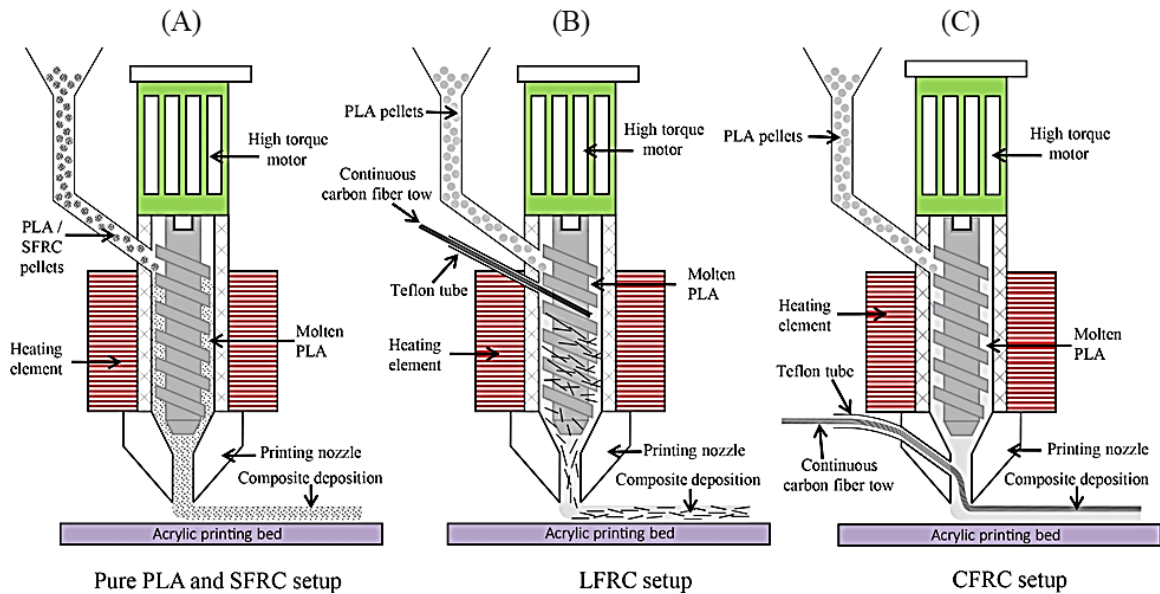


Figure 1. Schematic of the AM setup to fabricate (A) SFRC/pure thermoplastic, (B) LFRC, and (C) CFRC samples.

The PLA-short carbon fibers mixture was then deposited on the print bed as the vertically mounted extruder followed the toolpath and printed the SFRC samples layer-by-layer. The material extrusion and deposition rates were controlled by the extruder screw rotation speed, as represented by revolution per minute (RPM) at a given melt temperature.

For LFRC samples, the pure thermoplastic pellets, i.e., PLA pellets in this study, were fed through the hopper while continuous carbon fiber tows, guided by a feeding tube, were fed into the extruder through a vent hole on the extruder as illustrated in Figure 1(B). During extrusion, the thermoplastic pellets were melted by the heater while

the continuous carbon fiber tows were chopped down into discontinuous long carbon fibers by the extrusion-screw induced shearing forces. The PLA melt and long carbon fibers were further mixed as they were fed through the extruder and coextruded out through the print nozzle. The PLA-long fibers mixture was then deposited on the print bed as the vertically mounted extruder followed the toolpath and printed the LFRC samples in 3D space. The material extrusion and deposition rates, similar to pure thermoplastic and SFRC samples, is controlled by the extruder screw RPM at a given melt temperature.

The extrusion processes were expected to facilitate orientation of the reinforcing fibers in the print direction during deposition, for both SFRC and LFRC samples, owing to the shear and the melt flow induced fiber alignment [43]–[47], which was further examined through microstructural analyses.

Meanwhile, as seen in Figure 1(C), if the continuous carbon fiber tows were directly impregnated through the print nozzle instead of the vent hole on the extruder, following the previous studies [25], [27], CFRC can be printed using the proposed experimental setup using a modified printing nozzle. The following Figure 2 depicts the in-nozzle impregnation and deposition process which occurs for CFRC samples in the proposed AM method.

Preliminary parametric studies were first performed to find optimal printing parameters. The print temperature, layer thickness, material deposition rate, and print speed would affect the quality of the printed samples [27], [48].

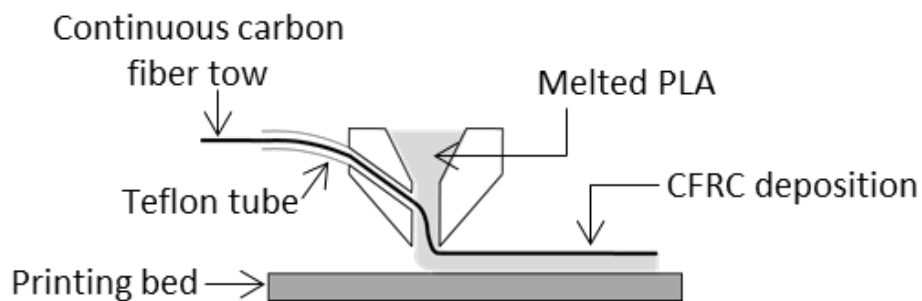


Figure 2. Schematics of setup used in preparation of continuous carbon fiber reinforced composites.

A print temperature of 190 °C was found to allow sufficient viscosity for the PLA melt to provide drag force to coextrude carbon fibers at a wide range of extruder RPMs and print speeds. A layer thickness of 1 mm was used to ensure sufficient contact pressure to avoid delamination between deposition layers [27]. The extruder screw rotation speed was selected as 200 RPM, with a calibrated extruder material output rate, i.e., a deposition rate of 3.3 g/min, six times higher than the deposition rates (e.g., 0.17 g/min-0.46 g/min [27]) typically achieved by the filament-based FDM processes. It is worth noting that as the deposition rates were controlled by the extruder-screw rotation speed, the deposition rate can be easily scaled up to a higher value at a higher RPM, e.g., 833.3 g/min as reported in previous studies for LSAM [49]. The constant deposition rate of 3.3 g/min was employed in this study to explore the printed composite parts using the proposed method with a print speed of 200 mm/min. Under these condition, pure PLA, SFRC, LFRC, and CFRC samples were fabricated for mechanical and microstructural analyses. The feasibility of the proposed process was further demonstrated through printing large-scale composite samples with complex geometries at a higher deposition rate of 13.3 g/min.

### 2.3. MECHANICAL AND MICROSTRUCTURE CHARACTERIZATION

The printed samples were studied through mechanical testing and microscopic observation across their cross sections. ASTM standard D7264/D7264M-15 was followed to measure the mechanical properties, specifically the flexural strength and modulus of the additively fabricated pure PLA, SFRC, LFRC, and CFRC samples via three-point bending tests. Rectangular bars with dimensions of 50 mm × 8 mm × 8mm were fabricated using the proposed setup by the aforementioned printing parameters. Flexural strength and modulus were determined using the three-point bending method on an Instron 5881 machine with a support span of 40 mm, as shown in Figure 3 using LFRC sample as an example. Three specimens of each type of samples were tested at a cross-head speed of 1 mm/min.

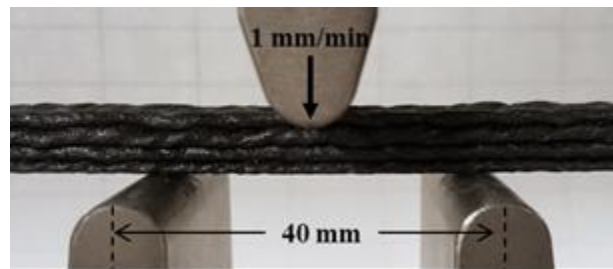


Figure 3. Three-point bending test set-up with LFRC sample used for demonstration.

To characterize the fiber length distribution and the fiber orientation within the thermoplastic matrix, the additively fabricated parts were first cut using a low-speed diamond saw both perpendicular to the print direction to obtain the transverse cross section for studying fiber distribution, and along the print direction to obtain the longitudinal cross section for studying the fiber orientation. The samples were then

mounted within VariDur acrylic materials before polishing. The cross sections were polished using resin bonded diamond discs between 220 and 1200 grit size, followed by diamond films between 3 $\mu\text{m}$  to 0.25  $\mu\text{m}$ . A Hirox Digital KH-8700 optical microscope was used to examine the polished samples for the fiber orientation and the distribution study. It is worth noting that with adequate polishing, the high transparency of the selected PLA matrix materials facilitated characterization of reinforcing carbon fibers. Hitachi TM-1000 Scanning Electron Microscope was used for void fraction analyses.

To determine the carbon fiber volume fraction and the fiber length distribution in the composite samples, the weight of the printed samples was first measured. The samples were repeatedly rinsed with dichloromethane (DCM) solvent until all the PLA matrix material was dissolved and rinsed away, and only the carbon fiber inclusions remained. The weight of the remaining carbon fiber inclusions was then measured. Once knowing the densities of carbon fibers and PLA, the carbon fiber volume fraction  $V_f$  can be obtained as,

$$V_f = \frac{W_f}{\rho_f} \left( \frac{1}{\frac{W_f}{\rho_f} + \frac{W_m}{\rho_m}} \right) \quad (2)$$

where  $W_f$  and  $W_m$  represent the weights of the fiber reinforcements and the matrix materials, respectively. The densities of the continuous carbon fiber reinforcements ( $\rho_f$ ) and the PLA matrix materials ( $\rho_m$ ) were taken as 1.24 g/cm<sup>3</sup> and 1.78 g/cm<sup>3</sup>, respectively, for the selected carbon fiber tows (AS4C by Hexcel) [38] and PLA pellets (4043D by Filabot) [50] in this study. The obtained carbon fiber strands were also further examined under optical microscope to measure fiber length distribution through the image analysis software, ImageJ.

### 3. RESULTS AND DISCUSSION

The feasibility of the proposed method in printing fiber reinforced composite parts was investigated through comparing the mechanical properties with those of pure PLA samples measured by three-point bending tests. Microstructural analysis was further carried out to characterize the fiber distribution, fiber orientation, and the length of the reinforcing fibers within the samples. Large-scale fiber reinforced composite components with complex geometries were also printed to demonstrate the applications of the proposed approach.

#### 3.1. MORPHOLOGY COMPARISON OF THE PRINTED SAMPLES

Using the above experimental setup, pure thermoplastic, SFRC, LFRC, and CFRC were printed with typical sample morphology shown in Figure 4(A), (B), (C) and (D), respectively. With no fibers, pure PLA samples of relatively good resolution could be obtained over a large range of material deposition rates and print speeds. In comparison, under the same conditions, SFRC, LFRC and CFRC samples with relatively uniform geometries were printed but with worse printing resolution compared to the pure PLA samples. Fiber reinforced composites were more susceptible to fiber dislocation, pull-out, matrix overflow, and lack of matrix materials [27] during the printing processes. Difficulties in processing of composites increased [2][34] with an increase in fiber length. Compared to the SFRC and LFRC samples, the carbon fibers, seen as dark phases in Figure 4, were obviously non-uniformly distributed within the CFRC samples. The heterogeneity in fiber distribution could potentially lead to a higher degree of defects and

voids in the printed samples and thus worsen the mechanical properties of the printed samples as further discussed below. For the SFRC and LFRC samples, fiber dislocation and pull-out would be minimized because of discontinuity in carbon fibers. The fiber strands would in general be well dispersed within the matrix materials during extrusion [51] as shown from the printed SFRC and LFRC samples in Figure 4(B) and (C). It is worth noting that despite a constant layer thickness used, an obvious variation in printed layer thickness was noticed for the LFRC samples in Figure 4(C). This was found to be mainly related to the unique heterogeneity introduced by the discontinuous long fiber reinforcement. As further discussed below, despite a relatively uniformly dispersed carbon fibers, a wide variation in carbon fiber length resulted in poorer print resolution and surface anomalies for certain deposition layer, thus leading to the variation in layer thickness.

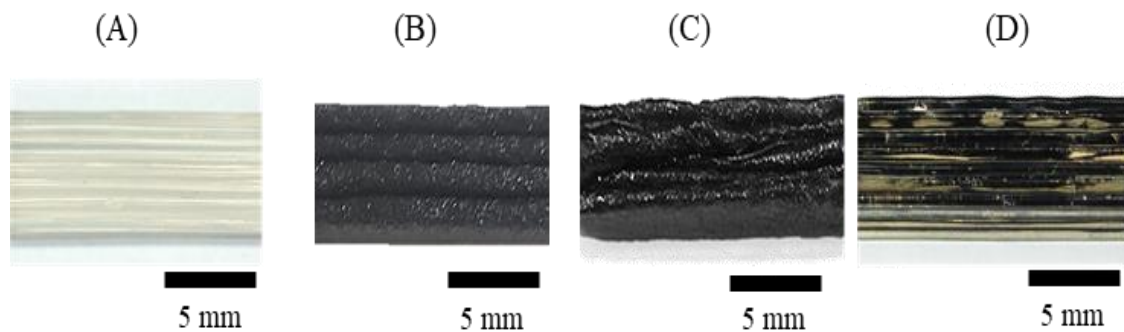


Figure 4. A direct comparison of additively manufactured (A) pure PLA, (B) SFRC, (C) LFRC, and (D) CFRC samples printed at printing parameters exhibiting acceptable printing resolution and consistent layer deposition.

### 3.2. PRINTED SAMPLES

The mechanical properties of the printed SFRC, LFRC and CFRC samples in Figure 4 were further studied in comparison with pure PLA samples via three-point bending tests. The measured stress-strain curves are plotted in Figure 5, where the results of all the three measured LFRC samples are shown. As relatively smaller variations were observed for pure PLA, SFRC, and CFRC samples; thus, only a singular result for each is included in Figure 5. For clarification, further details on mechanical properties of all the printed samples is summarized in Figure 6, where three samples were tested for each type, i.e., PLA, SFRC, LFRC, and CFRC. As expected, with no fiber reinforcement, the PLA samples showed the lowest mechanical strength. The LFRC samples exhibited mechanical behavior close to the CFRC samples. A large variation in the measured mechanical properties for the LFRC samples was observed, with one case showing a maximum stress nearly comparable to that of the CFRC samples.

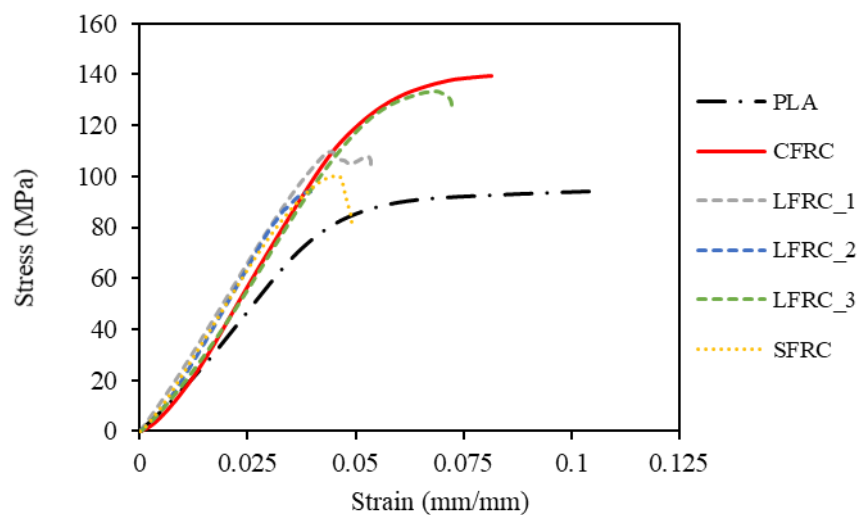


Figure 5. Measured stress and strain data through three-point bending tests on pure PLA, SFRC, LFRC and CFRC samples.

Mechanical behavioral trends observed via measured flexural strength and modulus is detailed in Figure 6. Evidently, increase in reinforcing fiber lengths correlated with increase in strength of the fiber reinforced samples. With the introduction of short fiber and long fibers as reinforcement, an average 11% and 28% improvement in the flexural strength, respectively, was achieved over the pure PLA samples. Meanwhile, CFRC samples were reportedly 52% stronger than their thermoplastic counterparts. This may be attributed to the continuous nature of the reinforcing fibers for the CFRC samples. In contrast, the measured average modulus of SFRC samples incremented by 36% compared to pure PLA samples. Whereas, for the LFRC samples the average modulus was comparable to that of the CFRC samples, increased by 50% over the pure PLA samples; in fact slightly higher (3% on average) than that of the CFRC samples.

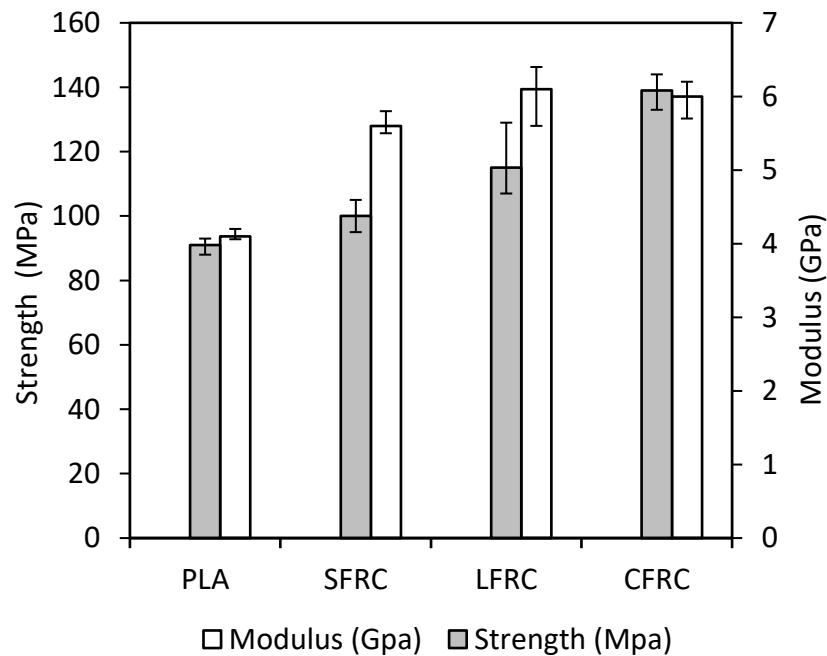


Figure 6. Comparison of measured flexural strength and modulus between pure PLA, SFRC, LFRC and CFRC samples.

The high modulus of the printed LFRC samples could be attributed to highly oriented long carbon fibers that were discontinuous but well distributed within the PLA matrix materials. The discontinuity of carbon fiber reinforcement also lowered the possibility of void formation and formed a strong fibrous reinforcement, more effectively stiffening the composites, compared to the typically concentrated continuous carbon fibers within the printed CFRC samples [27], [28]. On the other hand, previous studies [2], [13], [52] showed that the stiffness of the fiber reinforced composites increased with an increase in the aspect ratio of reinforcing fibers until a critical aspect ratio was reached. Beyond that, the stiffness remained constant irrespective of further increase in the length of the reinforcing fibers. Hence, the modulus was observed to be lowest for SFRC samples amongst composites, unable to meet the critical aspect ratio. On the other hand comparable modulus of the LFRC and CFRC composites could be attributed to the fact that a critical fiber aspect ratio  $(l/d)_c$  was reached in the LFRC samples, coupled with lower tendency for void formation as illustrated later during microstructural analyses.

It can also be observed in Figure 5 and Figure 6 that compared to that of PLA and CFRC samples, a relatively larger variation was observed for the LFRC samples in both flexural strength and modulus. The flexural strength of the LFRC samples could fluctuate anywhere from a moderate improvement over the PLA samples, all the way up to almost being comparable to the CFRC samples. While the variation was partially attributed to the relatively poorer resolution in the printed LFRC samples, previous studies [2], [13] showed that a larger variation in fiber length and orientation introduces inconsistencies in the mechanical performance of the LFRC samples, which was especially true for the

composite samples reinforced with fibers of high aspect ratios. Thus, making it necessary to further examine the microstructure of the printed composites in terms of fiber length, fiber orientation, and fiber distribution.

### **3.3. MICROSTRUCTURAL CHARACTERIZATION**

**3.3.1. Carbon Fiber Distribution.** The distribution of the fibers within the printed composites directly correlates with their mechanical properties [53]. Thus, the microstructure of the printed SFRC, LFRC and CFRC samples were first examined to characterize the fiber distribution across the transverse and the longitudinal cross sections. Figure 7(A) and (B) shows the polished transverse cross section of a single SFRC and LFRC deposition layers, respectively. The carbon fibers were relatively uniformly distributed across the whole cross section. This showed a clear difference compared to the fiber distribution within the CFRC samples as illustrated in Figure 7(C), where continuous carbon fibers tend to concentrate within the top region of each deposition layer [27], [28]. Also, no obviously large voids or defects were observed within the SFRC and LFRC deposition layer, showing well impregnated carbon fibers in the PLA matrix. It was mainly attributed to the shearing forces during extrusion, which simultaneously chopped down carbon fibers and promoted the mixing of the PLA melt and the discontinuous carbon fibers. The high pressure introduced by the extrusion further improved the impregnation of the fibers into the PLA matrix materials.

The dispersion of carbon fiber dots in Figure 7 were further used to quantitatively evaluate the fiber distribution across the transverse cross section [39]. The dots were

converted to an X-Y coordinate system in Figure 8, where  $X_i$  and  $Y_i$  represented the transverse direction and building direction, respectively.

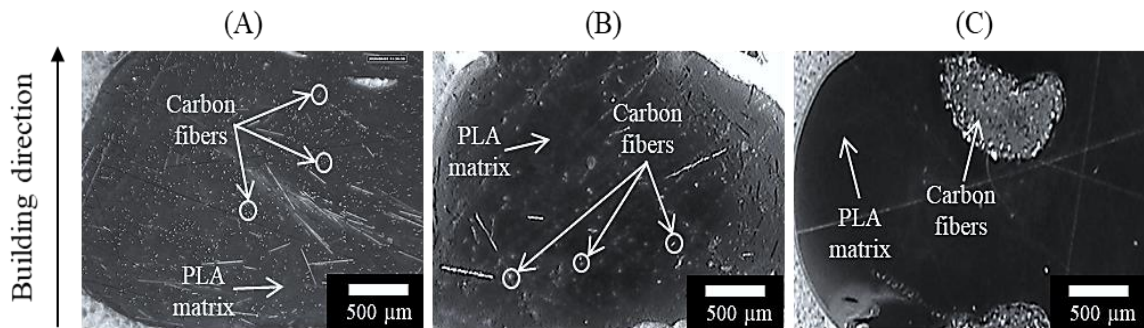


Figure 7. Transverse cross-section of a single deposition layer of the printed (A) SFRC, (B) LFRC, and (C) CFRC samples with highlighted carbon fibers within the PLA matrix.

The cross section was segregated into small grids, called quadrants. The number ( $N$ ) of the marked fiber dots falling into each quadrant ( $X_i, Y_i$ ) were then counted. The count distribution can then be used to quantify the degree of fiber distribution uniformity across the transverse cross section. The fiber dot counts were mapped as shown in Figure 8(A), (B) and (C) for SFRC, LFRC and CFRC samples, respectively. A relatively uniform distribution of carbon fibers was observed for the samples with discontinuous fiber reinforcement, with peak values slightly shifting toward the top region of the deposition layer for LFRC sample. This trend is exaggerated for CFRC samples where the carbon fibers concentrate within the top region of each deposition layer, further incrementing anisotropy within the deposition [27], [28]. A similar trend was observed while examining the longitudinal cross section of the single deposition layer in Figure 9.

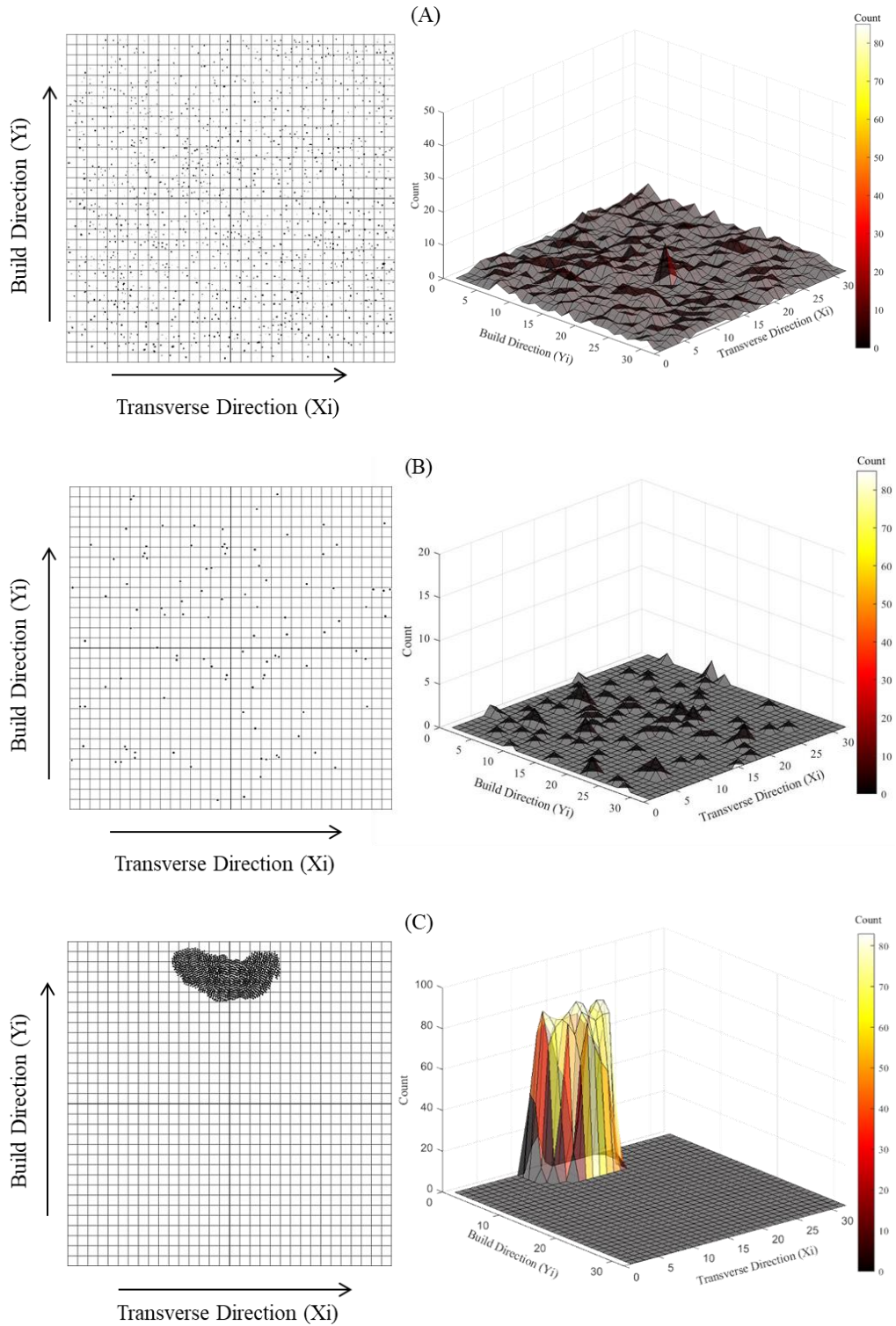


Figure 8. Distribution mapping of carbon fibers (marked dots) across the transverse cross section with the distribution of fiber dot counts in (A) SFRC, (B) LFRC and (C) CFRC composite deposition.

A similar trend was observed while examining the longitudinal cross section of the single deposition layer in Figure 9. For discontinuous fiber reinforcement, the distribution across the deposition width is generally thorough. However, the carbon fibers were more obviously dispersed into the top region of the LFRC deposition layer with over 85 % of the reinforcing long carbon fibers located within the top half deposition width. The difference in the fiber distribution could be attributed to the orientation of the high aspect ratio fibers, part of which were either not aligned in the printing direction or twisted as seen in Figure 9, and thus were not captured by the marked fiber dots in the transverse cross section in Figure 7 and Figure 8. Therefore, the fiber orientation was further studied as discussed below. The conglomerated fibers in LFRC were mainly caused by the drawing forces during the extrusion processes, which directly contributed to the much concentrated fiber bundles as seen in the CFRC samples. However, due to the discontinuity in the fibers for the SFRC and LFRC samples, the fiber distribution was less affected by the drawing forces and showed a higher degree of uniformity.

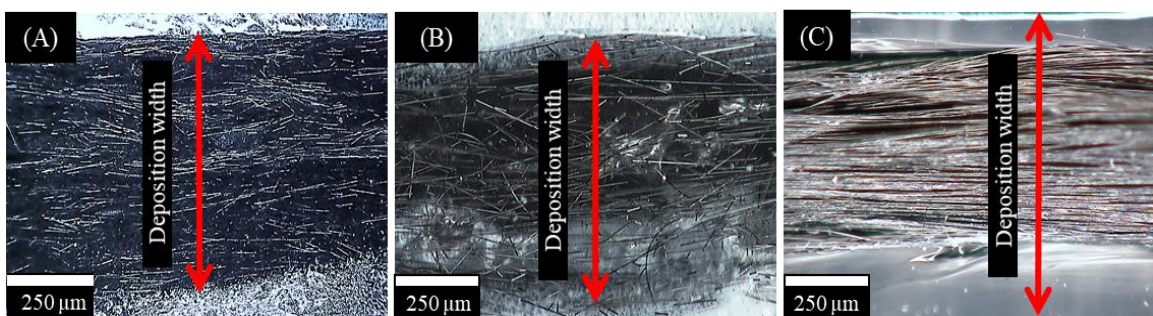


Figure 9. Longitudinal cross-section of each deposition layer of the printed (A) SFRC, (B) LFRC, and (C) CFRC samples with the distribution of carbon fibers (dark phase) within transparent PLA matrix.

**3.3.2. Carbon Fiber Orientation and Length.** To study the fiber orientation distribution, a window of  $1350\ \mu\text{m} \times 1350\ \mu\text{m}$  (typical deposition width) was first selected at three different longitudinal cross sections on three different samples. The fiber orientation angle with respect to the printing direction was obtained for all the fibers within the window. The printing direction was defined as  $0^\circ$ , and the building direction was defined as  $90^\circ$ . The distribution of carbon fiber orientation is shown in Figure 10(A) for SFRC samples and Figure 10(B) for LFRC samples. Since all the fibers for the CFRC samples inherently align in the printing direction and are approximately of the same length as the sample, they are not being illustrated in the following.

For SFRC samples, nearly 32% of the reinforcing fibers orient within 10 degrees of the printing direction, with the longer reinforcing fibers having a higher tendency to either not align in the printing direction and twist at a peculiar 40 degree to 50 degree angle. This could be attributed to the fact that reportedly, with an increment in the fiber length, there is a higher tendency to align on the top region of the deposition layer [27], [28]. This may lead to the observed misalignment of fibers in SFRC samples. This corroborates with the previous observations for LFRC and CFRC samples where as illustrated in Figure 8, with increment in reinforcing fiber aspect ratio, there is an increase in the likeliness of fibers positioning within the top half of the deposition width.

Similarly, for LFRC samples, 69% of the fibers were aligned within  $10^\circ$  with 87% oriented within  $30^\circ$  from the printing direction. Having notably longer fibers compared to SFRC, LFRC samples have fibers that inherently position themselves on the upper half region of the deposition, with shearing and melt flow inducing the orientation of the reinforcing fibers to be in the printing direction during the extrusion processes. For CFRC

samples, with significantly higher fiber aspect ratio, the orientation is entirely within 10 degrees of the printing direction.

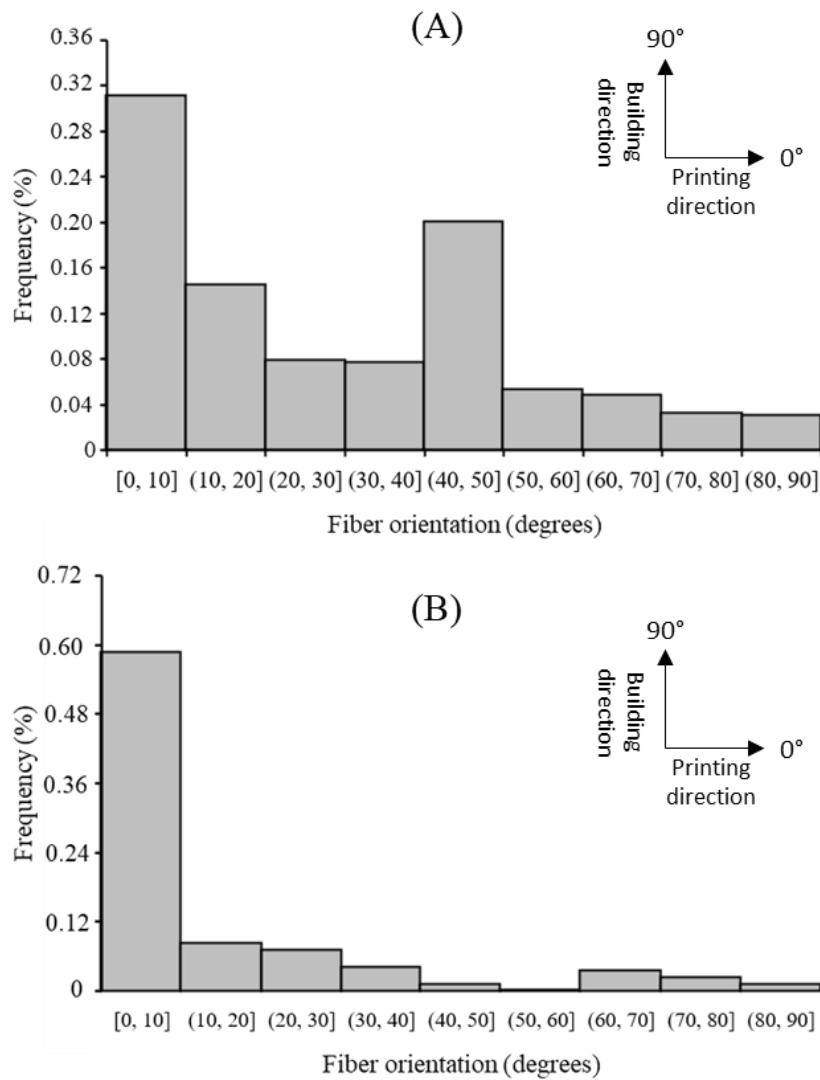


Figure 10. Fiber orientation distribution within the printed (A) SFRC and (B) LFRC samples.

The length of the reinforcing carbon fibers was also measured from the carbon fiber strands obtained after dissolving and removing the PLA matrix materials via DCM.

Weighted histograms were then created to characterize the distribution of carbon fiber length as shown in Figure 11. The histograms were normalized by the total length of all measured carbon fibers, so the height of each bar represented the volume fraction of fiber length within a corresponding range. An average of 0.3 mm fiber length was obtained in the printed SFRC samples, with a maximum of 3.01 mm and a minimum of 6  $\mu\text{m}$  measured.

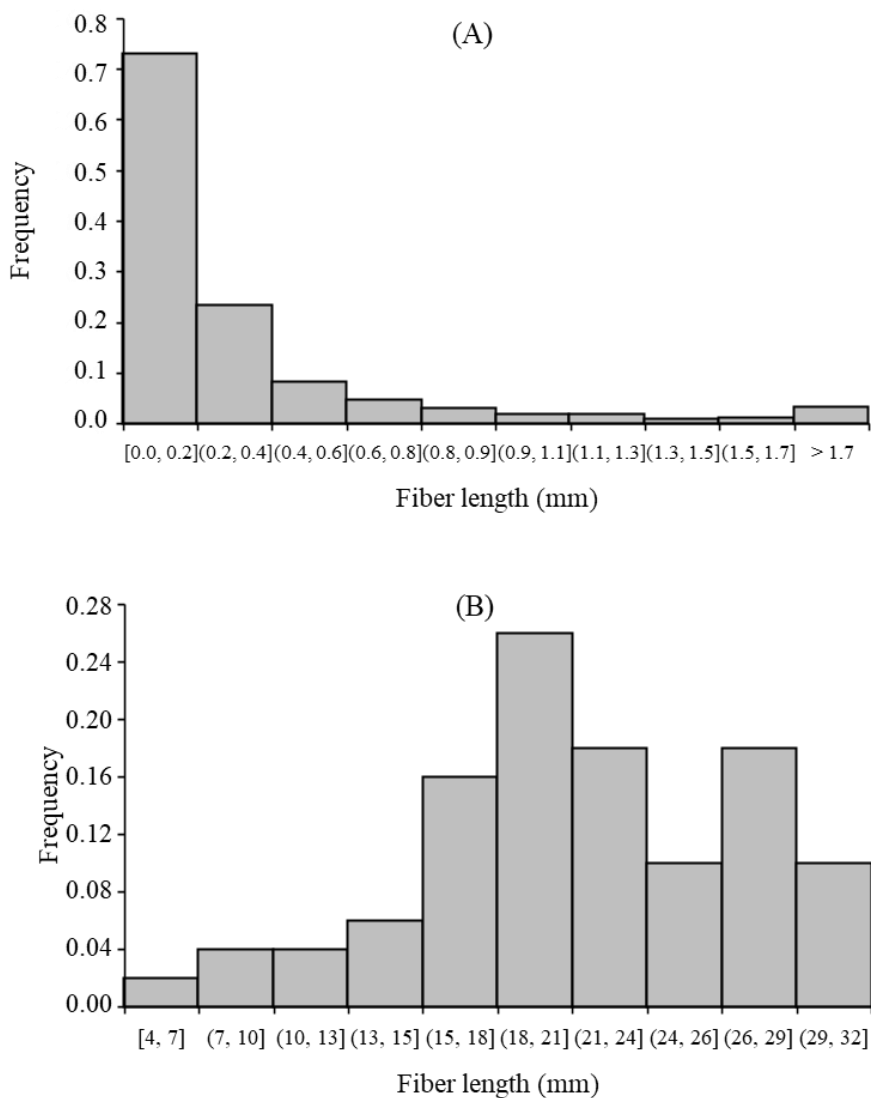


Figure 11. Fiber length distribution within the printed (A) SFRC and (B) LFRC samples.

On the other hand, for LFRC samples, average of 20.1 mm fiber length was obtained, with maximum and minimum measured fiber length of 32.0 mm and 40  $\mu\text{m}$  respectively. A narrow range of fiber length variation was observed in SFRC samples, as illustrated in Figure 11(A) with majority of the fibers being shorter than 0.4 mm in length. On contrary, for LFRC samples, as illustrated in Figure 11 (B), majority of the fibers were measured to be longer than 15 mm, which was much larger than a critical carbon fiber length of 3.3 mm calculated above. Thus, the carbon fiber length was effectively strengthening and stiffening the printed LFRC samples [2], showing a consistently high modulus comparable to that of the CFRC samples in Figure 6. Meanwhile, a large variation in the obtained fiber length led to higher uncertainties in the fiber distribution. In the examination of the carbon fiber strands in LFRC samples, it was found that the singled, untangled fibers were most likely to be less than 170  $\mu\text{m}$  in length, while the fibers exceeding 440  $\mu\text{m}$  were likely to be entangled into conglomerates. With highly oriented carbon fibers, if fewer longer fibers were entangled in the printed samples, a better dispersed fiber reinforcement network would lead to higher mechanical properties. With a majority of the long carbon fibers present in Figure 11(B), carbon fibers had a higher tendency to be entangled and accumulated as conglomerates into the top region in Figure 9(B), which weakened the reinforcing effects of long fibers and increased the heterogeneity, thus leading to a larger variation in printing resolution and layer thickness as well as the flexural strength and modulus seen above, which are closely related to the fiber length. This phenomenon was less prominent for SFRC samples with consistently smaller reinforcing fiber lengths ( $<0.4$  mm) and distribution across the deposition.

Notably different defect patterns were found between the printed SFRC, LFRC and CFRC samples. As shown in Figure 12(A) and Figure 12(B), micron-size voids were found around single carbon fibers for the SFRC and LFRC samples with 6% fibers. In contrast, for the CFRC samples with 6% fibers printed under the same conditions, larger scale voids were observed both around and within the carbon fiber bundle in Figure 12(C). The measured void fraction within the CFRC samples was over four times of that found in the LFRC samples, and nearly nine times higher than SFRC samples, as shown in Figure 13. This also helped explain why the obtained LFRC mechanical properties were close to those of the CFRC samples in Figure 5, despite the discontinuous fibers present in the LFRC samples. The void formation was mainly attributed to the fiber impregnation process during printing, which resulted in different fiber-matrix wetting conditions within the SFRC, LFRC and CFRC samples. As the carbon fiber tows and PLA pellets were nearly fed together in Figure 1, the long shearing and extrusion processes greatly promoted the impregnation of the chopped discontinuous carbon fibers into the PLA melt. Thus, good fiber-matrix wetting conditions were achieved before deposition. In contrast, similar to the previous studies in printing CFRC [25], [27], the carbon fiber tows were directly fed through the print nozzle as seen in Figure 2. A much shorter impregnation time limited the amount of the PLA flowing into the continuous carbon fiber bundles, thus yielding poorer wetting conditions.

The void fraction within the printed LFRC samples was further characterized in terms of the fiber volume fraction. Notably, with a smaller carbon fiber bundle size, lower fiber volume fraction was obtained. Fewer voids were observed, with the void fraction dramatically decreasing with a decrease in fiber volume fraction.

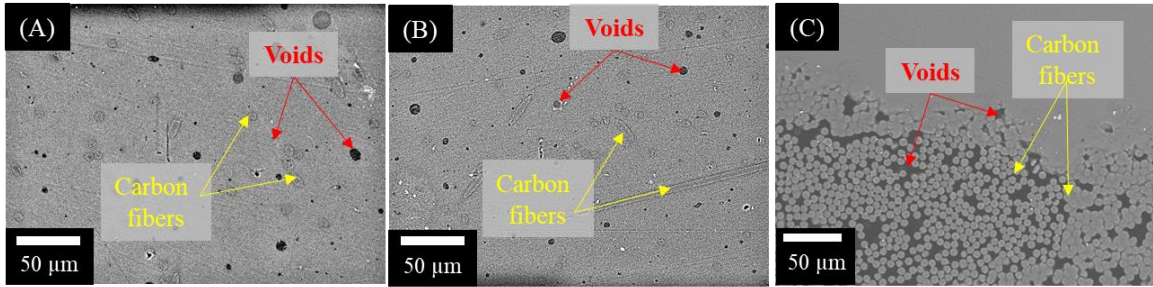


Figure 12. Micrographs illustrating the transverse cross sections of (A) SFRC, (B) LFRC, and (C) CFRC samples with 6% fiber reinforcement.

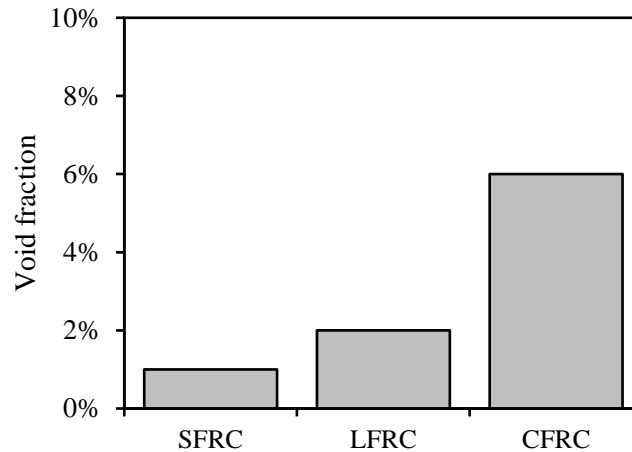


Figure 13. Void fraction within the printed fiber reinforced thermoplastic samples for short, long and continuous fiber reinforcement.

During LFRC printing processes, the decreased fiber bundle size made it easier for the PLA melt to flow into carbon fiber bundle and better wet single carbon fibers, thus yielding greatly reduced void fraction. In contrast, increasing the fiber bundle size and volume fraction would increase the tendency of tangled long fiber conglomerates, making it harder for the PLA melt to wet the fibers. Therefore, despite a potential increase in mechanical performance with an increase in fiber volume fraction, the presence of more voids could easily lead to fiber-matrix debonding and fiber pull-outs,

thus weakening the fiber reinforcing effects. It is expected that a prolonged impregnation time, e.g., decreasing print speed, would help decrease the void fraction, which will be investigated in the follow-up future studies.

### **3.4. DEMONSTRATION OF 3D PRINTED CARBON FIBER REINFORCED COMPOSITE STRUCTURES**

The applications of the proposed method in printing SFRC, LFRC and CFRC parts were demonstrated through the obtained structures shown in Figure 14. Based on the experimental setup discussed above, a print speed of 200 mm/min and a deposition rate of 13.3 g/min were used. The proposed AM method facilitated printing of composite samples of complex shapes reinforced with varying carbon fiber lengths. With high deposition rates, the proposed approach enabled fabrication of large-format samples within shorter amount of time compared to the traditional filament-based FDM processes. The wing-rib structure shown in Figure 14(A) was finished within two hours, attributed to the high deposition rates employed (13.3 g/min or 0.8 kg/hr), which normally would take days to print by filament-based FDM processes. Meanwhile, the average material costs was just around \$10/kg, much lower than the typical filament-based FDM processes, which can even increase the manufacturing costs of seemingly low-cost thermoplastics to \$100/kg [6]. It is also worth noting that due to the increased deposition rates, the LFRC parts were printed with a low print resolution and relatively high surface roughness compared to SFRC and CFRC parts; thus, requiring further post-processing, e.g., machining and polishing [54]–[56], for most large-scale printed parts. The successfully printed fiber reinforced parts demonstrated the feasibility of the proposed AM technique in fabrication of lightweight, structural components with high mechanical

strength and stiffness, potentially capable of replacing metal parts in the aerospace and automotive industries.

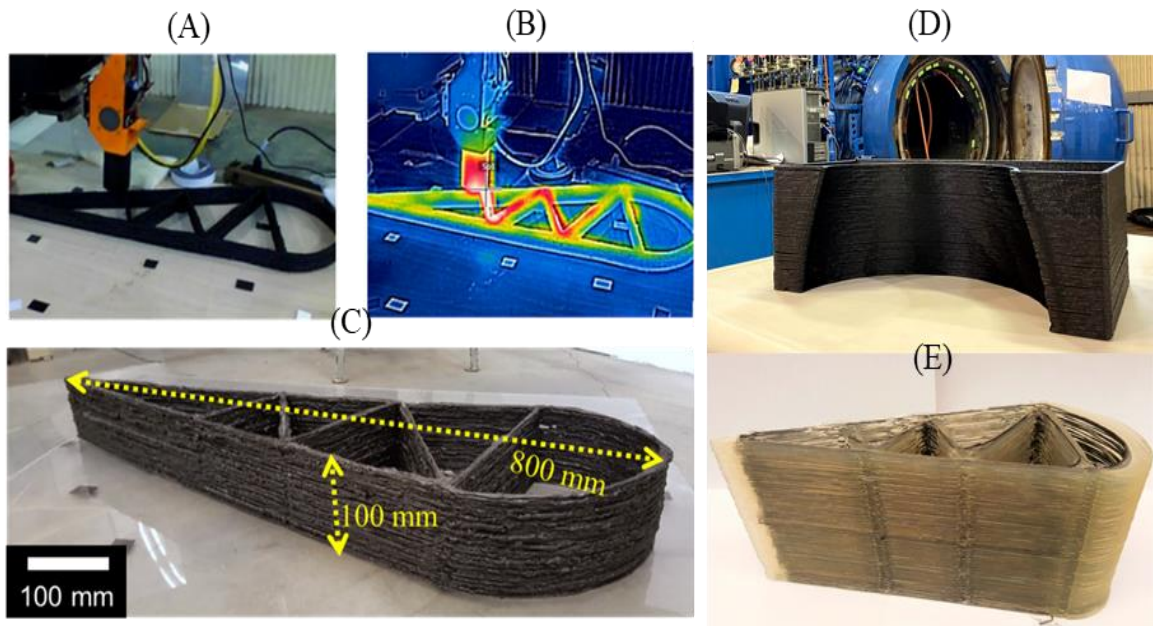


Figure 14. A large-scale (800 mm × 250 mm × 100 mm) wing rib structure printed at a deposition rate of 13.3 g/min and a print speed of 200 mm/min. (A) demonstrates the printing process, (B) shows the captured thermal image for the layer-by-layer deposition process, (C) shows the obtained LFRC part. (D) Shows a section of Cessna 414 nose-cone mold printed using SFRC, and (E) shows a wing rib structure printed with continuous carbon fiber reinforcement.

#### 4. CONCLUSION

In this study, a direct comparison was drawn between additively fabricated SFRC, LFRC and CFRC structures, using an LSAM method capable of directly printing short, long and continuous fiber reinforced composites, with minimal hardware modification. The method directly used continuous carbon fiber tows and thermoplastic pellets as feedstock materials for fabrication of LFRC and CFRC samples. The implementation of a

single-stage extruder helped achieve a high material deposition rate and thus was capable of printing large-scale components with high efficiency. The printed samples exhibited increment in mechanical properties with increase in reinforcing fiber length. LFRC samples demonstrated mechanical behavior close to the CFRC samples, with a 28% increase in average flexural strength and 50% increase in average flexural modulus over the pure thermoplastic counterparts. These were found to be attributed to highly oriented and relatively well distributed long fibers with an average length of 20.1 mm, much longer than the estimated fiber critical length for LFRC. However, a wide range of fiber length variation led to a large variation of flexural strength and modulus observed for the LFRC samples. With much lower void fraction, the void pattern in SFRC and LFRC samples were found to be dramatically different than that of the CFRC samples printed under the same conditions. Though SFRC exhibited lowest void fraction amongst fiber reinforced composites with similar fiber volume content, with further reduced fiber volume fraction, a much lower void fraction of 0.1% was achieved in the LFRC samples. The feasibility of the proposed AM method was further demonstrated through printing of large-scale complex SFRC, LFRC and CFRC structures at a high deposition rate of 0.8 kg/hr with a low material cost at \$10/kg. These results showed the potentials of the proposed method in additive manufacturing of large-scale, high-strength fiber-reinforced composites.

## ACKNOWLEDGEMENT

The authors acknowledge the funding support by the Intelligent Systems Center at the Missouri University of Science and Technology for the research work presented in this paper. The technical assistance of Charng-Yuh Lee in preparing samples during experiments is also much appreciated.

## REFERENCES

- [1] V. Srinivasa *et al.*, “Fracture morphology of carbon fiber reinforced plastic composite laminates,” *Mater. Res.*, vol. 13, no. 3, pp. 417–424, Sep. 2010.
- [2] H. Ning, N. Lu, A. A. Hassen, K. Chawla, M. Selim, and S. Pillay, “A review of Long fibre thermoplastic (LFT) composites,” *Int. Mater. Rev.*, vol. 65, no. 3, pp. 164–188, Apr. 2020.
- [3] T. Hartness, G. Husman, J. Koenig, and J. Dyksterhouse, “The characterization of low cost fiber reinforced thermoplastic composites produced by the DRIFT<sup>TM</sup> process,” *Compos. Part A Appl. Sci. Manuf.*, vol. 32, no. 8, pp. 1155–1160, Aug. 2001.
- [4] Y. Zhai, D. A. Lados, and J. L. LaGoy, “Additive Manufacturing: Making Imagination the Major Limitation,” *JOM*, vol. 66, no. 5, pp. 808–816, May 2014.
- [5] L. J. Love and C. Duty, “Cincinnati big area additive manufacturing (BAAM),” *Oak Ridge Natl. Lab.*, 2015.
- [6] L. J. Love *et al.*, “Breaking barriers in polymer additive manufacturing,” in *International SAMPE Technical Conference*, 2015.
- [7] V. Kunc *et al.*, “Low cost reactive polymers for large scale additive manufacturing,” in *CAMX 2018 - Composites and Advanced Materials Expo*, 2018.

- [8] D. Moreno Nieto, V. Casal López, and S. I. Molina, “Large-format polymeric pellet-based additive manufacturing for the naval industry,” *Addit. Manuf.*, vol. 23, pp. 79–85, Oct. 2018.
- [9] A. A. Hassen *et al.*, “The durability of large-scale additive manufacturing composite molds,” in *CAMX 2016 - Composites and Advanced Materials Expo*, 2016.
- [10] A. A. Hassen, J. Lindahl, X. Chen, B. Post, L. Love, and V. Kunc, “Additive manufacturing of composite tooling using high temperature thermoplastic materials,” in *International SAMPE Technical Conference*, 2016.
- [11] V. Kunc, V. Kishore, X. Chen, C. Ajinjeru, C. Duty, and A. A. Hassen, “High performance poly(etherketoneketone) (PEKK) composite parts fabricated using Big Area Additive Manufacturing (BAAM) processes,” Oak Ridge National Lab.(ORNL), Oak Ridge, TN (United States). Manufacturing ..., Oak Ridge, TN (United States), Sep. 2016.
- [12] S. Yang and W. Chin, “Mechanical properties of aligned long glass fiber reinforced polypropylene. II: Tensile creep behavior,” *Polym. Compos.*, vol. 20, no. 2, pp. 207–215, Apr. 1999.
- [13] K. K. Chawla, “Composite materials science and engineering,” *Composites*, vol. 20, no. 3, p. 286, May 1989.
- [14] T. Liu, X. Tian, Y. Zhang, Y. Cao, and D. Li, “High-pressure interfacial impregnation by micro-screw in-situ extrusion for 3D printed continuous carbon fiber reinforced nylon composites,” *Compos. Part A Appl. Sci. Manuf.*, vol. 130, p. 105770, Mar. 2020.
- [15] M. Luo, X. Tian, J. Shang, W. Zhu, D. Li, and Y. Qin, “Impregnation and interlayer bonding behaviours of 3D-printed continuous carbon-fiber-reinforced poly-ether-ether-ketone composites,” *Compos. Part A Appl. Sci. Manuf.*, vol. 121, pp. 130–138, Jun. 2019.
- [16] S. Toll and C.-G. Aronsson, “Notched strength of long- and short-fibre reinforced polyamide,” *Compos. Sci. Technol.*, vol. 45, no. 1, pp. 43–54, Jan. 1992.
- [17] T. Vu-Khanh and J. Denault, “Toughness of Reinforced Ductile Thermoplastics,” *J. Compos. Mater.*, vol. 26, no. 15, pp. 2262–2277, Dec. 1992.
- [18] H. Yasuda, Y. Chiba, and M. Ishikawa, “Effect of the glass fiber length on the mechanical properties of long glass fiber reinforced polyphenylene sulfide,” *J. Polym. Eng.*, vol. 31, no. 5, Sep. 2011.

- [19] F. Ning, W. Cong, Y. Hu, and H. Wang, “Additive manufacturing of carbon fiber-reinforced plastic composites using fused deposition modeling: Effects of process parameters on tensile properties,” *J. Compos. Mater.*, vol. 51, no. 4, pp. 451–462, Feb. 2017.
- [20] P. Dudek, “FDM 3D Printing Technology in Manufacturing Composite Elements,” *Arch. Metall. Mater.*, vol. 58, no. 4, pp. 1415–1418, Dec. 2013.
- [21] R. D. Farahani *et al.*, “Direct-write fabrication of freestanding nanocomposite strain sensors,” *Nanotechnology*, vol. 23, no. 8, p. 085502, Mar. 2012.
- [22] R. T. L. Ferreira, I. C. Amatte, T. A. Dutra, and D. Bürger, “Experimental characterization and micrography of 3D printed PLA and PLA reinforced with short carbon fibers,” *Compos. Part B Eng.*, vol. 124, pp. 88–100, Sep. 2017.
- [23] E. A. Papon and A. Haque, “Fracture toughness of additively manufactured carbon fiber reinforced composites,” *Addit. Manuf.*, vol. 26, pp. 41–52, Mar. 2019.
- [24] J. Justo, L. Távara, L. García-Guzmán, and F. París, “Characterization of 3D printed long fibre reinforced composites,” *Compos. Struct.*, vol. 185, pp. 537–548, Feb. 2018.
- [25] N. Li, Y. Li, and S. Liu, “Rapid prototyping of continuous carbon fiber reinforced polylactic acid composites by 3D printing,” *J. Mater. Process. Technol.*, vol. 238, pp. 218–225, Dec. 2016.
- [26] X. Yao, C. Luan, D. Zhang, L. Lan, and J. Fu, “Evaluation of carbon fiber-embedded 3D printed structures for strengthening and structural-health monitoring,” *Mater. Des.*, vol. 114, pp. 424–432, Jan. 2017.
- [27] X. Tian, T. Liu, C. Yang, Q. Wang, and D. Li, “Interface and performance of 3D printed continuous carbon fiber reinforced PLA composites,” *Compos. Part A Appl. Sci. Manuf.*, vol. 88, pp. 198–205, Sep. 2016.
- [28] R. Matsuzaki *et al.*, “Three-dimensional printing of continuous-fiber composites by in-nozzle impregnation,” *Sci. Rep.*, vol. 6, no. 1, p. 23058, Sep. 2016.
- [29] T. A. Dutra, R. T. L. Ferreira, H. B. Resende, and A. Guimarães, “Mechanical characterization and asymptotic homogenization of 3D-printed continuous carbon fiber-reinforced thermoplastic,” *J. Brazilian Soc. Mech. Sci. Eng.*, vol. 41, no. 3, p. 133, Mar. 2019.
- [30] H. Zhang, D. Liu, T. Huang, Q. Hu, and H. Lammer, “Three-Dimensional Printing of Continuous Flax Fiber-Reinforced Thermoplastic Composites by Five-Axis Machine,” *Materials (Basel)*, vol. 13, p. 1678, 2020.

- [31] W. Ye *et al.*, “Separated 3D printing of continuous carbon fiber reinforced thermoplastic polyimide,” *Compos. Part A Appl. Sci. Manuf.*, vol. 121, pp. 457–464, Jun. 2019.
- [32] J. Zhang, Z. Zhou, F. Zhang, Y. Tan, Y. Tu, and B. Yang, “Performance of 3D-Printed Continuous-Carbon-Fiber-Reinforced Plastics with Pressure,” *Materials (Basel)*, vol. 13, no. 2, p. 471, Jan. 2020.
- [33] N. Li, G. Link, and J. Jelonck, “3D microwave printing temperature control of continuous carbon fiber reinforced composites,” *Compos. Sci. Technol.*, vol. 187, p. 107939, Feb. 2020.
- [34] V. Yamakov, D. Wolf, S. R. Phillpot, and H. Gleiter, “Dislocation-dislocation and dislocation-twin reactions in nanocrystalline Al by molecular dynamics simulation,” *Acta Mater.*, vol. 51, no. 14, pp. 4135–4147, 2003.
- [35] NatureWorks, “Crystallizing and Drying of PLA,” *Technical Resources*, 2007. [Online]. Available: <http://www.natureworkslc.com/Technical-Resources/4-Series.aspx>. [Accessed: 13-Oct-2020].
- [36] H. Park, B. Kim, J. Gim, E. Han, and B. Rhee, “A study on the entrapped air bubble in the plasticizing process,” in *Annual Technical Conference - ANTEC, Conference Proceedings*, 2017.
- [37] E. Pérez-Pacheco, J. I. Cauich-Cupul, A. Valadez-González, and P. J. Herrera-Franco, “Effect of moisture absorption on the mechanical behavior of carbon fiber/epoxy matrix composites,” *J. Mater. Sci.*, vol. 48, no. 5, pp. 1873–1882, Mar. 2013.
- [38] Hexcel, “HexTow Continuous Carbon Fiber,” 2019. [Online]. Available: <https://www.hexcel.com/>. [Accessed: 13-Oct-2020].
- [39] X. Yan and S. Cao, “Structure and interfacial shear strength of polypropylene-glass fiber/carbon fiber hybrid composites fabricated by direct fiber feeding injection molding,” *Compos. Struct.*, vol. 185, pp. 362–372, Feb. 2018.
- [40] W. Zhong, F. Li, Z. Zhang, L. Song, and Z. Li, “Short fiber reinforced composites for fused deposition modeling,” *Mater. Sci. Eng. A*, vol. 301, no. 2, pp. 125–130, Mar. 2001.
- [41] H. L. Tekinalp *et al.*, “Highly oriented carbon fiber–polymer composites via additive manufacturing,” *Compos. Sci. Technol.*, vol. 105, pp. 144–150, Dec. 2014.
- [42] N. M. DeNardo, “Additive manufacturing of carbon fiber-reinforced thermoplastic composites,” Purdue University, 2016.

- [43] T. D. Papathanasiou and D. C. Guell, *Flow-Induced Alignment in Composite Materials*. Woodhead Publishing Limited, 1997.
- [44] K. B. Moses, S. G. Advani, and A. Reinhardt, “Investigation of fiber motion near solid boundaries in simple shear flow,” *Rheol. Acta*, vol. 40, no. 3, pp. 296–306, May 2001.
- [45] C. G. Joung, N. Phan-Thien, and X. J. Fan, “Direct simulation of flexible fibers,” *J. Nonnewton. Fluid Mech.*, vol. 99, no. 1, pp. 1–36, Apr. 2001.
- [46] W. P. Mason, *Physical Acoustics: Principles and Methods*, no. v. 1, pt. 1. Elsevier Science, 2013.
- [47] G. B. Jeffery, “The motion of ellipsoidal particles immersed in a viscous fluid,” *Proc. R. Soc. London. Ser. A, Contain. Pap. a Math. Phys. Character*, vol. 102, no. 715, pp. 161–179, Nov. 1922.
- [48] X. Tian, T. Liu, Q. Wang, A. Dilmurat, D. Li, and G. Ziegmann, “Recycling and remanufacturing of 3D printed continuous carbon fiber reinforced PLA composites,” *J. Clean. Prod.*, vol. 142, pp. 1609–1618, Jan. 2017.
- [49] C. E. Duty *et al.*, “Structure and mechanical behavior of Big Area Additive Manufacturing (BAAM) materials,” *Rapid Prototyp. J.*, vol. 23, no. 1, pp. 181–189, Jan. 2017.
- [50] Filabot, “Pulverized PLA - 4043D,” 2019. [Online]. Available: <https://www.filabot.com/blogs/news/filabot-pulverized-pla-4043d-for-your-next-project>. [Accessed: 13-Oct-2020].
- [51] K. Balaji Thattai parthasarathy, S. Pillay, H. Ning, and U. K. Vaidya, “Process simulation, design and manufacturing of a long fiber thermoplastic composite for mass transit application,” *Compos. Part A Appl. Sci. Manuf.*, vol. 39, no. 9, pp. 1512–1521, Sep. 2008.
- [52] Q. Wang, J. Jones, N. Lu, R. Johnson, H. Ning, and S. Pillay, “Development and characterization of high-performance kenaf fiber–HDPE composites,” *J. Reinf. Plast. Compos.*, vol. 37, no. 3, pp. 191–200, Feb. 2018.
- [53] D. McNally, “Short Fiber orientation and its Effects on the Properties of Thermoplastic Composite Materials,” *Polym. Plast. Technol. Eng.*, vol. 8, no. 2, pp. 101–154, Jan. 1977.
- [54] O. Lužanin, D. Movrin, and M. Plan, “Experimental Investigation of Extrusion Speed and Temperature Effects on Arithmetic Mean Surface Roughness in Fdm-,” *J. Technol. Plast.*, vol. 38, no. 2, 2013.

- [55] I. Gajdoš, E. Spišák, L. Kaščák, and V. Krasinskyi, “Surface Finish Techniques for FDM Parts,” *Mater. Sci. Forum*, vol. 818, pp. 45–48, May 2015.
- [56] R. Singh, S. Singh, I. P. Singh, F. Fabbrocino, and F. Fraternali, “Investigation for surface finish improvement of FDM parts by vapor smoothing process,” *Compos. Part B Eng.*, vol. 111, pp. 228–234, Feb. 2017.

### **III. ADDITIVE MANUFACTURING OF 3D STRUCTURAL BATTERY COMPOSITES WITH COEXTRUSION DEPOSITION OF CONTINUOUS CARBON FIBERS**

Aditya R. Thakur<sup>1</sup>, Xiangyang Dong<sup>1\*</sup>

<sup>1</sup> Department of Mechanical and Aerospace Engineering, Missouri University of Science and Technology, 400 W. 13th St., Rolla, MO 65409

\* Corresponding author

#### **ABSTRACT**

There is a growing interest in fabrication of structural battery composites to achieve mass-less energy storage. Additive manufacturing (AM) would allow customization of their battery form factor to fit specific needs. In this study, a multi-axis coextrusion deposition technique is proposed to fabricate a 3D structural battery composite with continuous carbon fibers coated by solid polymer electrolyte (SPE). The SPE-coated carbon fibers are coextruded with cathode doped matrix materials. All the printed complex structural battery composites successfully power up LEDs. Further mechanical and electrochemical characterization demonstrates the potentials of the additively manufactured composites in electrical energy storage and load bearing.

*Keywords: Additive manufacturing, Structural battery composites, Lithium ion battery, Continuous carbon fiber, Solid polymer electrolyte.*

## 1. INTRODUCTION

Growing needs of electric technologies in aviation, automotive, and consumer electronics require further development of high energy storage systems [1], [2]. One promising approach is to develop multifunctional composite structures and materials [3]–[5] to enable mass-less energy storage for electrically powered structural systems [6] in order to achieve improvement of energy and power densities at a system level. In particular, structural power composites are capable of simultaneously carrying mechanical loads and storing electrical energy, and thus have been extensively investigated [4], [6]–[10]. Among them, carbon fiber composites, commonly used as structural materials, show great potentials of being used as structural power composites due to preferable electrochemical properties of carbon fibers [11]–[13]. A majority of multifunctional carbon fiber composites are based on a laminated composite structure and are fabricated through conventional lay-up processes [3], [7], which involve high fabrication costs and long development cycles for components with complex geometries.

On the other hand, additive manufacturing (AM) methods allow flexible design of shape and size, which would further allow a battery form factor to be customized for improvement of energy storage or to fit a given product design [14]–[16]. In particular, AM techniques have been recently developed to fabricate carbon fiber reinforced thermoplastics based on extrusion deposition process [17]–[20]. However, their applications in multifunctional composites are limited [21]–[24]. Most of studies focused on optimization of their mechanical performance [25], [26]. Thus, it will be necessary to

develop AM techniques to explore applications of carbon fiber composites in structural power composites.

In this study, a multi-axis coextrusion deposition method is proposed to additively manufacture a 3D structural battery composite structure with continuous carbon fibers. Electrocoating is first used to produce solid polymer electrolyte (SPE) onto each individual carbon fiber. Polylactic acid (PLA), a commonly used thermoplastic material for 3D printing, is infused with active and conductive materials to prepare cathode doped matrix materials that are further used to fabricate the structural battery composites with various geometries. It is worth noting that as previous studies [24] suggested the doped cathode materials would hinder the curing process of photopolymer binders, we propose a new 3D printing process using thermoplastics as feedstock in order to increase loadings of cathode materials. Both electrochemical and mechanical properties are characterized to demonstrate the potentials of the proposed AM method.

## **2. EXPERIMENTAL PROCEDURE**

### **2.1. 3D STRUCTURAL BATTERY ARCHITECTURE**

A concentric 3D structural battery composite architecture in Figure 1A was implemented in this study. Carbon fiber works as both anode and current collector. A solid polymer electrolyte individually coated on each carbon fiber is used as electrolyte and separator. SPE-coated carbon fibers are embedded in cathode doped matrix materials that are further assembled with current collector. Dispersed in cathode doped matrix, individually SPE-coated carbon fibers formed a network of micro-battery cells. Due to

high surface area between coated fibers and active materials, the obtained structural batteries have potentials of achieving high energy density [4], [27].

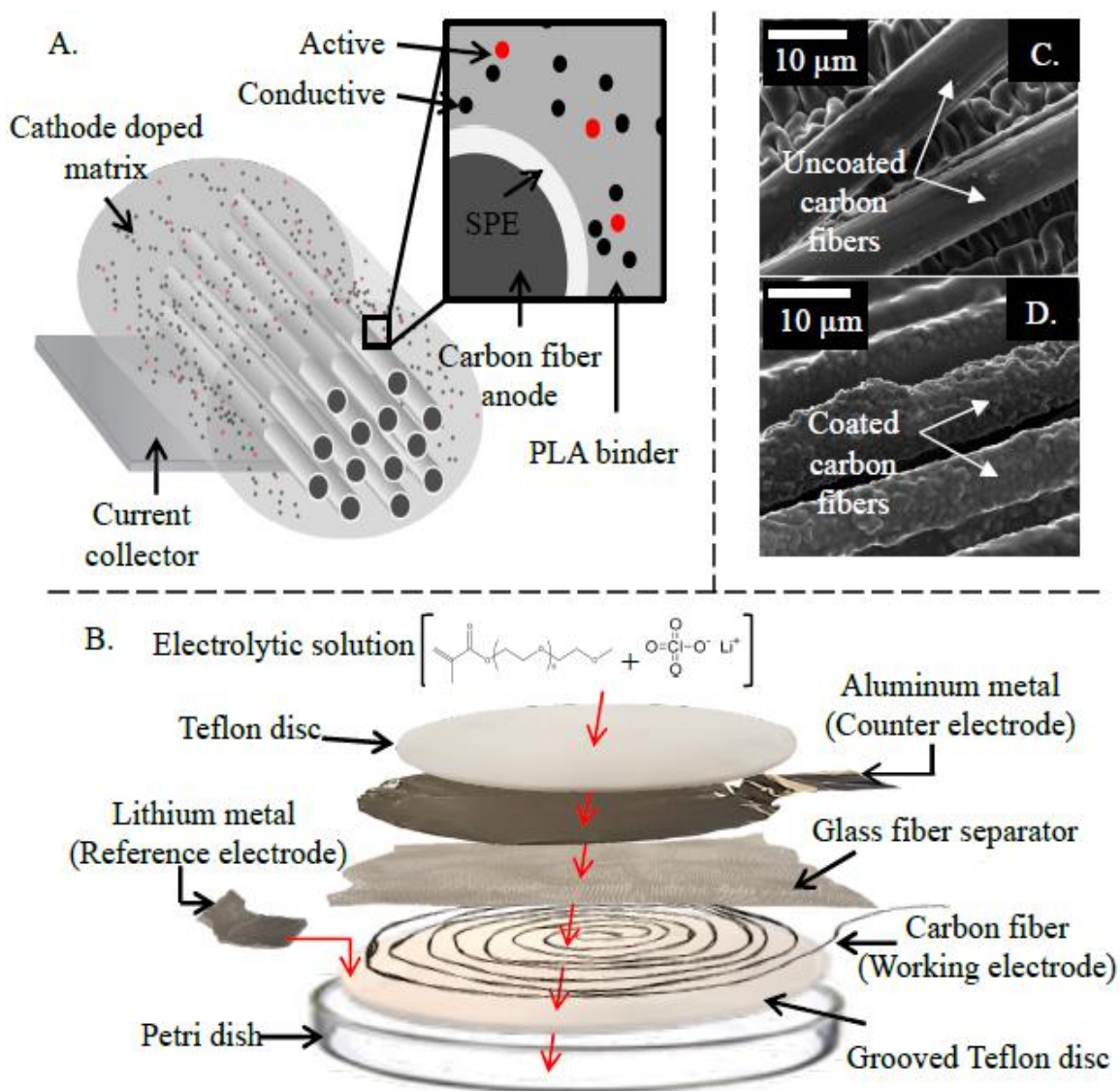


Figure 1. Schematics of the 3D structural battery composite architecture: (A) shows the 3D structural battery design; (B) shows the electrocoating process to produce solid polymer electrolyte onto continuous carbon fiber; (C) and (D) show a direct comparison of uncoated and SPE-coated carbon fibers.

SPE coatings [28] were prepared using a three-electrode electrocoating assembly in Figure 1B inside a glove box in an Argon atmosphere (<1 ppm oxygen content and moisture). A carbon fiber tow in Figure 1C with a total length of up to 300 mm could be electrocoated (Figure 1D) to facilitate 3D printing of various structural battery composites samples. It should be noted that although longer coated carbon fiber length is possibly achieved, correspondingly increased heat generation and thermal induced stress during electrochemical cycling may lead to mechanical and electrical failure [29]. In this study, Polyacrylonitrile (PAN)-based carbon fibers (Toray T800HB, 12000 filaments per rowing) were selected (dried in a vacuum oven at 120 °C for at least four hours to remove moisture) to facilitate printing process for the structural battery composites, together with their favorable electrochemical and mechanical properties [13], [30]. It is worth noting that the fiber bundle size may also affect structural battery performance. The solution with 1M LiClO<sub>4</sub> (less sensitive to the atmospheric moisture [27]) in methoxy polyethylene glycol (350) monomethacrylate (SR550) monomer was dissolved in Dimethylformamide (DMF by Sigma-Aldrich) with a monomer-to-solvent ratio of 1:2 (by volume) and used in the electrocoating process. The SPE coating was polymerized from the solution, leaving grafted polymer on each individual carbon fiber. A SPE coating of about 2 μm thickness in Figure 1D was obtained with a polarization time of 400 s. The SPE coating thickness was estimated via the scanning electron microscope (SEM) images of the uncoated and coated fibers, by characterizing their cross sections using the FIJI image analyses package.

The cathode doped matrix materials need to have a high electrical conductivity and a high ionic conductivity. Commercial graphene infused PLA pellets (by

Blackmagic3D) with an electrical resistivity of  $1 \Omega \cdot \text{cm}$  were used, where graphene worked as conductive materials, and PLA would serve as binder material to facilitate the proposed AM method. Lithium iron phosphate (by Sigma-Aldrich), commonly used for electrodes of lithium ion batteries, was selected as active material for its high theoretical specific capacity. The pelletized cathode doped matrix materials were then prepared following through dissolving, curing, and drying. While PLA is a commonly used 3D printing material, a major challenge in the structural battery composites is its very poor ionic conductivity. It was thus converted into an ionically conductive matrix through post cure swelling of printed samples by infusion with liquid electrolytes. A 1:1 (by volume) solution of ethyl methyl carbonate (EMC) and propylene carbonate (PC) with 1 M  $\text{LiClO}_4$  was used since it was shown to promote stable ionic conductivity and retain mechanical integrity of infused polymers over a long period of time [31]. In this study, all printed samples were infused at  $50^\circ\text{C}$  for 24 h and aged for another 24 h prior to testing.

## **2.2. EXPERIMENTAL SETUP**

To fabricate the proposed 3D structural battery architecture, a coextrusion deposition method in Figure 2A was proposed to additively manufacture the 3D structural battery composite materials. It included a single-screw extruder with its movement controlled by a multi-axis machine, thus allowing drawing toolpath in three-dimensional space. The extruder rotation speed was used to control the material deposition rate during printing process. The cathode doped PLA pellets were fed through the extruder hopper and melted by the heater before being extruded out through the coextrusion nozzle (4 mm inner diameter). Meanwhile, a continuous SPE-coated carbon fiber bundle was

impregnated through the extrusion nozzle [20] and coextruded with the cathode doped PLA melt before being deposited on the print bed layer-by-layer, in an ambient air pressure and temperature. It should be noted that drawing forces during the proposed printing process tend to place the SPE-coated carbon fibers near the top region of each deposition layer in Figure 2B. This would hinder the fiber impregnation into the cathode doped matrix materials. The resulting voids and fiber clumping would severely limit the electrochemical performance of the printed battery samples. Moreover, the coextrusion nozzle may scratch away the SPE coatings. Any exposed carbon fiber would be in direct contact with the cathode matrix materials and cause short circuiting of the printed structural battery cells. Thus, a 5-axis printing process (with the extruder in Figure 2 mounted on a 5-axis machine) was implemented. The rotational A axis and B axis were adjusted to maintain a constant tilt angle (Figure 2C) between extruder and deposition bead following the printing toolpath. In this study, a tilt angle of  $15^\circ$  was used with a melting temperature of  $175^\circ\text{C}$ , a print speed of  $40\text{ mm/min}$ , and a layer thickness of  $2.5\text{ mm}$ . A preheated temperature of  $45^\circ\text{C}$  on the print bed was also used to facilitate deposition process. With an extruder rotation speed of  $22\text{ RPM}$ , a material output rate of  $280\text{ mm}^3/\text{min}$  was achieved with a typical deposited sample shown in Figure 2D. It is worth noting further optimization of these printing parameters may help improve the performance of printed structural battery composites, the effects of which will be investigated in future studies.

### 3. RESULTS AND DISCUSSION

To maximize energy capacities, the ratio of active material to conductive material was first optimized to achieve highest ionic conductivity in Figure 3A. Electrochemical Impedance Spectroscopy (EIS) measurements were performed using a Gamry Reference 600+ potentiostat over a frequency range of 1 MHz to 10 Hz at 100 mV pp. Electrical resistivity measurement was made using a Signatone Pro4-4000 Four Point Resistivity System with a Keithley 2400 Sourcemeter. At a fixed percentage of PLA binder, an active material to conductive material ratio of 20:80 yielded a highest ionic conductivity of 1.2 mS/cm.

The need to use a relatively high amount of conductive materials was presence of high volume of PLA binder, which hindered the electrical contact between active and conductive materials [31]. A corresponding electrical resistivity of 4  $\Omega \cdot \text{cm}$  was measured for the cathode doped PLA matrix materials, much higher than the as-received graphene/PLA pellets. This was possibly attributed to the addition of active material as well as additional post processing. This was possibly attributed to the addition of active material as well as additional post processing in preparing cathode doped pellets.

The electrochemical performance was characterized through specific capacity measured by a Gamry Reference 600+ potentiostat. The electrochemical performance for full battery cells 10 was performed within a cutoff voltage range 6.0–1.0 V. The capacity was normalized to the mass of anode active material (i.e. carbon fiber). Figure 3B shows the charging-discharging capacities of rectangular structural battery samples (80 mm  $\times$  10 mm  $\times$  5 mm) for 10 consecutive cycles with a current density of 10 mA/cm<sup>3</sup> at C/2.

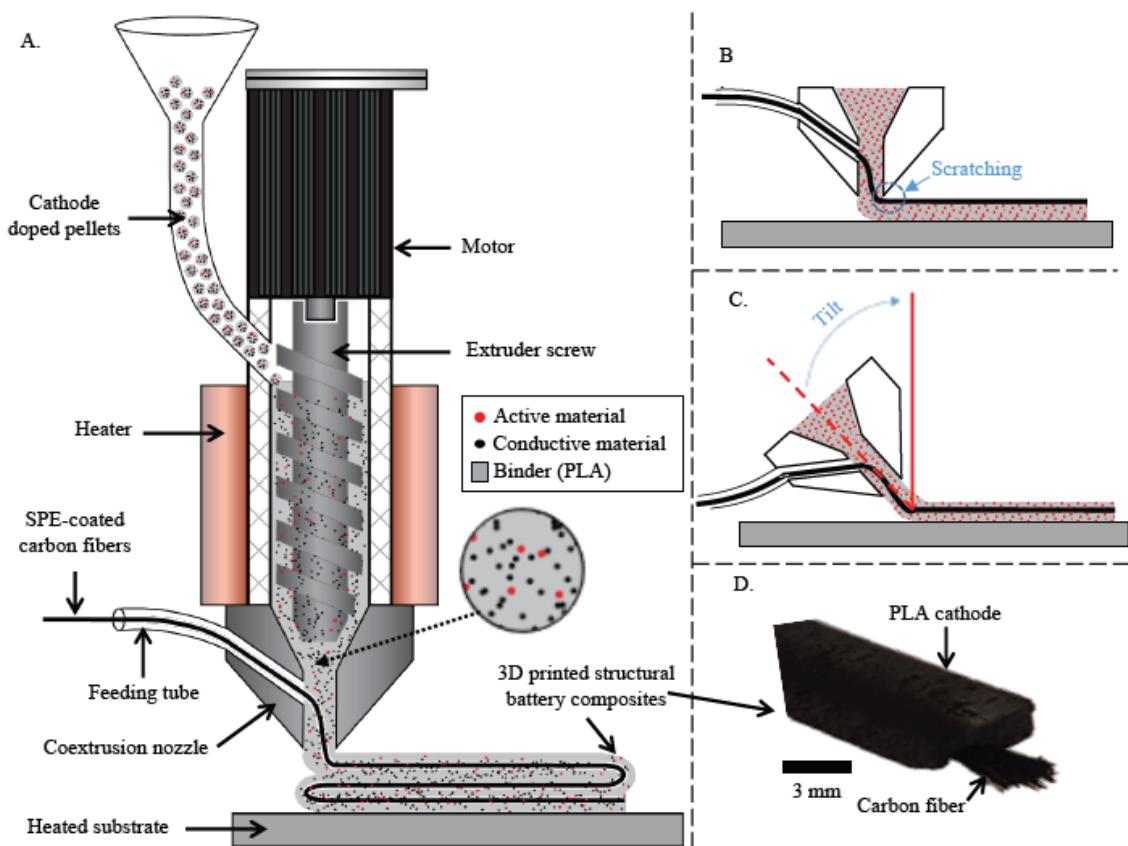


Figure 2. Schematics of the proposed AM method to print structural battery composites with SPE-coated continuous carbon fibers: (A) shows the experimental setup, where the extruder is mounted on a 5-axis machine; (B) and (C) demonstrate the implemented multi-axis printing process; (D) shows a typical printed structural battery composite sample.

The specific capacity of graphite (372 mAh/g) was used to calculate the C-rate. An obvious drop in charging capacity was observed, decreasing from 119.9 mAh/g to 25.5 mAh/g after 10 cycles when it tended to stabilize. The large irreversible capacity loss was attributed to the formation of solid electrolyte interphase [31]–[33] and trapped lithium in the carbon fiber structure [34]. The discharging capacity of the battery cell was also notably higher than that of a single print PLA battery by fused filament fabrication [31].

It is worth noting that this was mainly attributed to higher loadings of conductive and active materials in the cathode doped matrix materials as enabled by the proposed AM method. Pellet-based extrusion processes typically exhibit better printability for given compositions, which would otherwise lead to clogging or brittle filaments that become too brittle to handle based on filament fusion fabrication.

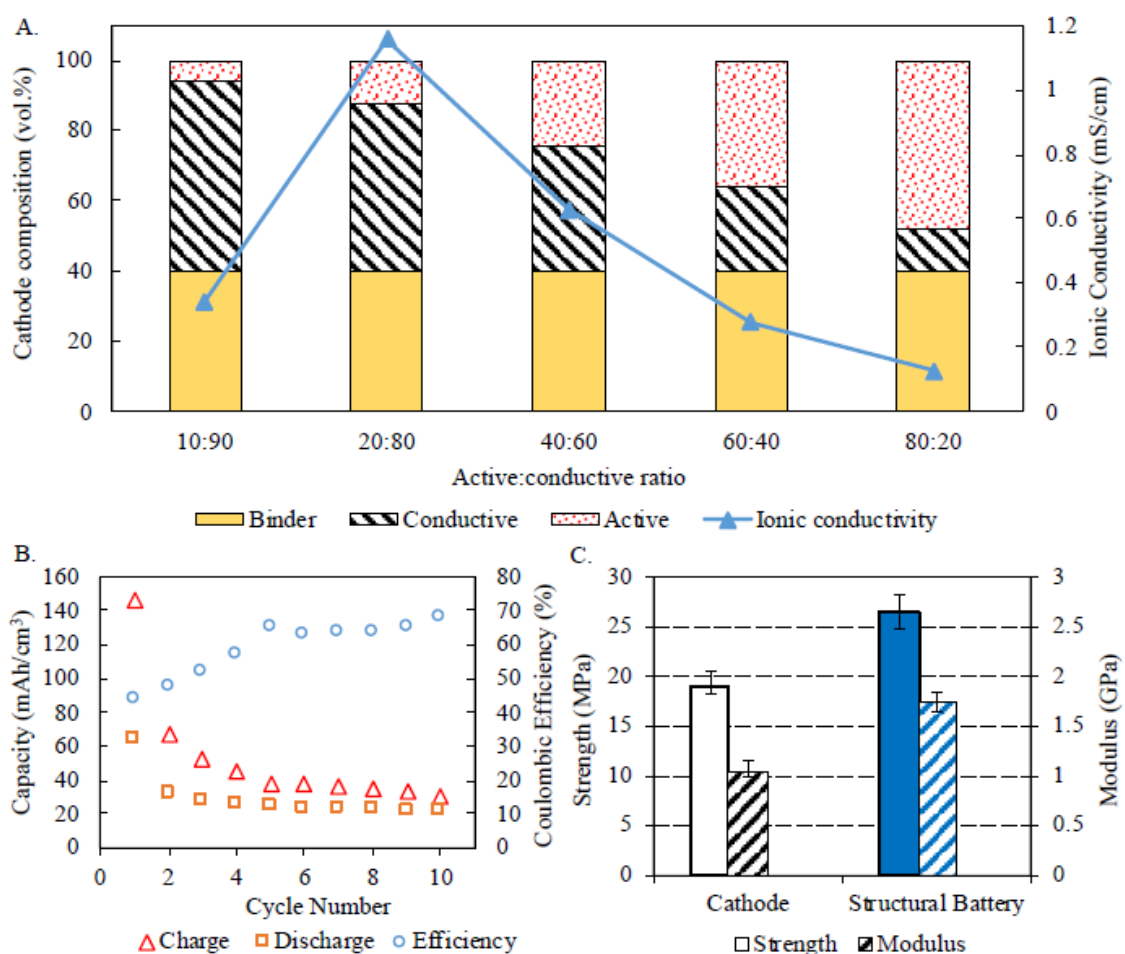


Figure 3. Characterization of the printed samples: (A) shows optimization of cathode doped matrix materials; (B) shows capacity and Coulombic efficiency of the printed structural battery at a current density of 10 mA/cm<sup>3</sup> at C/2 for 10 cycles; (C) shows flexural strength and modulus measured through 4-point bending tests in comparison of printed cathode matrix and structural battery composite samples (80 mm × 10 mm × 5 mm).

Meanwhile, the improvement was expected to be related to the introduced SPE-coated carbon fibers, which showed high electrochemical performance [28] and would also promote the mechanical performance of the printed structural battery composite samples. On the other hand, for the 10 consecutive cycles, the battery cell yielded an average charging capacity of 42.9 mAh/g and discharging capacity of 23.4 mAh/g, showing an average Coulombic efficiency of nearly 68% after the 10 cycles. The energy density was 7.6 Wh/kg with an average battery cell voltage of 1.8 V calculated over the discharge cycle [31]. These values are substantially lower than energy densities of typical lithium-ion full battery cells [28]. The low values were attributed to the relative thick SPE coatings as well as high percentage of PLA binder used to maintain good printability of the cathode matrix materials, which limited the contact between active and conductive materials.

The mechanical properties of both cathode doped matrix and structural battery composite samples were measured using 4-point bending tests with a support span of 40 mm and a load span of 20 mm at a cross-head speed of 1 mm/min. Three samples of each composition were used to measure the mechanical properties in Figure 3C with the error bars showing the variations in the measured strength and modulus. The transverse modulus of the composite samples was measured in this study. With the introduction of 15 vol.% continuous fiber reinforcements, 39% in flexural strength and 66% in flexural modulus were achieved compared to those of cathode doped matrix materials. These well demonstrated the potentials of the printed carbon fiber structural batteries in load bearings while working as batteries to store electrical energy. Meanwhile, the mechanical properties were lower than conventional carbon fiber composites, which are believed to

be related to the proposed AM process. The doped cathode materials are expected to increase the viscosity of PLA matrix materials, thus lowering fiber impregnation quality and possibly leading to a higher void fraction, which will be examined in follow-up studies.

The capability of the proposed AM method was further demonstrated through printing structural battery composite samples of various geometries in Figure 4. As the AM method was able to fabricate a full structural battery cell in one print, the obtained samples just needed to be assembled with aluminum current collector before being charged to power up LEDs.

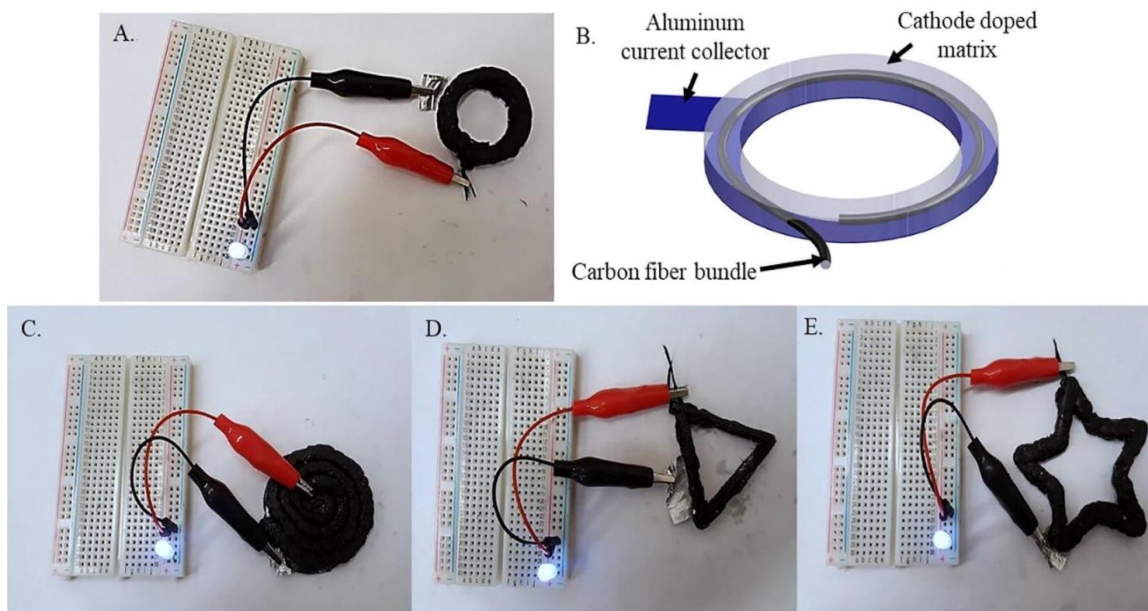


Figure 4. Printed structural battery composites illuminating LEDs with a ring-shaped structure shown in (A) and the schematics of its full battery assembly shown in (B). A similar full battery assembly process has been used for a disc-shaped structure in (C), a triangle structure in (D), and a star-shaped structure in (E).

#### **4. CONCLUSION**

A coextrusion deposition method was proposed to additively manufacture a 3D structural battery composite with continuous carbon fibers. Cathode doped matrix materials were coextruded with solid polymer electrolyte coated carbon fibers. The structural battery cells fabricated in single print were shown to successfully power up LEDs. The implemented pellet-based extrusion enabled high loadings of active and conductive materials and promoted the obtained electrochemical performance. The introduced SPE-coated carbon fibers not only enabled electrical energy storage but also promoted the mechanical performance of the printed structural battery composites. With individually SPE-coated carbon fibers dispersed in cathode matrix working as micro-battery cells, further improvement of the proposed AM method will help explore their potentials of achieving high energy density.

#### **ACKNOWLEDGEMENT**

The authors acknowledge the supports from the Ralph E. Power Junior Faculty Enhancement Award from Oak Ridge Associated Universities, and the Intelligent Systems Center at Missouri University of Science and Technology. The technical assistance of Chang-Yuh Lee in preparing samples during experiments is also much appreciated.

## REFERENCES

- [1] B. Fleming, “An Overview of Advances in Automotive Electronics [Automotive Electronics],” *IEEE Veh. Technol. Mag.*, vol. 9, no. 1, pp. 4–9, Mar. 2014.
- [2] J. P. Thomas and M. A. Qidwai, “The design and application of multifunctional structure-battery materials systems,” *JOM*, vol. 57, no. 3, pp. 18–24, Mar. 2005.
- [3] E. Senokos *et al.*, “Energy storage in structural composites by introducing CNT fiber/polymer electrolyte interleaves,” *Sci. Rep.*, vol. 8, no. 1, p. 3407, Dec. 2018.
- [4] L. E. Asp and E. S. Greenhalgh, “Structural power composites,” *Compos. Sci. Technol.*, vol. 101, pp. 41–61, Sep. 2014.
- [5] P. Ladpli, R. Nardari, F. Kopsaftopoulos, and F.-K. Chang, “Multifunctional energy storage composite structures with embedded lithium-ion batteries,” *J. Power Sources*, vol. 414, pp. 517–529, Feb. 2019.
- [6] L. E. Asp, M. Johansson, G. Lindbergh, J. Xu, and D. Zenkert, “Structural battery composites: a review,” *Funct. Compos. Struct.*, vol. 1, no. 4, pp. 1–19, 2019.
- [7] W. Johannisson *et al.*, “Multifunctional performance of a carbon fiber UD lamina electrode for structural batteries,” *Compos. Sci. Technol.*, vol. 168, pp. 81–87, Nov. 2018.
- [8] A. Lendlein and R. S. Trask, “Multifunctional materials: concepts, function-structure relationships, knowledge-based design, translational materials research,” *Multifunct. Mater.*, vol. 1, no. 1, p. 010201, Aug. 2018.
- [9] P. Liu, E. Sherman, and A. Jacobsen, “Design and fabrication of multifunctional structural batteries,” *J. Power Sources*, vol. 189, no. 1, pp. 646–650, 2009.
- [10] Y. Yu *et al.*, “Multifunctional structural lithium ion batteries based on carbon fiber reinforced plastic composites,” *Compos. Sci. Technol.*, vol. 147, pp. 62–70, 2017.
- [11] G. Fredi *et al.*, “Graphitic microstructure and performance of carbon fibre Li-ion structural battery electrodes,” *Multifunct. Mater.*, vol. 1, no. 1, pp. 1–6, 2018.
- [12] E. Jacques, M. H. Kjell, D. Zenkert, and G. Lindbergh, “The effect of lithium-intercalation on the mechanical properties of carbon fibres,” *Carbon N. Y.*, vol. 68, pp. 725–733, Mar. 2014.

- [13] M. H. Kjell, E. Jacques, D. Zenkert, M. Behm, and G. Lindbergh, "PAN-Based Carbon Fiber Negative Electrodes for Structural Lithium-Ion Batteries," *J. Electrochem. Soc.*, vol. 158, no. 12, p. A1455, 2011.
- [14] N. Shirshova *et al.*, "Structural composite supercapacitors," *Compos. Part A Appl. Sci. Manuf.*, vol. 46, pp. 96–107, Mar. 2013.
- [15] T. S. Arthur *et al.*, "Three-dimensional electrodes and battery architectures," *MRS Bull.*, vol. 36, no. 7, pp. 523–531, Jul. 2011.
- [16] M. Cheng, R. Deivanayagam, and R. Shahbazian-Yassar, "3D Printing of Electrochemical Energy Storage Devices: A Review of Printing Techniques and Electrode/Electrolyte Architectures," *Batter. Supercaps*, vol. 3, no. 2, pp. 130–146, Feb. 2020.
- [17] N. Li, Y. Li, and S. Liu, "Rapid prototyping of continuous carbon fiber reinforced polylactic acid composites by 3D printing," *J. Mater. Process. Technol.*, vol. 238, pp. 218–225, Dec. 2016.
- [18] X. Yao, C. Luan, D. Zhang, L. Lan, and J. Fu, "Evaluation of carbon fiber-embedded 3D printed structures for strengthening and structural-health monitoring," *Mater. Des.*, vol. 114, pp. 424–432, Jan. 2017.
- [19] X. Tian, T. Liu, C. Yang, Q. Wang, and D. Li, "Interface and performance of 3D printed continuous carbon fiber reinforced PLA composites," *Compos. Part A Appl. Sci. Manuf.*, vol. 88, pp. 198–205, Sep. 2016.
- [20] R. Matsuzaki *et al.*, "Three-dimensional printing of continuous-fiber composites by in-nozzle impregnation," *Sci. Rep.*, vol. 6, p. 23058, 2016.
- [21] M. Zhang *et al.*, "Printable Smart Pattern for Multifunctional Energy-Management E-Textile," *Matter*, vol. 1, no. 1, pp. 168–179, Jul. 2019.
- [22] J. Peng *et al.*, "3D extruded composite thermoelectric threads for flexible energy harvesting," *Nat. Commun.*, vol. 10, no. 1, p. 5590, Dec. 2019.
- [23] A. Lund, K. Rundqvist, E. Nilsson, L. Yu, B. Hagström, and C. Müller, "Energy harvesting textiles for a rainy day: woven piezoelectrics based on melt-spun PVDF microfibrils with a conducting core," *npj Flex. Electron.*, vol. 2, no. 1, p. 9, Dec. 2018.
- [24] A. Thakur and X. Dong, "Printing with 3D continuous carbon fiber multifunctional composites via UV-assisted coextrusion deposition," *Manuf. Lett.*, vol. 24, pp. 1–5, Apr. 2020.

- [25] J. P. Lewicki *et al.*, “3D-Printing of Meso-structurally Ordered Carbon Fiber/Polymer Composites with Unprecedented Orthotropic Physical Properties,” *Sci. Rep.*, vol. 7, p. 43401, Mar. 2017.
- [26] B. Brenken, E. Barocio, A. Favaloro, V. Kunc, and R. B. Pipes, “Fused filament fabrication of fiber-reinforced polymers: A review,” *Addit. Manuf.*, vol. 21, no. October 2017, pp. 1–16, May 2018.
- [27] Q. Chen, R. Xu, Z. He, K. Zhao, and L. Pan, “Printing 3D Gel Polymer Electrolyte in Lithium-Ion Microbattery Using Stereolithography,” *J. Electrochem. Soc.*, vol. 164, no. 9, pp. A1852–A1857, 2017.
- [28] S. Leijonmarck, T. Carlson, G. Lindbergh, L. E. Asp, H. Maples, and A. Bismarck, “Solid polymer electrolyte-coated carbon fibres for structural and novel micro batteries,” *Compos. Sci. Technol.*, vol. 89, pp. 149–157, Dec. 2013.
- [29] D. Carlstedt and L. E. Asp, “Thermal and diffusion induced stresses in a structural battery under galvanostatic cycling,” *Compos. Sci. Technol.*, 2019.
- [30] M. H. Kjell, T. G. Zavalis, M. Behm, and G. Lindbergh, “Electrochemical characterization of lithium intercalation processes of PAN-based carbon fibers in a microelectrode system,” *J. Electrochem. Soc.*, vol. 160, no. 9, pp. 1473–1481, 2013.
- [31] C. Reyes *et al.*, “Three-Dimensional Printing of a Complete Lithium Ion Battery with Fused Filament Fabrication,” *ACS Appl. Energy Mater.*, vol. 1, no. 10, p. acsaem.8b00885, Oct. 2018.
- [32] J. Vetter *et al.*, “Ageing mechanisms in lithium-ion batteries,” *J. Power Sources*, vol. 147, no. 1–2, pp. 269–281, Sep. 2005.
- [33] M. Park, X. Zhang, M. Chung, G. B. Less, and A. M. Sastry, “A review of conduction phenomena in Li-ion batteries,” *J. Power Sources*, vol. 195, no. 24, pp. 7904–7929, 2010.

#### **IV. PRINTING WITH 3D CONTINUOUS CARBON FIBER MULTIFUNCTIONAL COMPOSITES VIA UV-ASSISTED COEXTRUSION DEPOSITION**

Aditya Thakur <sup>1</sup> and Xiangyang Dong <sup>1\*</sup>

<sup>1</sup> Mechanical and Aerospace Engineering, Missouri University of Science and  
Technology, Rolla, MO 65409

\* Corresponding author

#### **ABSTRACT**

This study proposes to print multifunctional composite materials with 3D continuous carbon fibers. Coextrusion was implemented to deposit continuous carbon fibers simultaneously with doped functional photopolymer resin, subsequently rapidly cured by an ultraviolet laser. The technique allowed for direct printing of free-standing compliant carbon fiber reinforced composite structures and composites with conductive channeling. In particular, a novel functional, full lithium-ion structural battery was successfully printed in one single step with each coated carbon fiber acting as a micro-battery cell. The characterized mechanical and electrochemical performance well demonstrated the potentials of the proposed method in direct printing multifunctional structural composites.

*Keywords: Multifunctional composites; additive manufacturing; coextrusion; structural battery; continuous carbon fiber*

## 1. INTRODUCTION

The rapidly increasing demand in mobile electric technologies has necessitated the need to develop energy storage systems with high volumetric efficiency. Compared to the traditional approach in minimizing the weight of energy storage systems [1], an alternative approach involves the development of multifunctional composite structures [2], [3] and materials [4]. Carbon fibers show capabilities of simultaneously carrying mechanical loads, storing and even harvesting energy [5], and thus offer significant reduction in system-level weight and volume. In particular, a 3D continuous single carbon fiber structural design was shown with great potentials in energy storage [6], where each individual carbon fiber, directly acting as one battery electrode, was coated with solid polymer electrolyte (SPE). Compared to the laminated battery structure [4], [7] and a heavy tow carbon fiber electrode [8], the single carbon fiber was found to show better reversible capacities and higher charging rates [9] due to increased intercalation surface area. However, this design also posed great challenges in fabrication techniques. Most of the multifunctional carbon fiber reinforced composites (CFRC) are based on a laminated battery structure and are fabricated through the conventional lay-up processes [3], [10]. The high fabrication costs and cycles hindered the implementation of multifunctional materials and structures.

CFRC has recently gained much attention for their potential use in additive manufacturing (AM) to enhance the mechanical strength of manufactured parts with reduced warpage and improved dimensional stability [11]–[15]. There is also an increasing interest to explore the multifunctional CFRC via AM. However, the existing

AM techniques for CFRC were mainly optimized for mechanical performance. Most of the printed CFRC parts were reinforced with short carbon fibers that are not capable of energy storage [14], [16]. Thus, it is necessary to develop a new 3D printing technique for multifunctional CFRC with continuous carbon fibers. Early studies demonstrated extrusion deposited continuous CFRC via in-nozzle impregnation [17]–[19]. However, the state-of-the-art work mostly utilized thermoplastics [14], [20], [21], which often gave rise to voids between adjacent beads [22], [23], limiting the electrical performance of the printed parts. In this study, a new printing method based on coextrusion deposition of liquid photopolymers with fiber impregnation is presented. The continuous carbon fibers are simultaneously extruded and rapidly cured by an ultraviolet (UV) laser. The objective of this study is to investigate the feasibility of this method in direct printing of multifunctional CFRC, particularly functional structural parts with both uncoated and coated continuous carbon fibers. A novel functional full structural lithium-ion battery structure was successfully printed with continuous carbon fibers.

## 2. EXPERIMENTAL SETUP

The schematics of the proposed AM method is shown in Figure 1(A). A coextrusion head, with an inner nozzle diameter of 0.6 mm and an outer nozzle diameter of 1.2 mm, was connected to two dispensers. The inner nozzle was connected to the vertical dispenser, where a tow of continuous carbon fibers, uncoated or with uniformly coated SPE [24], [25] for structural battery, was embedded in the uncured doped photopolymer (as cathode) before deposition. The outer nozzle was connected to the

horizontal dispenser holding the undoped photopolymer (as insulation). With the pressurized air applied, the continuous carbon fibers were first coextruded with the doped photopolymer through inner nozzle and then further impregnated into the undoped photopolymer within the coextrusion head [17]–[19] before deposited on the substrate layer-by-layer. An ultraviolet (UV) laser (200 mW, 405 nm) was mounted together with the coextrusion head capable of drawing in three-dimensional space. The UV laser beam was always aimed at a focus spot behind the coextrusion head with a constant distance of 10 mm to facilitate rapid curing of the coextruded materials while avoid clogging the coextrusion head. The relative position between the laser spot and the coextrusion head was maintained by a rotation table, where the substrate was mounted, while the coextrusion head followed the toolpath in different moving directions during printing process, as demonstrated by directly printed free-standing spring and cylinder structures reinforced with continuous carbon fibers in Figure 1(B), (C), and (D).

Commercial photopolymer resin (UV wavelength 405 nm) by Elegoo [26] was used as matrix materials. Polyacrylonitrile (PAN)-based carbon fibers (Toray T800HB 12K Carbon Fiber tow) were selected due to the favorable lithium-ion intercalation capabilities and mechanical strength [8]. The printability and coextrusion of continuous carbon fibers were controlled by the viscosity of the photopolymer resin, where the carbon fibers were fed by the drag force between the resin and carbon fibers. For viscous fluids at low velocities, the drag force is given as  $F_d = a\eta v$ , where  $F_d$  is the drag force,  $a$  is the size of the carbon fiber size,  $\eta$  is the coefficient representing viscosity, and  $v$  is the velocity of the carbon fibers with respect to the resin [1]. At the selected carbon fiber size and a flow rate of 18 mm<sup>3</sup>/s in this study, the drag force will be linearly related to the

resin viscosity. The resin viscosity will be affected by additives, e.g., doped conductive and active materials. Colloidal silica thickener by West System was also used in this study to accurately control the viscosity, following through dissolving and defoaming procedures before the solution was transferred to the dispensers. Preliminary studies were performed with a systematic increase of silica thickener, indicating no noticeable sagging or dragging observed while feeding the selected 12K continuous carbon fibers starting at 5 wt.%. A good deposition resolution and structural integrity were observed within the printed samples thickened at 7 wt.% silica.

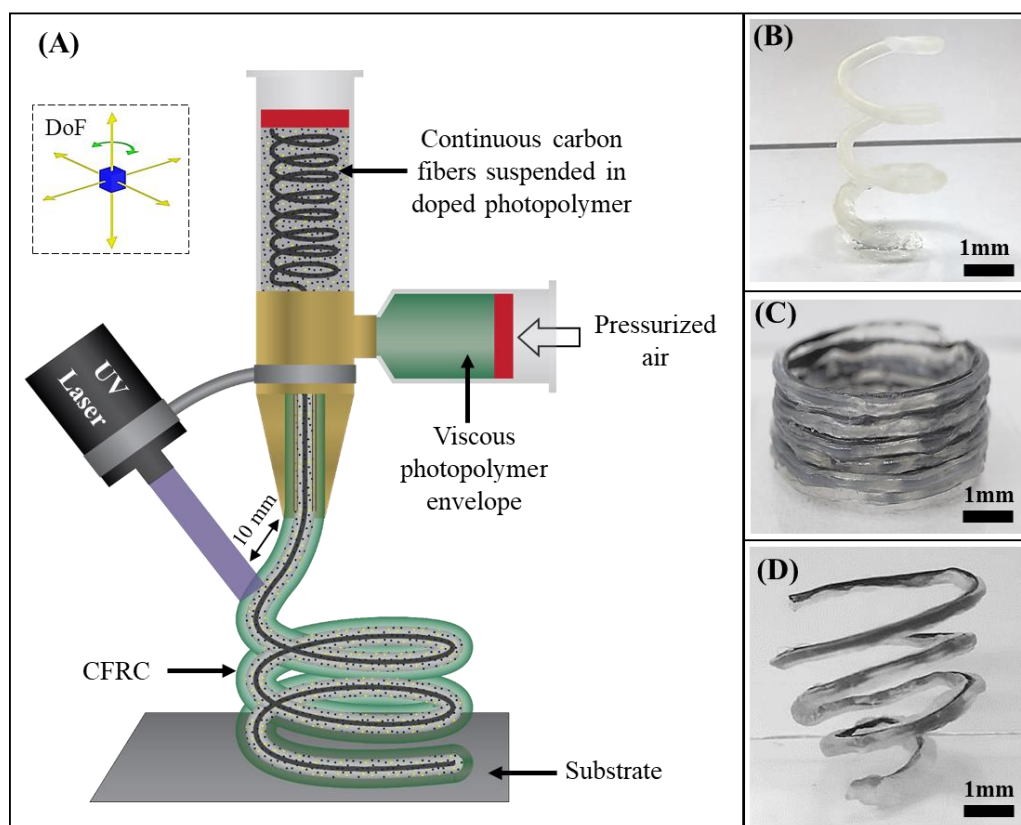


Figure 1. (A) Shows the schematics of the UV-assisted coextrusion deposition of 3D continuous carbon fiber multifunctional composites, as demonstrated by a printed free-standing spiral spring structure in (B), a hollow cylinder structure in (C), and a free-standing tapered spiral spring structure in (D) reinforced with continuous carbon fibers.

### 3. RESULTS AND DISCUSSION

Good printability maintained by resin viscosity and rapid curing was demonstrated in Figure 2(A) by various overhanging structures with inclination angles ranging from  $0^\circ$  to  $75^\circ$ . Due to the brittleness of the selected UV resin, the printed spiral spring structures in Figure 2(B) easily collapsed under compression. With continuous carbon fibers printed within as reinforcement, good structural integrity was still maintained after releasing the compression loads. The thermal image in Figure 2(C) further shows the ability of the printing method in effectively introducing and controlling conductive channels into the nonconductive thermosetting matrix materials as it was resistively heated by the application of a direct current. Such functional structures have promising applications in non-destructive testing and integrated vehicle and structural health management with fibers used as sensor [27], [28].

The potentials of electrochemical performance of continuous carbon fibers were explored by direct printing of a new 3D structural lithium-ion battery [4] as demonstrated in Figure 3(A), where a concentric battery structure was designed: the as-received continuous carbon fibers worked as both anode and current collector; each carbon fiber was coated with thin uniform solid polymer electrolyte, working as both electrolyte and separator; the doped photopolymer worked as both composite matrix and cathode of the structural batteries; the thin aluminum foil was wrapped around cathode materials and used as current collector. It is worth noting that the aluminum current collector was not covering all cathode materials, which instead were enveloped by undoped photopolymer as

insulation to further demonstrate the capabilities of the proposed printing method in direct fabricating multifunctional composite structures with one single step.

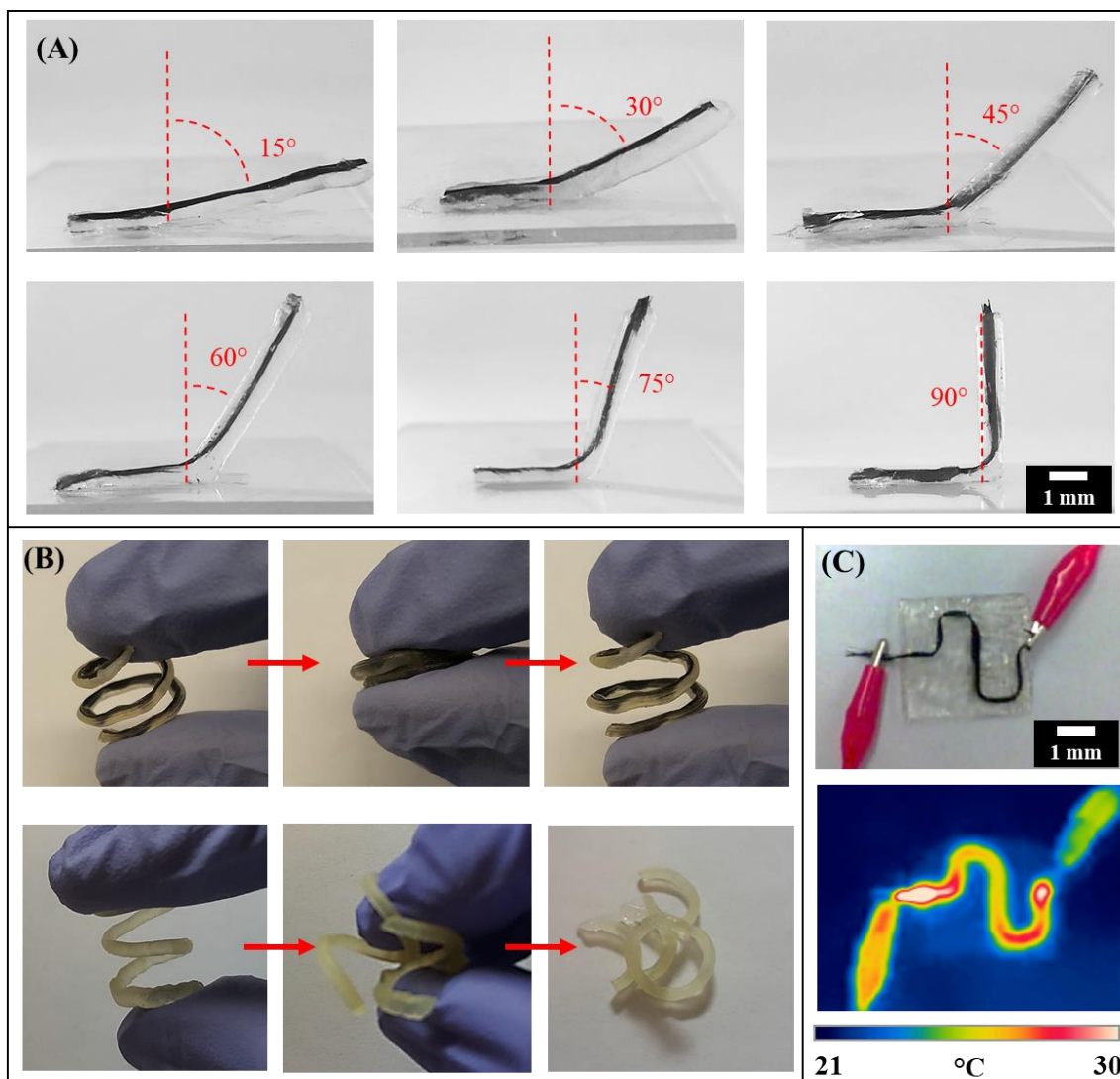


Figure 2. Printed functional parts with continuous carbon fibers: (A) overhanging structure; (B) functional compliant composite materials; (C) proof of concept for a conductive path printed within nonconductive materials.

SPE was prepared with 1M LiClO<sub>4</sub> (less sensitive to the atmospheric moisture [1]) in methoxy polyethylene glycol (350) monomethacrylate (SR550) monomer. A thin

uniform SPE coating, as electrolyte and separator, was then electrocoated on individual carbon fibers following the reported procedure [24]. The cathode doped matrix materials were mixtures of active materials ( $\text{LiFePO}_4$ ) and conductive materials (milled carbon fibers and Super P carbon black) in UV resins, infused with 1M  $\text{LiClO}_4$  in PC/EMC 50/50 vol%. With each carbon fiber acting as a micro-battery cell, high volumetric energy densities are projected to be achieved with closely packed continuous carbon fibers. However, only semi-structural carbon fiber battery cells were fabricated with no load-bearing capabilities due to liquid electrolytes [24]. No research studies could be identified on successfully fabricating this novel 3D battery structure, mainly due to the fabrication difficulties with individually coated carbon fibers. In contrast, the proposed AM method successfully printed a functional full 3D structural battery, as shown in Figure 3(B), capable of powering up a white LED for over 30 seconds after charging for one minute. Figure 3(C) and Figure 3(D), Its cross-section in Figure 3(C) and Figure 3(D) showed a concentric battery structure [4], [29] with intact SPE coating around each carbon fiber. A functional hollow cylindrical 3D structural battery in Figure 3(E) with a same battery design was also successfully printed.

Tensile tests at a loading rate of 1 mm/min were carried out to measure the mechanical properties of the 3D printed cylindrical structural battery (3 mm in diameter and 60 mm in length) shown in Figure 3(B). The measured tensile strength and tensile modulus are shown in Figure 4(A). The corresponding mechanical properties of the undoped photopolymer as provide by the vendor [26] are also included for comparison. With the introduction of 30 vol% continuous fiber reinforcements, an average of 145 MPa in tensile strength and an average of 289 MPa in tensile modulus were achieved.

These were 3.5 times and 138.8 times the corresponding tensile strength and tensile modulus of the photopolymer, respectively, showing the great potentials of the proposed carbon fiber structural batteries in improving the mechanical properties.

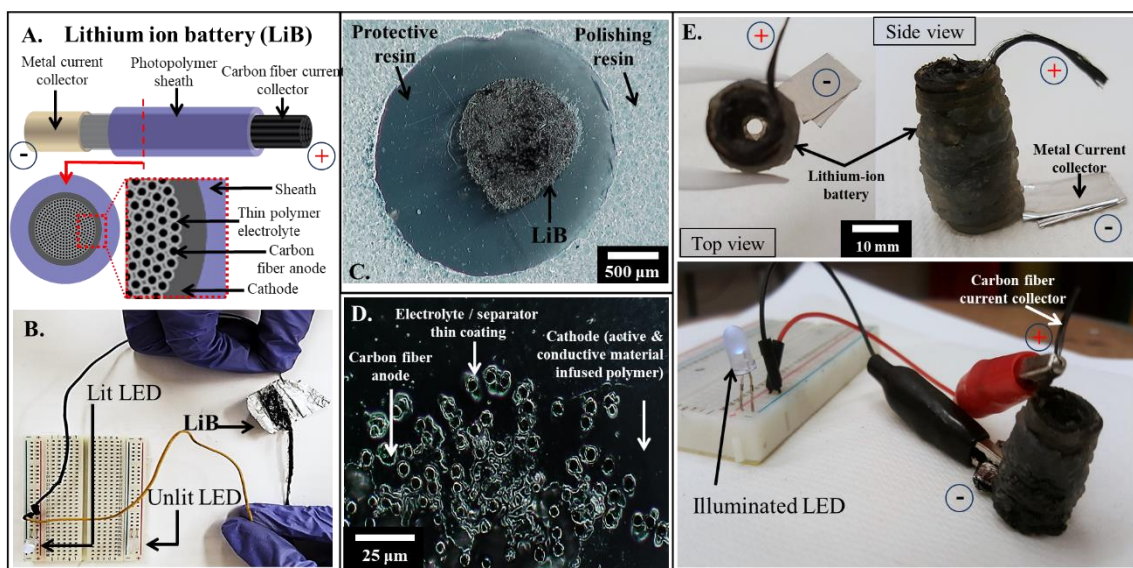


Figure 3. (A) shows the schematics of 3D continuous carbon fiber structural battery structure; (B) shows a printed functional, full cylindrical structural battery with same structure as in (A); (C) reveals the cross-section of the printed battery structure; (D) shows a close-up optical microscope image of the sample in (C), demonstrating SPE coated carbon fibers embedded within cathode materials; (E) shows a printed functional full hollow cylindrical battery structure.

Meanwhile, the electrochemical performance was characterized through specific capacity measured by a Gamry Reference 600+ potentiostat. Figure 4(B) shows the charging-discharging capacity of the same cylindrical structural battery for 10 cycles at a current density of  $10 \text{ mA/cm}^3$ . For the 10 consecutive cycles, it yielded an average volumetric charging capacity of  $0.65 \text{ mAh/cm}^3$  and discharging capacity of  $0.3 \text{ mAh/cm}^3$ , showing an average Coulombic efficiency of nearly 50% after the 10 cycles. The energy and power densities were  $1.05 \text{ Wh/L}$  and  $2.17 \text{ W/L}$ , respectively. It is worth noting that

though these values were much lower than those of conventional lithium-ion full battery cells [30], they were notably higher than those for 3D printed thermoplastic full batteries [31], reported at 0.14 Wh/L and 0.83 W/L for the energy and power densities, respectively.

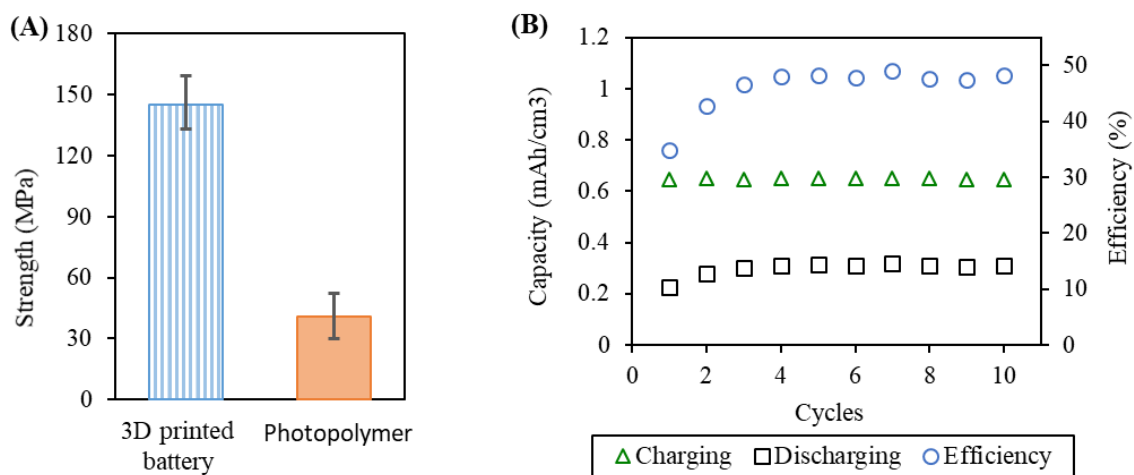


Figure 4. (A) Tensile strength and modulus in comparison of the 3D printed cylindrical structural battery and polymer matrix materials; (B) Capacity and Columbic efficiency of the printed cylindrical structural battery at a current density of 10 mA/cm<sup>3</sup> for 10 cycles.

The low values were attributed to the large percentage of binder, i.e., the photopolymer, necessary for printability but limiting the contact of the doped active and conductive materials. Further studies will also be performed to optimize the polymer composition as well as the dispersion [4] of cathode doped matrix materials within coated carbon fiber network in Figure 3(D).

#### 4. CONCLUSION

This study demonstrated a new printing method for multifunctional composites with 3D continuous carbon fibers. Doped functional matrix materials were coextruded with uncoated or coated carbon fibers through UV-assisted deposition. Its feasibility was demonstrated by several successfully printed multifunctional materials, i.e., free-standing compliant composite structures, composites with conductive channeling, and novel 3D structural battery composite materials. In particular, the proposed was the first study to successfully print a functional, full 3D structural battery with continuous carbon fibers.

#### REFERENCES

- [1] Q. Chen, R. Xu, Z. He, K. Zhao, and L. Pan, "Printing 3D Gel Polymer Electrolyte in Lithium-Ion Microbattery Using Stereolithography," *J. Electrochem. Soc.*, vol. 164, no. 9, pp. A1852–A1857, 2017.
- [2] E. Wong, D. Baechele, K. Xu, R. Carter, J. F. Synder, and E. D. Wetzel, "Design and Processing of Structural Composite Batteries," *Proc. Soc. Adv. Mater. Process Eng. 2007*, vol. 1, pp. 1–20, 2007.
- [3] E. Senokos *et al.*, "Energy storage in structural composites by introducing CNT fiber/polymer electrolyte interleaves," *Sci. Rep.*, vol. 8, no. 1, p. 3407, Dec. 2018.
- [4] L. E. Asp and E. S. Greenhalgh, "Structural power composites," *Compos. Sci. Technol.*, vol. 101, pp. 41–61, Sep. 2014.
- [5] E. Jacques, G. Lindbergh, D. Zenkert, S. Leijonmarck, and M. H. Kjell, "Piezo-Electrochemical Energy Harvesting with Lithium-Intercalating Carbon Fibers," *ACS Appl. Mater. Interfaces*, vol. 7, no. 25, pp. 13898–13904, Jul. 2015.
- [6] E. Jacques, M. H. Kjell, D. Zenkert, and G. Lindbergh, "The effect of lithium-intercalation on the mechanical properties of carbon fibres," *Carbon N. Y.*, vol. 68, pp. 725–733, Mar. 2014.

- [7] Y. Yu *et al.*, “Multifunctional structural lithium ion batteries based on carbon fiber reinforced plastic composites,” *Compos. Sci. Technol.*, vol. 147, pp. 62–70, 2017.
- [8] M. H. Kjell, E. Jacques, D. Zenkert, M. Behm, and G. Lindbergh, “PAN-Based Carbon Fiber Negative Electrodes for Structural Lithium-Ion Batteries,” *J. Electrochem. Soc.*, vol. 158, no. 12, p. A1455, 2011.
- [9] M. H. Kjell, T. G. Zavalis, M. Behm, and G. Lindbergh, “Electrochemical characterization of lithium intercalation processes of PAN-based carbon fibers in a microelectrode system,” *J. Electrochem. Soc.*, vol. 160, no. 9, pp. 1473–1481, 2013.
- [10] W. Johannisson *et al.*, “Multifunctional performance of a carbon fiber UD lamina electrode for structural batteries,” *Compos. Sci. Technol.*, vol. 168, pp. 81–87, Nov. 2018.
- [11] L. J. Love *et al.*, “The importance of carbon fiber to polymer additive manufacturing,” *J. Mater. Res.*, vol. 29, no. 17, pp. 1893–1898, Sep. 2014.
- [12] T. Hofstätter, D. B. Pedersen, G. Tosello, and H. N. Hansen, “State-of-the-art of fiber-reinforced polymers in additive manufacturing technologies,” *J. Reinf. Plast. Compos.*, vol. 36, no. 15, pp. 1061–1073, Aug. 2017.
- [13] P. Parandoush and D. Lin, “A review on additive manufacturing of polymer-fiber composites,” *Compos. Struct.*, vol. 182, pp. 36–53, Dec. 2017.
- [14] B. Brenken, E. Barocio, A. Favaloro, V. Kunc, and R. B. Pipes, “Fused filament fabrication of fiber-reinforced polymers: A review,” *Addit. Manuf.*, vol. 21, no. October 2017, pp. 1–16, May 2018.
- [15] E. R. Fitzharris, N. Watanabe, D. W. Rosen, and M. L. Shofner, “Effects of material properties on warpage in fused deposition modeling parts,” *Int. J. Adv. Manuf. Technol.*, vol. 95, no. 5–8, pp. 2059–2070, Mar. 2018.
- [16] J. P. Lewicki *et al.*, “3D-Printing of Meso-structurally Ordered Carbon Fiber/Polymer Composites with Unprecedented Orthotropic Physical Properties,” *Sci. Rep.*, vol. 7, p. 43401, Mar. 2017.
- [17] R. Matsuzaki *et al.*, “Three-dimensional printing of continuous-fiber composites by in-nozzle impregnation,” *Sci. Rep.*, vol. 6, no. 1, p. 23058, Sep. 2016.
- [18] X. Tian, T. Liu, C. Yang, Q. Wang, and D. Li, “Interface and performance of 3D printed continuous carbon fiber reinforced PLA composites,” *Compos. Part A Appl. Sci. Manuf.*, vol. 88, pp. 198–205, Sep. 2016.

- [19] C. Yang, X. Tian, T. Liu, Y. Cao, and D. Li, "3D printing for continuous fiber reinforced thermoplastic composites: Mechanism and performance," *Rapid Prototyp. J.*, vol. 23, no. 1, pp. 209–215, 2017.
- [20] N. Volpato, D. Kretschek, J. A. Foggatto, and C. M. Gomez da Silva Cruz, "Experimental analysis of an extrusion system for additive manufacturing based on polymer pellets," *Int. J. Adv. Manuf. Technol.*, vol. 81, no. 9–12, pp. 1519–1531, Dec. 2015.
- [21] F. Ning, W. Cong, Y. Hu, and H. Wang, "Additive manufacturing of carbon fiber-reinforced plastic composites using fused deposition modeling: Effects of process parameters on tensile properties," *J. Compos. Mater.*, vol. 51, no. 4, pp. 451–462, Feb. 2017.
- [22] C. E. Duty *et al.*, "Structure and mechanical behavior of Big Area Additive Manufacturing (BAAM) materials," *Rapid Prototyp. J.*, vol. 23, no. 1, pp. 181–189, Jan. 2017.
- [23] B. Huang and S. Singamneni, "Raster angle mechanics in fused deposition modelling," *J. Compos. Mater.*, vol. 49, no. 3, pp. 363–383, Feb. 2015.
- [24] S. Leijonmarck, T. Carlson, G. Lindbergh, L. E. Asp, H. Maples, and A. Bismarck, "Solid polymer electrolyte-coated carbon fibres for structural and novel micro batteries," *Compos. Sci. Technol.*, vol. 89, pp. 149–157, Dec. 2013.
- [25] J. Hagberg *et al.*, "Lithium iron phosphate coated carbon fiber electrodes for structural lithium ion batteries," *Compos. Sci. Technol.*, vol. 162, pp. 235–243, 2018.
- [26] Elegoo, "ELEGOO 3D Rapid Resin LCD UV-Curing Resin 405nm Standard Photopolymer Transparent Resin," *Elegoo Inc.*, 2018. [Online]. Available: <https://starging.elegoo.com/product/elegoo-3d-rapid-resin-lcd-uv-curing-resin-405nm-standard-photopolymer-resin-500gram-transparent/>. [Accessed: 15-Apr-2019].
- [27] J. Leng and A. Asundi, "Structural health monitoring of smart composite materials by using EFPI and FBG sensors," *Sensors Actuators, A Phys.*, 2003.
- [28] I. Kang, M. J. Schulz, J. H. Kim, V. Shanov, and D. Shi, "A carbon nanotube strain sensor for structural health monitoring," *Smart Mater. Struct.*, 2006.
- [29] J. Xu, G. Lindbergh, and J. Varna, "Carbon fiber composites with battery function: Stresses and dimensional changes due to Li-ion diffusion," *J. Compos. Mater.*, vol. 52, no. 20, pp. 2729–2742, Aug. 2018.

- [30] Y.-K. Sun, S.-T. Myung, B.-C. Park, J. Prakash, I. Belharouak, and K. Amine, “High-energy cathode material for long-life and safe lithium batteries,” *Nat. Mater.*, vol. 8, no. 4, pp. 320–324, Apr. 2009.
- [31] C. Reyes *et al.*, “Three-Dimensional Printing of a Complete Lithium Ion Battery with Fused Filament Fabrication,” *ACS Appl. Energy Mater.*, vol. 1, no. 10, p. acsaem.8b00885, Oct. 2018.

## V. ADDITIVE MANUFACTURING OF A POLYMER LITHIUM-ION STRUCTURAL BATTERY WITH 3D CONTINUOUS CARBON FIBER ANODE VIA COEXTRUSION DEPOSITION

Aditya R. Thakur <sup>1</sup>, Xiangyang Dong <sup>1\*</sup>

<sup>1</sup> Department of Mechanical and Aerospace Engineering, Missouri University of Science and Technology, 400 W. 13th St., Rolla, MO 65409.

\* Corresponding author

### ABSTRACT

Structural battery composites are actively being studied as materials that could potentially provide mass-less energy storage by catering electrical and mechanical requirements, simultaneously. Studies have shown that modern additive manufacturing techniques can be used to produce customized-to-fit battery form factor that can concurrently serve as a functional structural component. This study discusses a contemporary coextrusion-based additive manufacturing (AM) process developed to fabricate multifunctional energy composites that can be used as structural batteries, composition of which emulates a lithium-ion battery. The proposed structural battery uses 3D continuous conductive carbon fiber tows as anode and current collector. These fibers are coated with lithium-ion conductive polymer which acts as a solid polymer electrolyte (SPE) and separator. The coated carbon fiber tows reinforces (carbon) conductive and (lithium iron phosphate  $\text{LiFePO}_4$ ) active material infused (Polyvinylidene fluoride PVDF) thermoplastic fluoropolymer cathode matrix. A coextrusion process was implemented to simultaneously deposit full-cell composition with reinforcing coated

carbon fibers to fabricate a complete lithium-ion structural battery in single deposition. The design rationale is detailed in this work, corroborating parametric study optimizing the viscosity and the solid load composition of the cathode slurry used in the fabrication process. The electrochemical characterization of the fabricated energy composites illustrated stable cyclic performance. The continuous carbon fiber anode, also employed as a fiber reinforcement within the composite, provides practical mechanical advantage. Microstructural analyses was conducted to investigate the effect of cathode slurry viscosity and composition on the electrochemical and mechanical performance of the energy composite. The proposed process yields energy composites with excellent mechanical and electrochemical properties with added benefit of customizability facilitated by 3D printing. Thus, establishing the potential of the proposed method to directly print functional structural energy composites aimed to provide mass-less energy storage for electrically powered structural systems, especially in aerospace, automotive and consumer electronic applications where large capacities and low weights are desired.

*Keywords: additive manufacturing, lithium-ion structural battery, continuous carbon fiber, PVDF cathode*

## 1. INTRODUCTION

Lithium-ion batteries, owing to their excellent energy and power densities, are one of the leading battery technologies and are extensively used in industrial as well as consumer applications including but not limited to aviation, automotive, consumer electronics, etc. [1]–[5]. The size and the shape of the battery package has a significant

impact on the battery life and design of the products they power [6]. Typically, a commercially available lithium-ion battery is of a conventional rectangular or cylindrical shape, comprising of electrodes, electrolyte, separator and current collectors [3]. Generally, the batteries or battery packs are treated as auxiliary components, and the approach to improve volumetric efficiency has been to minimize the weight of the energy storage systems [7]. However, this approach reaches its potential threshold as the fabrication techniques are inconvenient for the scaled-up manufacturing, which is necessary for powering larger, practical energy systems [8]. Alternatively, development of multifunctional composite structures [9], [10], and materials [11] is being investigated with an aim to provide mass-less energy storage for electrically powered structural systems [12]. Structural energy composites address this need to maximize energy storage and simultaneously minimizing size and weight by intrinsically storing electrical energy while being a part of the load carrying structure itself [13]. Benefits of such multifunctional composites, where every constituent performs multiple functions, are numerous and diverse [11], [12], [14], and they are being investigated as functional engineering materials in several different means [2], [9], [15]–[17]. This facilitates a significant increment in system-wide energy and power densities upon being used as an integrated battery and load-carrying part [18], [19]. Practical examples of such applications include their use as structural batteries in the form of body panels for electric vehicles and structural components within unmanned aerial vehicles [1], [11], [17], [20], [21]. Wide-spread usage for such applications generally require customizable, unconventional form factor. Studies exploring paintable [3], printable [22], paper thin [23], stretchable [24] battery fabrication approaches have assisted in eliminating the form

factor restrictions that traditional batteries posed [25]–[27]. However, most of these prototype fabrication methods are restricted to curved or flat surfaces [28]–[31]. This limitation can be overcome through three-dimensional printing which enables the creation of complex 3D objects as well as rapid changes in the design without requiring substantial modifications to the manufacturing process [26].

There have been studies investigating 3D printing of conductive materials with an intent to inculcate multi-functionality into the printed structures. Conductive circuits and electronics have been 3D printed in conjunction with traditional batteries via fused filament fabrications and conductive inks [30], [32]. In fact, studies have also explored the possible usage of additive manufacturing approach to fabricate 3D lithium-ion structural batteries itself. However, these studies have been typically restricted to half-cell fabrications through layering using conductive additives to impart conductivity to the polymers [33]. The mechanical properties of these batteries are dictated by the nature of the polymer used, with a standard compromise between battery performance and mechanical behavior [26], [34]. This is because, improved mechanical characteristics in such structural batteries imply higher volume percentage of polymer and lower additives; vice versa for electrical characteristics.

Conductive graphitized carbon fibers have been shown to be an excellent candidate for reinforcement and primary component within multifunctional energy composites. They have an ability to simultaneously store and harvest energy while carrying mechanical loads [17], [35]–[37]. Continuous, self-standing carbon fiber tows, upon being implemented as electrodes, imbibe commendable mechanical properties [17]. Their high specific tensile properties and carbonaceous microstructure provide

mechanical advantage while promoting reversible lithium-ion intercalation reactions, respectively [38]. They are more electrochemically stable than metallic aluminum [39], with low electrical resistivity in the order of  $10^{-3} \Omega \cdot \text{cm}$  [17]. Therefore, carbon fibers are actively being investigated and integrated within structural energy composites [11], [40], [41].

The highest level of integration in multifunctional energy composites is realized by depositing electrolyte and cathode materials directly on a single carbon fiber [42], where each individual carbon fiber directly acts as one battery electrode and current collector [36]. Therefore, in this study, through the use of continuous conductive carbon fiber tows, the fibers were simultaneously employed as mechanically reinforcing component and as anode and current collector. This helps in concurrently addressing the compromise drawn between aforementioned battery performance and mechanical behavior [17]. Majority of the present multifunctional carbon fiber reinforced structural battery composites are based on a laminated battery structure. These are fabricated through the conventional lay-up processes [10], [13], [43], [44] that incur high fabrication costs and cycles. This has hindered the widespread implementation of multifunctional materials and structures [34].

Additive fabrication of continuous fiber reinforced thermoplastics has been looked into from a mechanical advantage and customizability point of view with studies using traditional fused filament fabrication approach [45]–[53]. However, it has been noted that addition of active and conductive fillers into the polymers deteriorates its printability and mechanical behavior in multiple ways. Large volumes of active-conductive fillers, though indorses electrochemical behavior, the structural aspect of the

multifunctional energy composites get largely compromised. Presence of high-strength, high-modulus conductive carbon fiber as reinforcement assists in addressing this compromise [34]. Whereas, the clogging issues associated with layer by layer deposition of multiphase composites with high volume of active-conductive dopants [26] could be adequately addressed through coextrusion deposition. Until recently, coextrusion-based fabrication was explored mainly to manufacture energy textiles. However, their applications as structural components is hindered by their characteristic pliability and intended low power applications [54]–[56]. In current study, active-conductive material infused PVDF cathode slurry is coextruded, along with continuous carbon fiber anode with flexible monomer coating to 3D print a complete lithium-ion structural battery with continuous fiber reinforcement for the first time. We hypothesized that active-conductive material infused PVDF could be used as cathode in conjunction with monomer separator / electrolyte and continuous carbon fiber anode enabling AM of a lithium ion structural battery. The role of the conductive carbon fiber core is not just as an excellent electrode but also act as a reinforcement for the otherwise weak thermoplastic fluoropolymer cathode envelope, truly forming a functional load-carrying structural battery with notable discharging capacity and high Coulombic efficiency.

## **2. EXPERIMENTAL PROCEDURE**

### **2.1. MATERIAL PREPARATION**

**2.1.1. Polymer Cathode.** Modern solid state lithium-ion batteries utilize lithium transition metal oxides as active material in cathode in conjunction with conductive

materials and binder. For current set-up, lithium iron phosphate ( $\text{LiFePO}_4$  by Sigma-Aldrich) was selected as the electrochemically active material in cathode because of its high theoretical specific capacity (170 mAh/g), good cycling stability, higher safety, low cost, and non-toxicity [57]–[61]. Carbon conductive additive (Super P conductive carbon black by Alfa Aesar) was considered as a primary conductive material for its conductive prominence due to its low resistivity [62], and MF80 milled short carbon fiber strands (by Carbiso) was considered as a supplementary conductive material. Along with improved structural integrity, studies have suggested improved power performance and energy density for  $\text{LiFePO}_4$  cathodes with a mixture of carbon black and carbon fiber as conductive additive for a given volume fraction [63]. Although,  $\text{LiFePO}_4$  has poor electrical conductivity ( $\sim 10^{-9} \text{ S cm}^{-1}$ ) and lithium diffusivity ( $\sim 8 \times 10^{-18} \text{ m}^2 \text{ s}^{-1}$ ), it can be compensated by using smaller particle sizes along with sufficiently large amount of carbon conductive additives to achieve desired electrical performance [64]–[67]. Poly(vinylidene fluoride) (PVDF by Sigma Aldrich) was used as a binder to prepare cathode matrix material due to its high ionic conductivity (order of  $10^{-4} \text{ S/cm}$  at  $20 \text{ }^\circ\text{C}$ ) when used as a binder in conjunction with active materials [68].

For the cathode material, preliminary studies have reported that the slurry comprising of  $\text{LiFePO}_4$ :Super-P carbon:PVDF at 54:34:12 ratio by weight in Dimethylformamide (DMF) solvent, upon evaporation of the solvent, provided capacity of nearly 60%, with  $102 \text{ mAhg}^{-1}$ , compared to the theoretical  $170 \text{ mAhg}^{-1}$ , when electrochemically cycled at C/5 [12]. Upon up-scaling the manufacturing process, this composition was determined to be inefficient for additive manufacturing of structural battery as the serviceability of the binder/carbon material is compromised during the

evaporation of the solvents. Thus, requiring excess binder material to compensate for its insufficient bonding strength [69], [70]. Therefore, conductive milled short carbon fiber strands were added as supplementary conductive material as the increase in the aspect ratio of the conductive filler improves the conductivity of the network for a given volume fraction of additive [33], [63]. Hence, minimizing the need to excessively increment the binder weight percent within the cathode slurry composition.

For current composition, through a parametric study, the cathode slurry with  $\text{LiFePO}_4$ :Super-P carbon:Milled short carbon fiber:PVDF at 45:12:18:25 ratio by weight in DMF solvent was determined to be apt for coextrusion deposition. Although, higher aspect ratio conductive additives improve the conductivity within the cathode due to the reduced sensitivity to inter-particle contact, the processibility of the cathode is negatively affected [63], especially during coextrusion deposition [34]. Therefore, a parametric study was conducted to determine maximum addition of milled conductive carbon fibers that allow coextrusion without clogging. A combination of carbon black and milled carbon fibers as conductive additive within the cathode material at 40:60 weight ratio (8:7 volume ratio), respectively, provided a highly conductive network that connects well to the active material particles and the current collector [63], without hampering the coextrusion process. The ratio of active to conductive materials was maintained at 3:2 by weight replicating the slurry composition reported by Asp and coworkers [12] for 3D-fiber structural battery. A minimum 25 wt.% of PVDF binder was found necessary to be present in the slurry to allow printing of complex structures at ambient temperature and pressure, ensuring shape retention for the deposition while the solvent evaporates.

The cathode slurry was prepared by mixing finely ground ( $<5\ \mu\text{m}$  particle size)  $\text{LiFePO}_4$  with Super-P carbon, milled short carbon fibers and PVDF along with the DMF solvent using the AR100 planetary centrifugal mixer (by ThinkyUSA) at 2000 RMP for 20 min at ambient temperature and pressure. The slurry was then defoamed and transferred to the syringes to be used for additive fabrication.

The viscosity of the slurry was moderated through the variation in solvent volume. To study the effect of the solvent volume percentage on the slurry and the resulting cathode material, a parametric study with varying solid load:DMF solvent ratio by volume between 1:3 to 1:5 was carried out. The slurry rheology for different solvent volume percentage was measured by a viscometer (Brookfield model HB) equipped with a solid shaft SC4-27SD spindle at  $25\ ^\circ\text{C}$ , results of which are detailed in the following Figure 1(A).

The mechanical strength of the printed multifunctional battery composite is also critical and is often dictated by the strength of the polymer cathode matrix. The mechanical performance of the matrix is governed by the binder volume percentage. Higher binder within the solid load usually corresponds with enhanced mechanical performance, but reduced electrochemical performance, and vice-versa [71]. Therefore, a parametric study was also carried out to investigate the effect of increasing binder volume percentage in the cathode slurry on the mechanical and electrochemical performance of the printed battery composites.

This was achieved by maintaining the weight ratio of  $\text{LiFePO}_4$ :Super-P carbon:Milled short carbon fiber constant at 15:4:6 and varying the weight ratio of PVDF binder within the solid load between 25% and 45% by weight. The ratio of the resulting

solid load:DMF solvent was maintained consistent at 1:4.5 as it found to be apt for coextrusion deposition. At least 25 wt.% of PVDF binder is necessary to allow printability of simple structures at ambient temperature and pressure.

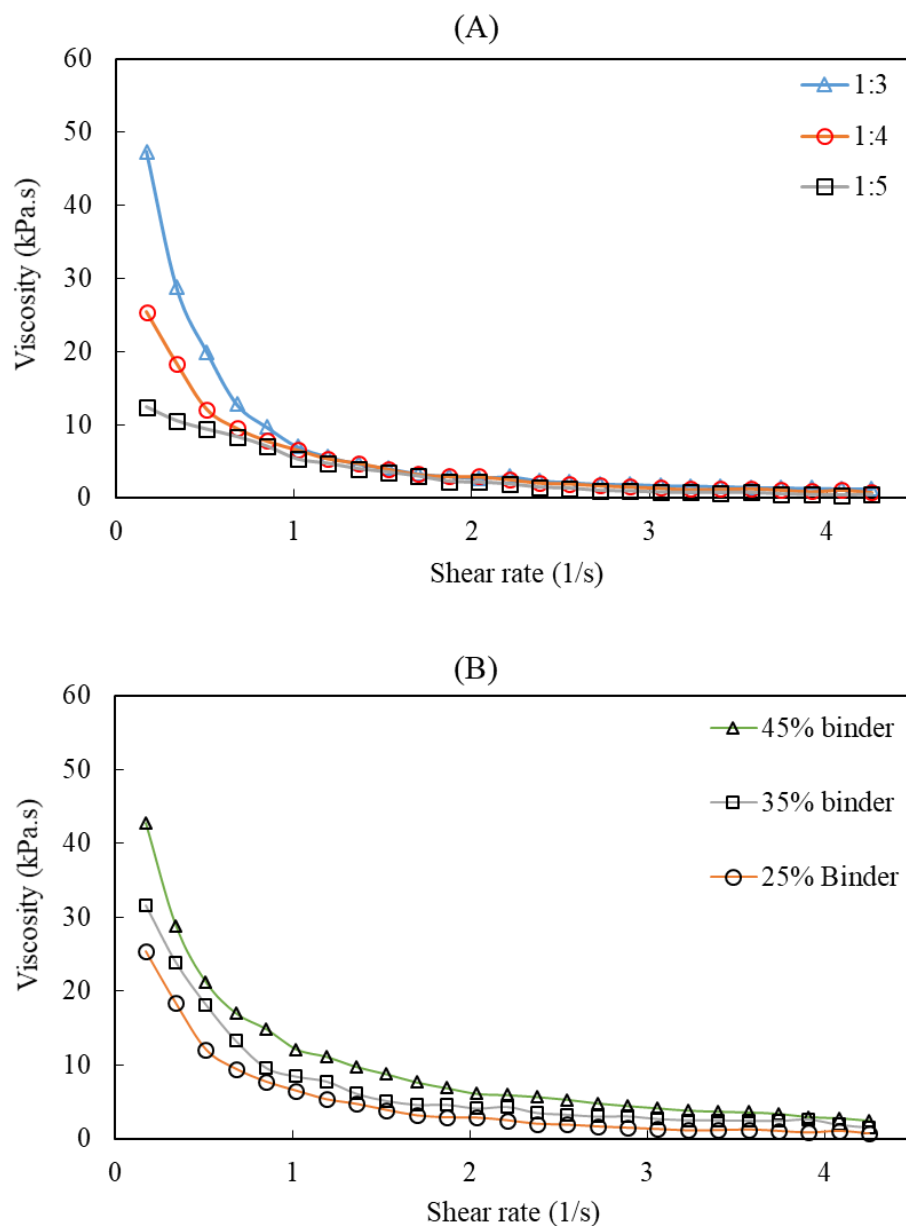


Figure 1. Viscosity vs. shear rate for cathode slurry with (A) varying solid load:DMF solvent volume ratio with 25 wt.% binder in the solid load, and (B) varying binder wt.% in the solid load with consistent solid load:DMF solvent volume ratio of 1:4.5.

For binder volume percentage exceeding 45 wt.% in the solid load, for a solvent volume ratio of 1:4.5, the coextrusion process would lead to discontinuous deposition. This was further established via printability window estimated for the current 3D printing set-up, as discussed in the later section.

We draw an hypothesis that though the mechanical performance of the resulting cathode material improves with higher binder volume percentage within the solid load, while the electrochemical performance depreciates [71], the trend in mechanical and electrochemical behavior of the resulting composite may not vary linearly, especially for the additively fabricated multifunctional fiber reinforced composites . We speculate that the permeability of the cathode slurry into the reinforcing SPE carbon fiber anode, fiber volume fraction of reinforcing continuous carbon fiber, and the changes in adhesive properties of the cathode slurry may have a notable influence on the mechanical and electrochemical performance of the printed composites. This proposition is investigated in later sections through the mechanical and electrochemical characterization of the printed battery structures, followed by the microstructural analyses.

**2.1.2. Carbon Fiber Anode and Current Collector.** To inculcate multi-functionality, while maintaining a compact, standalone and inclusive structure, a commercially available Polyacrylonitrile (PAN)-based Toray T800HB graphitized 12K continuous carbon fiber tows were used as anode and current collector [17], [72], [73]. The highly conductive nature of the graphitized carbon fibers along with lithium-ion intercalation capabilities enables them to perform as an anode as well as a current collector within the energy composites [17], [74], [75], while simultaneously improving the load carrying capacity of the structure [35], [37], [76]. These carbon fiber tows were

dried in the vacuum oven at 120 °C for at least four hours to remove moisture. This helps in minimizing the negative effect of moisture on the conductivity and lithium-ion intercalation capabilities of carbon fibers and promotes polymer adhesion [77], [78]. Drying also helps in reducing the fiber clumping during coextrusion process which can be detrimental to the deposition quality, and subsequently the mechanical properties of the fiber reinforced structures [79].

## **2.2. EXPERIMENTAL SET-UP**

**2.2.1. Electro-grafting Setup for Solid Polymer Electrolyte (SPE).** To coat carbon fibers with functional SPE, an electrolytic solution comprising of monoethoxy polyethylene glycol (350) monomethacrylate (SR550) monomer with 1 M of lithium salt as supporting electrolyte for the electrocoating process was prepared. The monomer was specifically chosen for its high ionic conductivity of  $1.5 \times 10^{-7} \text{ S cm}^{-1}$  (measured at 258 °C) with low stiffness of <1 MPa making the coating ideal for 3D printed structural electrode [34], [80]. Low stiffness specifically aid the 3D printing process, as the acquired pliability of the coated carbon fiber tows allowed printing of intricately shaped structures with reinforcing 3D continuous carbon fibers. Lithium perchlorate ( $\text{LiClO}_4$  by Sigma-Aldrich) was selected as supporting electrolyte for the study due to its existing extensive application in lithium-ion batteries [81]. Using  $\text{LiClO}_4$  as a supporting electrolyte in electrochemical polymerization minimizes the need for subsequent post-polymerization swelling to introduce lithium salts into SPEs [72], [81]. The solution was mixed using magnetic stirrer until the  $\text{LiClO}_4$  particles were adequately dispersed. DMF at 1:2 volume ratio of monomer solution was then added by continued stirring until the

$\text{LiClO}_4$  particles were completely dissolved. DMF as a solvent has been proven to work with methacrylate systems; thus was used in the electrocoating process [82]. The temperature of this solution was then steadily increased to 62 °C while continually stirring. The prepared electrolytic solution was then agitated to eliminate any air-bubbles.

The electrochemical polarization set-up with three-electrode assembly to add SPE coating on continuous carbon fiber tows is illustrated in the following Figure 2(A). This setup comprises of a petri dish, a Teflon plate, a lithium foil as reference electrode, an aluminum foil as counter electrode, a glass fiber mesh separator (plain weave e-glass), conductive carbon fibers as working electrode, and 2450 EC Keithley potentiostat equipped with three electrode assembly for polarization.

To coat the carbon fibers, the setup illustrated in Figure 2(A) is introduced inside a high-purity argon purged glovebox (<1 ppm oxygen and water at ambient temperature). A cyclic potential sweep using voltammogram is applied to record passivation peak voltage which corresponds to the potential at which the conductive substrate (carbon fibers) are coated by grafting SPE from the monomer solution [72], [82]. The grafting peak voltage (between 800 mV to 120 mV) is then applied during polarization for 400 seconds providing coating composition, thickness and morphology required for the proposed coextrusion deposition, as illustrated in Figure 2(B).

Studies have explored the idea of SPE-coated carbon fibers to be used as electrodes in structural batteries [9], [18], [72], [83]. However, the scope of such projects had been limited to short length carbon fiber tows (~ 25 mm), establishing the proof of concept [72]. On the other hand, using the abovementioned process continuous carbon

fiber tows with excellent conductivity and pliability have been used in large scale additive manufacturing of structural energy composites [34].

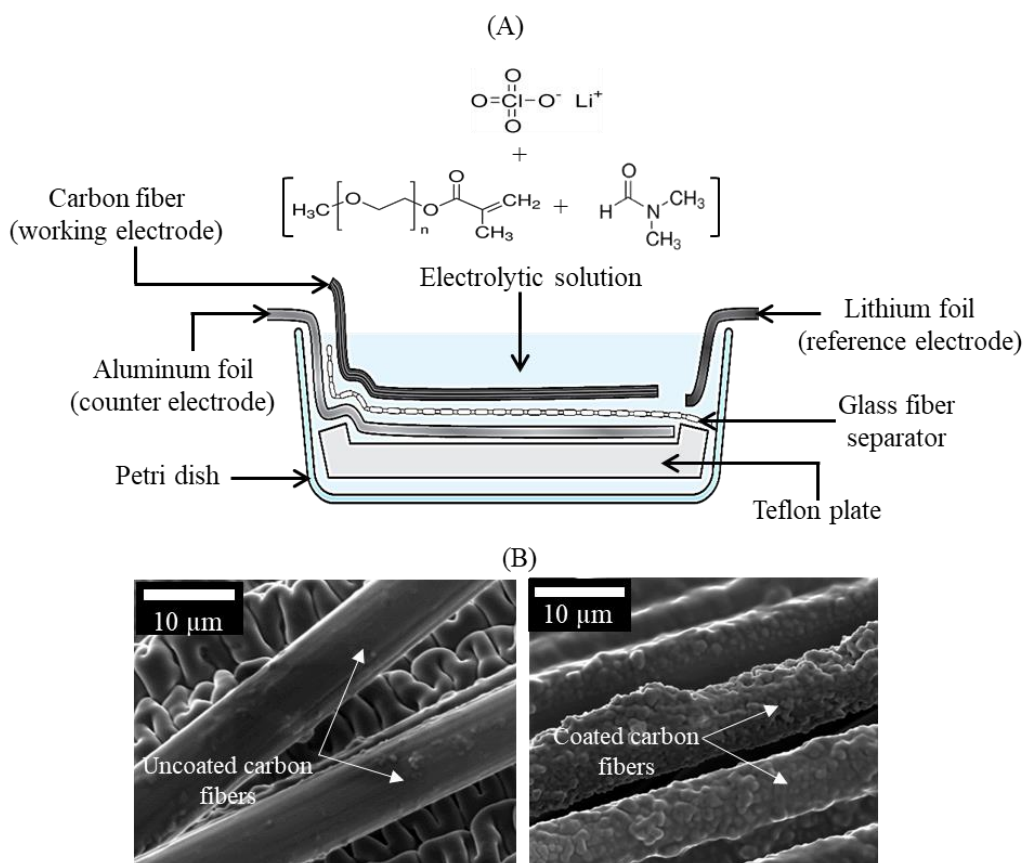


Figure 2. (A). Schematics of the set-up for SPE coating on carbon fiber tows, and (B) SEM images comparing uncoated and coated carbon fibers procured through the electro-grafting process.

This set-up allows coating of 300 mm long carbon fiber tow, with a potential to scale up. Ideally, a thorough but thin coating is desired on carbon fiber tows for solid structural battery applications. A thorough coating minimizes potential short-circuiting issues within the structure, while the thin coating ensures minimal resistance and adequate conductivity of ions during battery applications [20], [72]. However, if the

coating is too thin, it susceptible to damage during coextrusion process which may incite short-circuiting issues within the printed battery structure [34].

**2.2.2. Coextrusion Deposition Setup.** The schematics of the proposed coextrusion deposition setup is illustrated in Figure 3. The setup in conjunction with Shirline 4-axis CNC machine, uses two separate dispensers with a coaxial extrusion nozzle, with an inner nozzle diameter of 0.6 mm and an outer nozzle diameter of 1.2 mm. The inner nozzle is connected to the vertical dispenser which is used to feed continuous carbon fibers (anode) with uniform SPE coating (electrolyte and separator) [36], [72] along with cathode slurry comprising of active and conductive materials in DMF with PVDF binder. The outer nozzle, connected to the horizontal dispenser, feeds an identical cathode slurry. This dual nozzle set-up that promotes pre-impregnation of coated carbon fibers in the vertical dispenser, helps in improving the fiber-matrix bonding while simultaneously increasing the drag force that facilitates coextrusion process. Otherwise, the drawing forces during deposition would damage the SPE coating. [34].

Upon application of pressurized air, the SPE coated continuous carbon fibers are first impregnated and extruded with cathode slurry through inner nozzle, and then are further sheathed and coextruded with the slurry from the outer nozzle, before being deposited on the substrate layer-by-layer [34], [47], [48], [84]. Thus, the coextrusion process enables adequate impregnation and thorough coating of the reinforcing carbon fibers, assisting with shape retention of the deposition, and simultaneously avoiding nozzle clogging throughout the printing process.

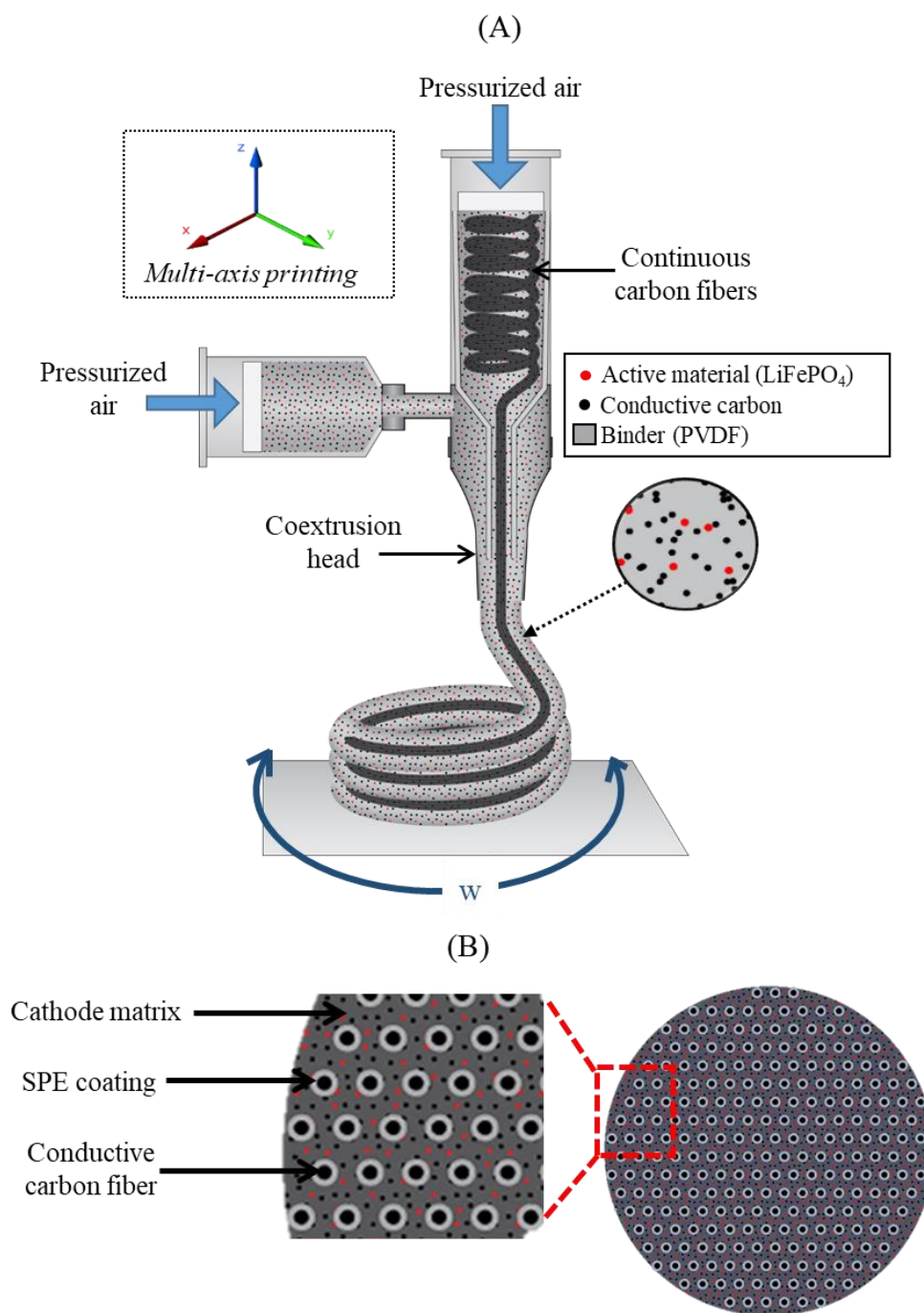


Figure 3. Schematic diagram depicting (A) coextrusion deposition of full lithium-ion battery with 3D continuous carbon fiber anode. The inset image illustrates the composition of active (red), conductive (black) and binder (gray) material fed through the inner and outer nozzle, being coextruded with the coated carbon fiber, and (B) the cross section of the fabricated concentric structural battery composite with each individual SPE-coated carbon fiber dispersed in cathode matrix working as micro-battery cells.

Flow rate of  $1.7 \text{ mm}^3/\text{sec}$  (volume based on the orifice) was measured for printing speed of up to 2 mm per second. However for illustration, conservative printing speed of 0.5 mm per second was used as it works thoroughly for viscosity range between 12 and 50 Pa.s, shear stress for which was controlled by moderating the pressure on the dispenser. To determine the printability window for the additive fabrication of the proposed energy composites, shear rate and shear stress were estimated. The process-related shear-stress while printing was measured by relating it to the extruding pressure and the nozzle geometry, calculating the yield stress in the coaxial nozzle [85]. The process-related shear rate was estimated from the volumetric flow rate of the slurry, taking into account the Rabinowitch-Mooney correction factor for non-Newtonian fluid [86], [87]. For the current cathode slurry composition and the 3D printing set-up with the coextrusion nozzle, at the shear rate of less than  $0.5 \text{ sec}^{-1}$ , the coextrusion process was hampered due to the higher viscosity of the cathode slurry, and would thus lead to a discontinuous deposition. Whereas, for the shear rate higher than  $10.2 \text{ sec}^{-1}$ , the evaporation rate of the solvent at the ambient temperature and pressure would prove inadequate to maintain the structural integrity of the coextruded and deposited carbon fiber reinforced composites. This could lead to an extremely poor printing resolution, impeding the additive fabrication aspect of the process. The printability window, based on the shear rate, could be expanded by incorporation of printing set-up with elevated temperature and controlled ambient pressure, moderating the evaporation of the DMF solvent within the cathode slurry. Future studies will be performed to study the effects of printing environments on printed structural batteries.

Although, the set-up is capable of applying up to 100 Psi pressure, exceeding 70 Psi of extruding pressure would lead to cathode material sagging during coextrusion deposition using current setup. On the other hand, extruding pressure less than 20 Psi prove to be inadequate for the coextrusion of carbon fiber tow along with the encompassing cathode slurry. Thus, limiting the applicable shear stress for the proposed printing process, using current apparatus, to be between 1.5 kPa and 10 kPa. The following Figure 4(A) and Figure 4(B) illustrates the measured shear stresses and rates for the cathode slurries with varying solvent volume and binder wt.%, respectively. The printability window shown in the figures is projected based the aforementioned limitations of the current 3D printing setup.

The deposition is carried out at ambient temperature under a fumed hood, after which it is introduced inside a vacuum oven for at least 24 hours at 80 °C, to ensure complete evaporation of DMF solvent. The process yields a ‘full’, solid state, polymer structural lithium-ion battery, comprising of SPE coated 3D continuous carbon fiber anode embedded within PVDF-based polymer cathode matrix infused with active-conductive material. The reinforcing carbon fibers imparts mechanical strength to the PVDF cathode matrix and improves the longevity of the structural battery by imbining load carrying capacity to it. A schematic illustration of the disposition obtained through the abovementioned process is illustrated in Figure 5(A), and an SEM image demonstrating the actual structure of the battery composite with reinforcing coated carbon fiber anode and current collector, embedded within the porous polymer cathode matrix, is illustrated in Figure 5(B). The bright particles distributed across the porous

cathode matrix are the active particles of  $\text{LiFePO}_4$ , whereas conductive SuperP carbon with particle size  $< 40\text{nm}$  is difficult to distinguish at the demonstrated scale.

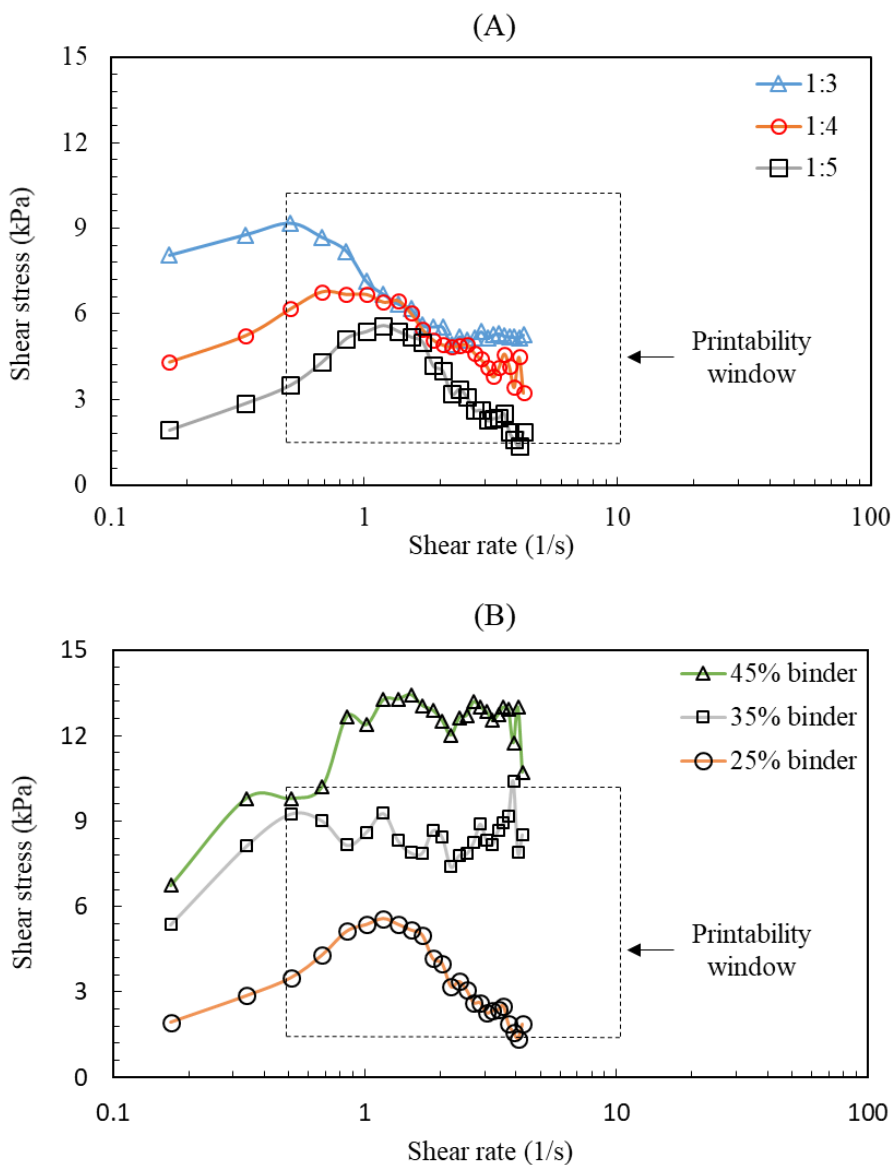


Figure 4. Shear stress vs. shear rate for cathode slurries with (A) varying solid load:DMF solvent volume ratio with 25 wt.% binder in the solid load, and (B) varying binder wt.% in the solid load with solid load:DMF solvent volume ratio of 1:4.5. The corresponding printability windows are presented as the areas within the dashed lines.

Each carbon fiber filament within the tow are individually coated with electrolytic polymer, as illustrated in Figure 5(C). The co-extrusion process using the customized co-axial nozzle, with the help of the drag force of viscous matrix is gentle. The deposition maintains the integrity of delicate thin polymer layer on the carbon fiber filaments, imbedded within cathode material. Thus, each filament act as an individual anode component, their respective polymer coatings act as separator and solid electrolyte, and their combined interaction with surrounding cathode matrix makes the structure into a network of micro-batteries [41], [88].

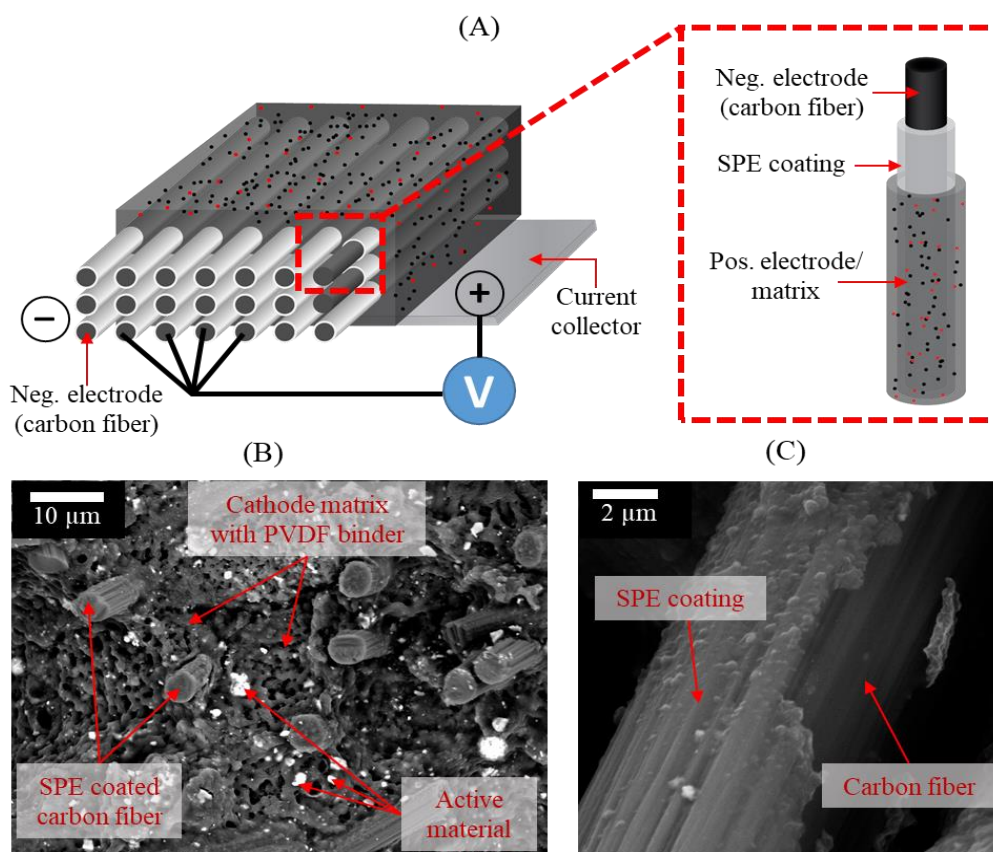


Figure 5. (A) Schematic image of the cross section of the fabricated structural battery composite, and (B) SEM image of the battery composite, with (C) highlighting the SPE coating on the carbon fiber anode embedded within cathode matrix.

## 2.3. TESTING AND CHARACTERIZATION

**2.3.1. Electrochemical Characterization.** The electrochemical performance is generally dictated by the properties of the compositional materials. Ideally, both anode and cathode must have high electrical and ionic conductivity [89]. Electrochemical impedance spectroscopy (EIS) was used to characterize the ionic conductivity, in conjunction with resistivity analyses to characterize electric conductivity for various cathode material composition. For resistivity test, Signatone Pro4-4000 Four Point Resistivity System was used with Keithley 2400 Sourcemeter, and for EIS analyses Gamry Reference 600+ potentiostat was used along with quick assembly split coin cell EQ-HSTC by MTI Corporation. Capacity of the printed battery structures were also measured using Gamry Reference 600+ potentiostat using a direct contact 4-point configuration. Previous studies have already established the efficacy of graphitized PAN-based carbon fibers as anode material [17], [72], [73]. For electrochemical characterization of proposed cathode material composition, the cathode slurry was used to print discs for testing. For battery capacity and Coulombic efficiency measurements, a circular disc shaped concentric battery structure was printed and cured, prior to the testing.

**2.3.2. Mechanical Tests.** Mechanical tests were carried out on the printed structural battery composites to characterize the effects of the composition on the mechanical properties. Tensile test using ASTM D3039 was conducted on five printed samples of each type with specimen geometry of 100 mm × 3 mm × 1 mm. The tensile test setup comprised of an Instron 5881 tester applying tension load at a standard strain rate of 0.01/min until sample failure.

**2.3.3. Microstructural Analyses.** Scanning electron microscopy (SEM), using Quanta 600F Environmental Scanning Electron Microscope, was used to conduct microstructural analyses. SEM was used to investigate the permeability of cathode matrix in reinforcing carbon fiber. To obtain the cross sections of the battery composites, a single layer deposition was first cured and imbedded within VeriDur acrylic resin. It was then sectioned using a slow-speed diamond saw to adequately retain the microstructure within the deposition [90]. The cross-section of each printed battery with varying cathode matrix composition was observed at three different locations, to draw generalized assertions. The observations and subsequent inferences drawn from the SEM examination are detailed in the following sections.

### **3. RESULTS AND DISCUSSION**

#### **3.1. ELECTRICAL CHARACTERIZATION OF CATHODE MATRIX**

For resistivity analyses, the printed electrode discs were analyzed using four-point probe resistivity system. With 43 wt.% LiFePO<sub>4</sub>, 16wt.% Super-P carbon black, 11 wt.% milled short carbon fibers and 25 wt.% PVDF binder the resistivity measured was under 0.4  $\Omega$ .cm. This is over 10 times improvement in electrical conductivity compared to the reported studies using commercial graphene infused PLA pellets [26]. Previous investigations also refrained from adding more than 30 vol. % of conductive material in additively manufactured polymer cathode matrix as it was prone to poor printability and potential clogging [26], [34], [91]. On the other hand, for current set-up, the latency in solvent evaporation and resulting loss in binder serviceability restricts higher

concentrations of carbon black, thus being complemented instead by conductive milled short carbon fibers. Hence, allowing over 70% of the solid load volume to be conductive material. The variation in slurry viscosity through the addition of solvent may vary the electric conductivity of the polymer cathode between 0.2  $\Omega$ .cm and 0.4  $\Omega$ .cm, despite of the consistent solid load composition. This variation may be attributed to the deposition geometry, with lower viscosity leading to a larger surface area for solvent evaporation, affecting the porosity and consequently resistivity of the cured cathode material [69], [70].

Studies have shown noteworthy ionic conductivity through the use of 1 M lithium perchlorate ( $\text{LiClO}_4$ ) in 1:1 (by volume) solution of propylene carbonate (PC) and ethyl methyl carbonate (EMC) solvent combination, providing improved mechanical integrity, better contact with current collectors and higher ionic conductivity retention compared to other lithium salts [26]. For ionic conductivity investigation of the deposited cathode discs, a droplet of the abovementioned liquid electrolyte was added and were investigated with EIS. The ionic conductivity was calculated using following Equation (1).

$$\sigma = \frac{l}{A R_b} \quad (1)$$

where  $l$  is the thickness and is  $A$  the cross-sectional area of the printed disc,  $R_b$  is the bulk resistance which is acquired through the Nyquist plot [92], [93]. The current composition yielded highest ionic conductivity of 11  $\text{mS cm}^{-1}$ , 20 °C. This is higher than previously reported hybrid and polymer electrolytes utilizing  $\text{LiClO}_4$  (0.01–1  $\text{mS cm}^{-1}$ ) suggesting the usability of the proposed cathode composition to be adequate for the structural lithium-ion battery applications [94]–[96].

A similar analysis for resistivity and ionic conductivity variation was carried out for cathode material with varying PVDF binder weight-ratio within the solid load. The results are summarized in the following Figure 6.

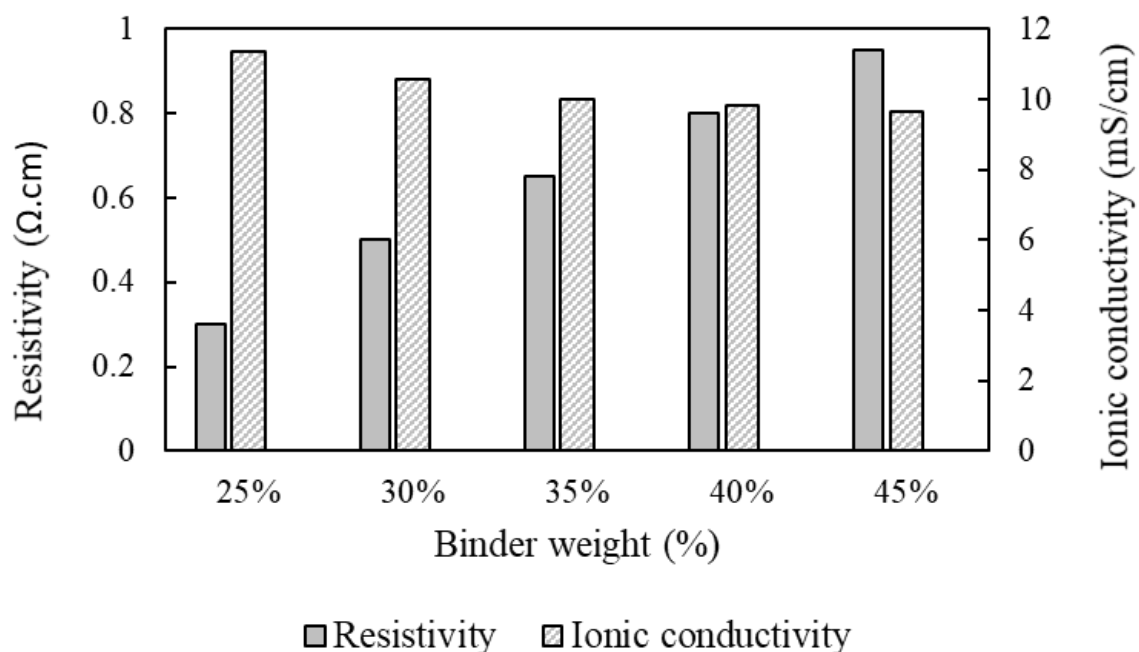


Figure 6. Resistivity and ionic conductivity measured for the cathode material with varying binder weight percent within the solid load.

With increasing binder weight percent within the solid load, the resistivity increased linearly, as expected [71]. Whereas, the ionic conductivity of the cathode material is linearly correlated with the active  $\text{LiFePO}_4$  content. This behavior is different from that of the other solid polymer electrolyte systems, where a maximum conductivity is identified at a particular compositional ratio. This can be associated to the absence of ion-pairing mechanism in PVDF polymer electrolytes [97].

### 3.2. BATTERY PERFORMANCE CHARACTERIZATION

Disc shaped composite battery structures were printed and cured using the proposed additive fabrication process with different cathode slurry compositions. These printed battery composites were used in conjunction with aluminum current collector. A drop of 1 M LiClO<sub>4</sub> in 1:1 (by volume) solution of EMC:PC was added to improve the contact between current collector and the printed battery structure [26]. The set-up was enclosed in a vacuumed pouch bag, inside an Argon purged glovebox. This helped in further improving the contact between the current collector and the energy composite, while also minimizing the corrosion of the aluminum current collector due to atmospheric moisture and oxygen over time, securing robust battery characterization results [13], [98].

To measure the capacity of the printed battery composites, electrochemical performance analyses for full cells was performed using Gamry Reference 600+ potentiostat. The tests were conducted within the cut-off range between 4.5 V and 1 V, electrochemically cycled at *C/5*, within frequency range of 1MHz to 10Hz. The variation in the electrochemical performance with varying cathode slurry viscosity and binder weight percent in the cathode slurry is summarized in the following section.

Throughout the analyses, the battery composites consistently experienced a large irreversible capacity loss, which is attributed to solid electrolyte interphase layer formation [26], [89], [99] and trapped Li within the structure [100]. The electrochemical behavior stabilizes by 10 cycles, as illustrated in Figure 7 where capacities and Coulombic efficiencies of a disc shaped battery is summarized for a 100 – cycle test. Therefore, 10 cycles were selected for comparative quantitative analyses for different cathode compositions, to draw relatively robust inferences within a reasonable timeframe.

Additionally, it was observed that the battery cycling did not deteriorate the lithiation and delithiation process for the proposed energy composite, as observed from the cycling results illustrated in Figure 8.

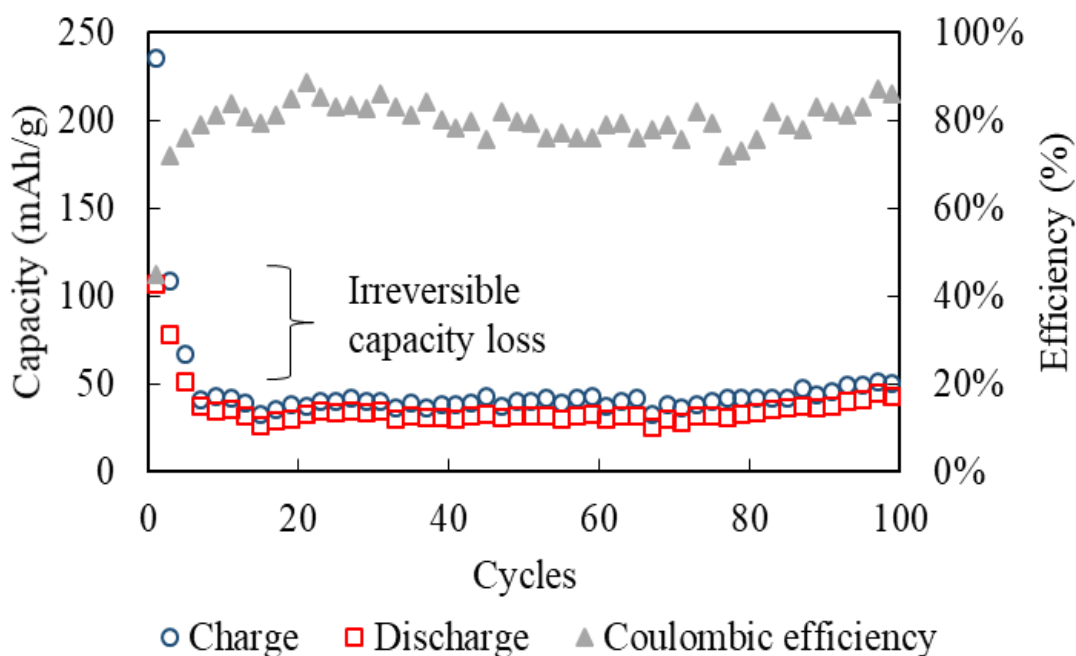


Figure 7. Capacity and Coulombic efficiency at a current density of  $10 \text{ mA g}^{-1}$  for 100 cycles for a disc shaped battery with solid load composition of  $\text{LiFePO}_4$ :Super-P carbon:Milled short carbon fiber:PVDF at 45:12:18:25 ratio. The cathode slurry was prepared with 1:5 volume ratio of solid load:DMF solvent.

### 3.2.1. Effect of Solvent Volume Ratio on the Electrochemical Performance.

Disc shaped battery composites with identical solid load composition, but varying cathode slurry viscosity prior to deposition, were printed and analyzed as the part of this study. The active material weight normalized discharge curves for the 10<sup>th</sup> cycle of the batteries printed with solid load:DMF solvent ratio between 1:3 and 1:5 is illustrated in

the following Figure 9(A). The corresponding discharge capacities are summarized in Figure 9(B).

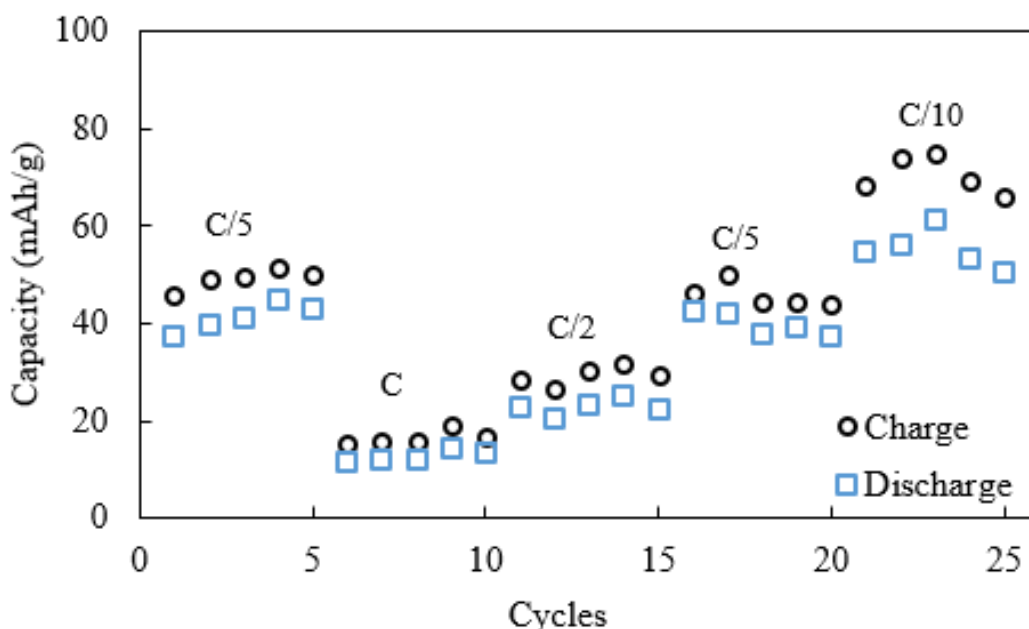


Figure 8. Charging (black circle) and discharging (blue square) capacity of a disc shaped battery with solid load composition of  $\text{LiFePO}_4$ :Super-P carbon:milled short carbon fiber:PVDF at 45:12:18:25 ratio cycled at varying C rates.

For the 10<sup>th</sup> cycle, the normalized discharge capacity for the battery printed with 1:3 volume ratio was measured to be 18 mAh/g (illustrated in solid black in Figure 9(A)). The discharge capacity for the battery printed with 1:4 volume ratio showed a notable increment in comparison with 25 mAh/g (illustrated in solid yellow in Figure 9(A)). The only variation between the two composition being the solid load:DMF solvent ratio. However, this increment in discharge capacity does not increase linearly as further reduction in cathode slurry viscosity to 1:5 volume ratio from 1:4.5 only allowed moderate improvement with 35 mAh/g as discharge capacity, compared to 33 mAh/g. In

summary, the battery composites measure 13%, 15% and 21% utilization of active  $\text{LiFePO}_4$  capacity (with theoretical capacity of 170 mAh/g) for 1:3, 1:4 and 1:5 slurry volume ratios, respectively.

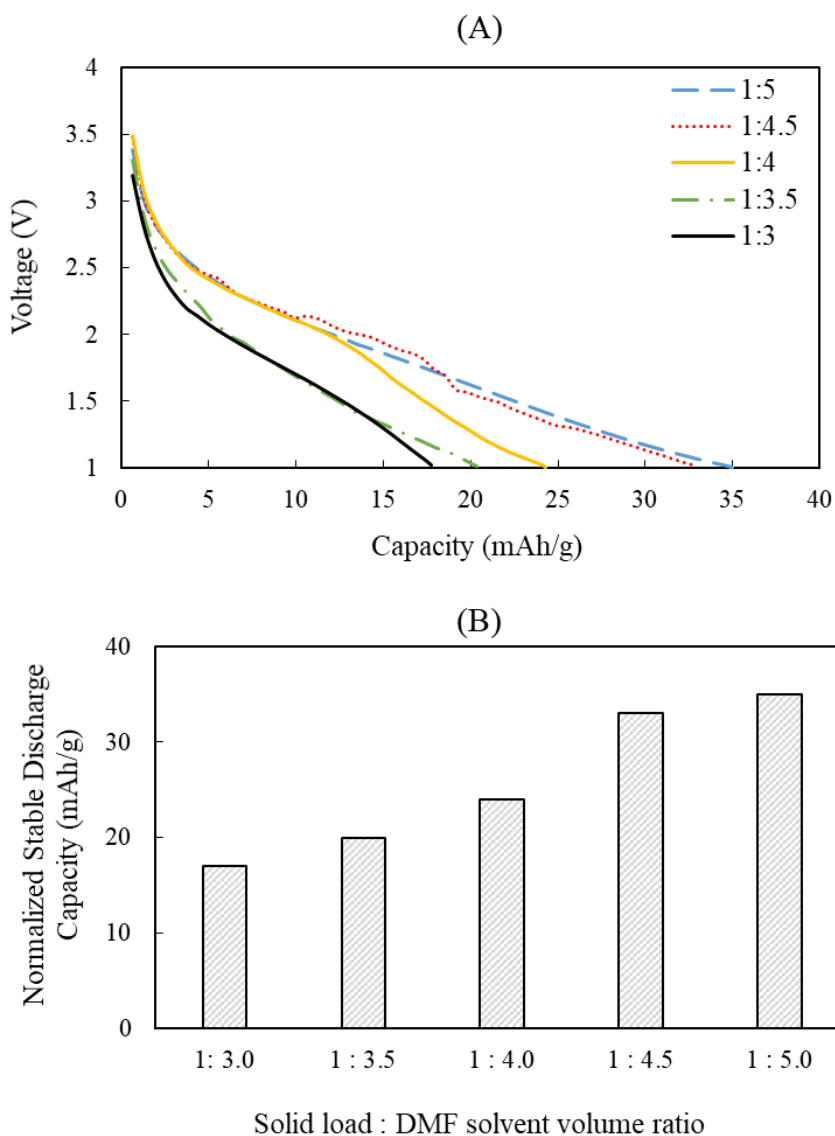


Figure 9. (A) Weight normalized discharge voltage vs. capacity curves of the battery composites printed using cathode slurries with varying viscosities, and (B) the summary of discharge capacities for the battery composites. The solid load composition for cathode slurry is  $\text{LiFePO}_4$ :Super-P carbon:Milled short carbon fiber:PVDF at 45:12:18:25 ratio by weight.

In general, the discharge capacities were notably higher for the battery sample printed with low viscosity slurries. For battery composites with fibrous reinforcing electrode, this can be attributed to the improved impregnation of carbon fibers with cathode slurry matrix, being promoted by lower viscosity prior to curing. This improved permeability of the matrix material within carbon fiber tows enhances integration of fibrous electrodes within the multifunctional battery composites [42]. Improved integration improves contact area between cathode matrix and reinforcing coated carbon fibers, further incentivizing reinforcing carbon fibers to work as a micro-battery cell within the composite, resulting in higher capacities despite of identical solid load composition. However, there is a threshold to the permeability as the increment in the discharge capacity between 1:4.5 and 1:5 solid load:DMF solvent is small, suggesting an upper bound to maximum impregnation, and thus the capacity, using the proposed composition and additive fabrication process.

### **3.2.2. Effect of Binder Weight Percent on the Electrochemical Performance.**

Disc shaped batteries with varying binder weight percent between 25% and 45% were printed and analyzed. The solid load:DMF solvent ratio within the cathode slurry was maintained constant at 1:4.5 for all the samples as it allowed improved printability. The active  $\text{LiFePO}_4$  weight normalized discharge curves procured for the 10<sup>th</sup> cycle for batteries printed with 25% to 45% binder weight percent is illustrated in following Figure 10(A), and the discharge capacities are summarized in Figure 10(B).

For the 10<sup>th</sup> cycle, the normalized discharge capacity for the battery printed with 25% binder was measured to be 33 mAh/g (illustrated in dotted red in Figure 10(A)). With the increase in the binder weight percent, there was a decrease in the discharge

capacity. However, the decreasing trend was not linear as observed for the increment in resistivity and decrease in ionic conductivity, as noted in Figure 6, for cathode matrix with varying binder weight percent. The discharge capacity for 30% and 35% binder (illustrated in solid yellow and dashed green in Figure 10(A), respectively) is nearly comparable, with significant drop in capacity for the following samples with 40% and 45% binder (illustrated in dashed blue and solid black in Figure 10(A), respectively), measuring just 20 mAh/g and 14 mAh/g.

With increment in the viscosity with the increase in binder weight percent, as illustrated in Figure 1(B), the impregnation of the cathode slurry is compromised at higher binder weight percentages. This in turn could reduce the contact area between the cathode matrix and the reinforcing coated carbon fibers due to the presence of large voids, rendering the carbon fibers to have a reduced contact area with the cathode matrix. This, makes them incapable of efficiently contributing as micro-battery cells within the composite, resulting in lowered capacities than expected. The increase in the binder weight percent, reduces the pores and improves the contact between the reinforcing fiber anode and cathode matrix. However, in the absence of microspores, the diffusion path of the lithium-ions may lengthen. Thus, negatively affecting the Li mobility and impacting the electrochemical performance of the printed structures.

### **3.3. CARBON FIBER CONTENT**

The carbon fiber content is one of the main factors determining the mechanical properties of the printed fiber-reinforced composites. It is typically represented by the carbon fiber volume fraction  $V_f$  as calculated by

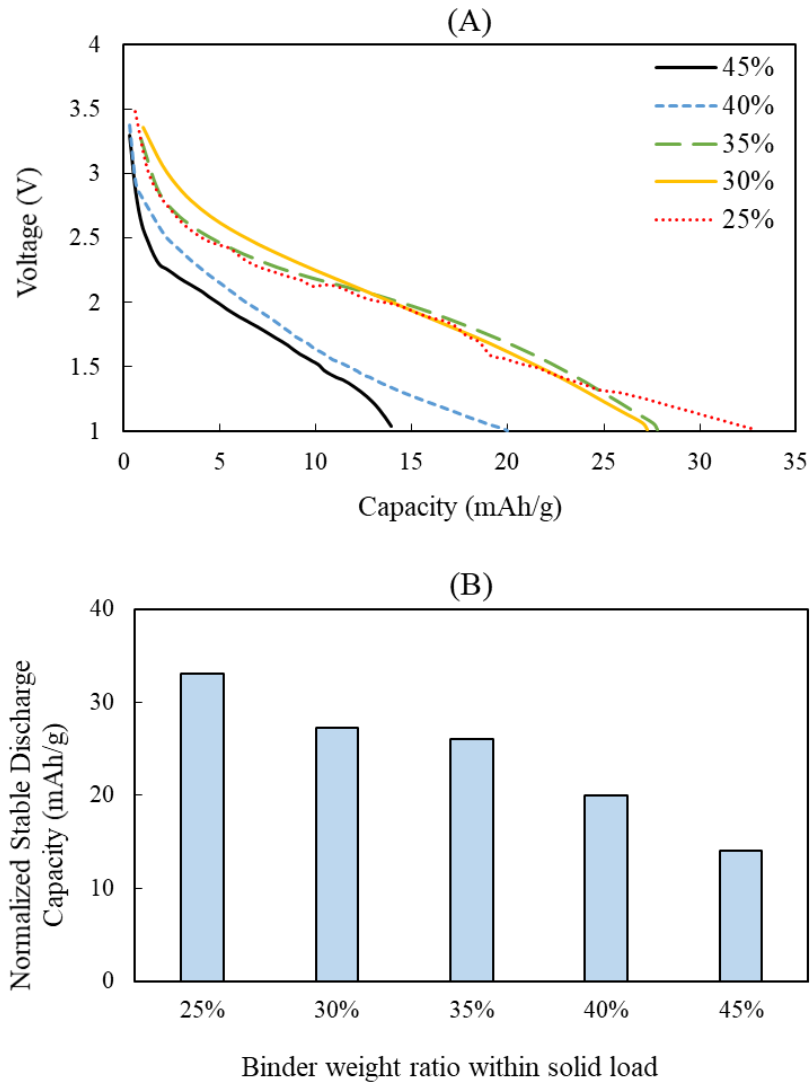


Figure 10. (A) Weight normalized discharge voltage vs. capacity curves of the battery composites printed using cathode slurries with varying binder weight percent, and (B) the summary of discharge capacities for the battery composites.

$$V_f = \frac{W_f}{\rho_f} \left( \frac{1}{\frac{W_f}{\rho_f} + \frac{W_m}{\rho_m}} \right) \quad (2)$$

where  $W_f$  and  $W_m$  represent the weights of fiber reinforcement and the matrix material, respectively. In this study the densities of continuous carbon fiber reinforcement ( $\rho_f$ )

was taken as  $1.81 \text{ g/cm}^3$ , from the selected carbon fiber tows (Toray T800HB) [101]. For the matrix material, the densities for each individual material within the solid load was considered for the measurement for varying compositions with PVDF as  $1.78 \text{ g/cm}^3$  [102], carbon black as  $0.16 \text{ g/cm}^3$  [103], short carbon fiber with measured tapped density of  $0.275 \text{ g/cm}^3$ , and  $\text{LiFePO}_4$  as  $1.1 \text{ g/cm}^3$  [104]. In printing energy composite samples, SPE coated continuous carbon fibers were coextruded with the cathode slurry. The carbon fiber length can be obtained from the length of nozzle path, and the carbon fiber weight ( $W_f$ ) can then be calculated by multiplying its weight per unit length with the carbon fiber length. After the weight of extruded cathode matrix material ( $W_m$ ) was measured, the continuous carbon fiber volume fraction was calculated from Equation (2).

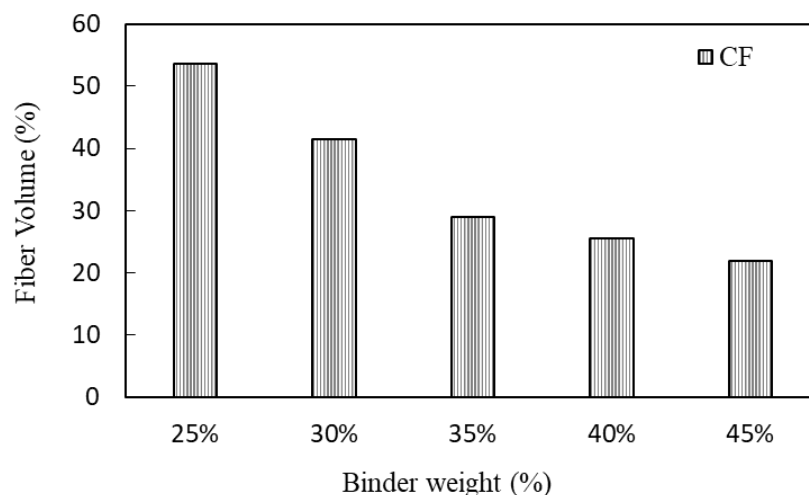


Figure 11. Continuous fiber volume fraction for varying binder weight percent of solid load within the cathode matrix.

The obtained carbon fiber content with respect to binder weight percent is illustrated in Figure 11. At a fixed deposition length, the fiber volume percent of the

reinforcing continuous fiber decreased within the composite with increasing binder weight percent. This was mainly attributed to the deposition comprising of larger volume fraction of solid load extruded with increased binder content, thus yielding lower carbon fiber content within the printed composite and hence a lower fiber volume fraction. A maximum fiber volume fraction of 53% was obtained within the composite with 25% PVDF binder in its cathode matrix, whereas minimum fiber volume fraction of 22% was obtained within the composite with 45% PVDF binder in its cathode matrix.

### **3.4. MECHANICAL PERFORMANCE**

The effect of variation in cathode slurry composition and viscosity on the mechanical properties of the printed battery composite was investigated through the tensile testing. Three specimens for each parametric combination were subjected to tension test, to measure the strength and the modulus of the sample. The following Figure 12 summarizes the measured tensile strength and modulus for the samples printed with varying cathode slurry viscosity, and Figure 13 summarizes it for the samples printed with varying binder percent.

A consistent increase in tensile strength and modulus was observed for the samples printed with identical cathode slurry composition, albeit with varying cathode slurry viscosity through the addition of DMF solvent, as observed in Figure 12(A). With 1:3 solid load:DMF solvent ratio, the average tensile strength and the modulus was measured to be 380 MPa and 52 GPa, respectively. While, the sample printed with 1:5 solid load:DMF solvent ratio demonstrated over 100% increase in tensile strength and nearly 41% increase in modulus.

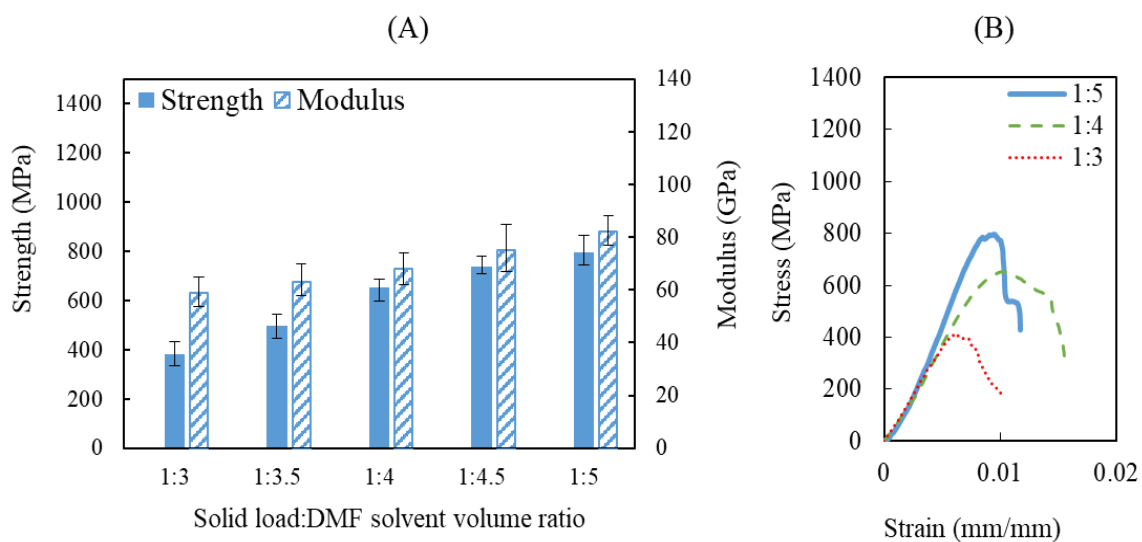


Figure 12. (A) Measured tensile strength and modulus, and (B) stress vs. strain curve for the battery composites with varying solid load:DMF solvent volume ratio with solid load composition of  $\text{LiFePO}_4$ :Super-P carbon:Milled short carbon fiber:PVDF at 45:12:18:25 ratio by weight.

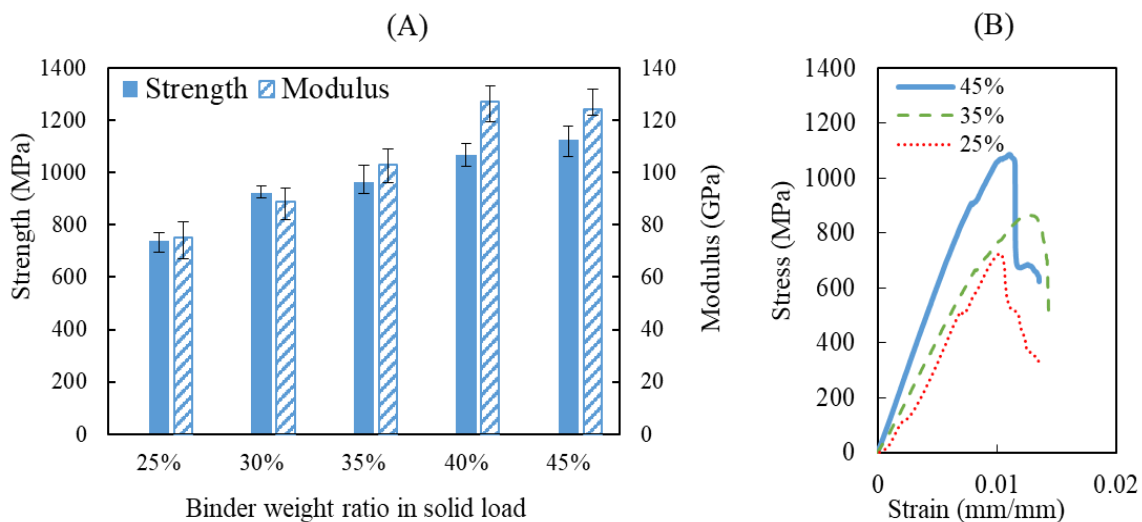


Figure 13. (A) Measured tensile strength and modulus, and (B) stress vs. strain curve for the battery composites with varying binder weight percent in the solid load with solvent volume ratio of 1:4.5.

It is noteworthy that the matrix composition only comprises of 25 wt.% of PVDF as binder in these samples. Thus, the strength of the cured cathode matrix is lowered to 7 MPa in comparison to ~ 35 MPa for pure PVDF polymer, while the modulus is reduced to 27 MPa from 1.3 GPa [102]. The continuous reinforcing fibers, as reported by the vendor, have strength and modulus of 5490 MPa and 294 GPa, respectively [101]. Clearly, the reinforcing fibers play a significant role in imparting the tensile strength to the printed battery composites. The variation in the fiber impregnation due to the viscosity modification is notable. Moreover, the incremental strength with the increase in solvent volume, within the cathode slurry prior to printing, suggests that the permeability of the matrix material is significantly controlled by the viscosity of the cathode slurry as the continuous fiber volume fraction remains consistent at 53%. Improvement in the fiber impregnation directly correlates with improved bonding and interface between the fibers and the matrix, and subsequent reduction in voids within the printed composites [48], [105]. Thus, cathode slurries with lower viscosities impart higher strength to the composite upon curing. This assertion was further substantiated through the microstructural analyses.

It is obvious that the mechanical behavior of the matrix material increases with the increment in the binder weight percent within the solid load. Thus, there is an expectation for increment in the tensile strength and the modulus of the samples printed with the increased binder percent, as illustrated in Figure 13. However, this measured improvement in the mechanical performance is not collinear as the samples over 35% of binder demonstrated almost comparable mechanical behavior, despite of obvious increase in the mechanical strength of the cathode matrix. For example, samples printed with 40%

and 45% binder measured an average over 1000 MPa of mechanical strength and approximate modulus of 125 GPa.

This could be attributed to the hampered permeability due to the increased viscosity with increment in binder weight percent, as illustrated in Figure 1(B), and reduced continuous fiber volume fraction within the composite with increasing binder volume fraction as illustrated in Figure 11. The reduced permeability leads to an increased void fraction within the fiber reinforced samples for slurry composition with a given solid load:DMF solvent ratio. Thus, the resulting battery composites have larger total porous area, despite reduced tendency to form micro-pores. Increasing the percentage of solvent would help decrease viscosity and improve fiber-matrix bonding as discussed above.

## **4. MICROSTRUCTURAL ANALYSES**

### **4.1. POROSITY ANALYSES**

The pore size measurement and distribution analyses for the battery composites with varying cathode slurry compositions was done via the microstructural characterization carried out using the SEM images acquired for the cross sections of the depositions. SEM images of the overall composite deposition imbedded within VeriDur acrylic resin were acquired to observe and measure larger voids, while the images at higher magnification were acquired to observe and measure the micro-pores. Three separate locations within each composite were studied under SEM, which provided the uncertainties in the porosity observed within each composition. The examples of this are

illustrated in Figure 14 for samples with varying cathode slurry viscosity, and in Figure 15 for samples with varying binder percent within the cathode slurry.

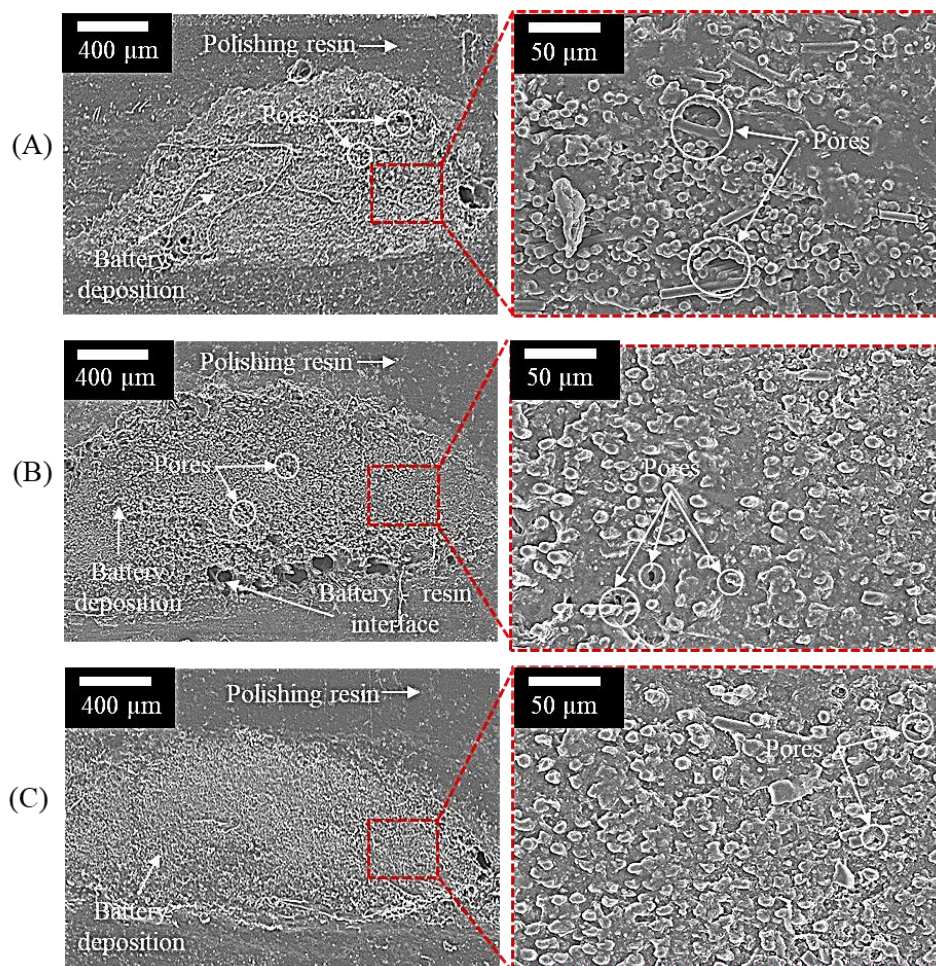


Figure 14. SEM images illustrating the overall deposition and an inset image providing an example of magnified view for the battery composite samples with varying viscosity of (A) 1:3, (B) 1:4 and (C) 1:5 solid load:DMF solvent ratio.

It is noteworthy that the obvious large voids around the periphery of the deposition are caused due to the interface between the depositions and the VeriDur acrylic resin, as specifically pointed out in Figure 14(B) and Figure 15(C). This was used to secure the sample while cutting across the cross sections. These artifacts are not an

inherent part of deposition and thus have been ignored in the calculation of total porosity area as illustrated in Figure 16, and distribution as summarized in Figure 17.

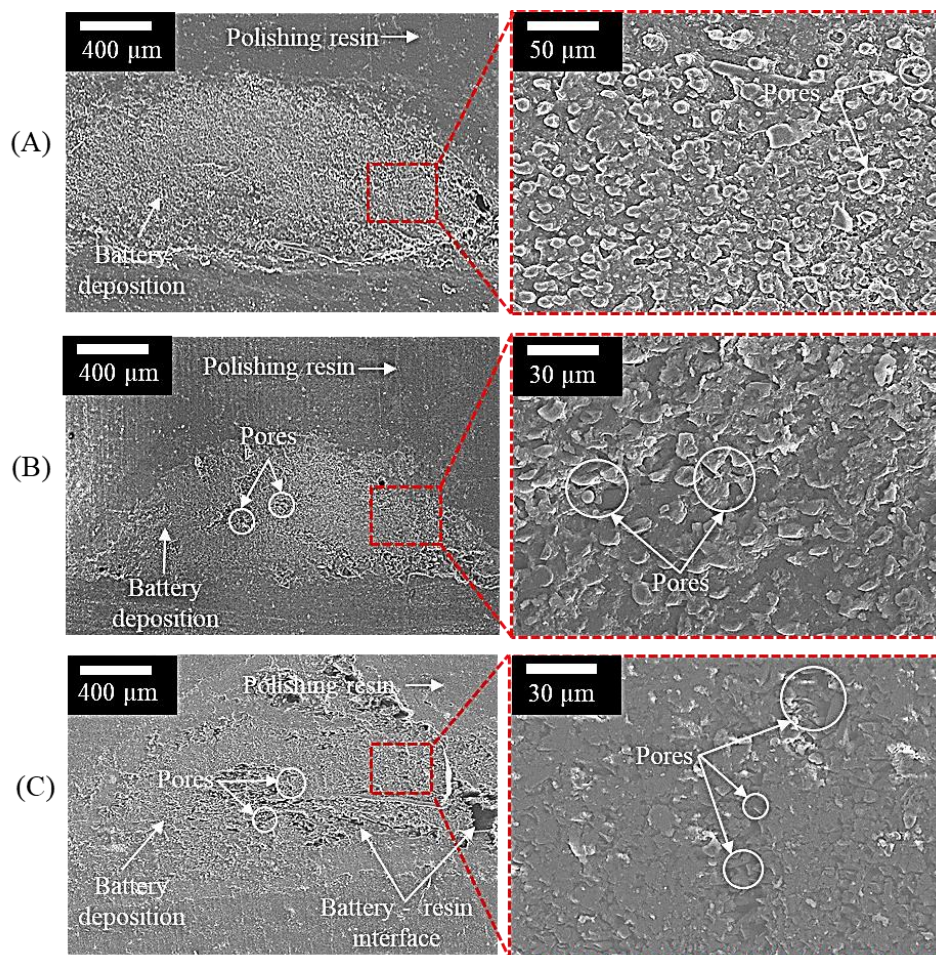


Figure 15. SEM images illustrating the overall deposition and inset image providing an example magnified view for the battery composite samples with varying binder percent of (A) 25%, (B) 35%, and (C) 45% within the solid load of the cathode slurry.

Associating Figure 16 with the viscosity analyses from Figure 1(A) and Figure 1(B), it is apparent that the total porosity within the deposition correlates with the resulting viscosity of the cathode slurry. However, upon closer inspection, observing weighted histogram based on the equivalent circular area diameter distribution, as

illustrated in Figure 17, it is possible to correlate the pore size distribution with the amount of binder in the cathode slurry and its permeability within the coated carbon fibers.

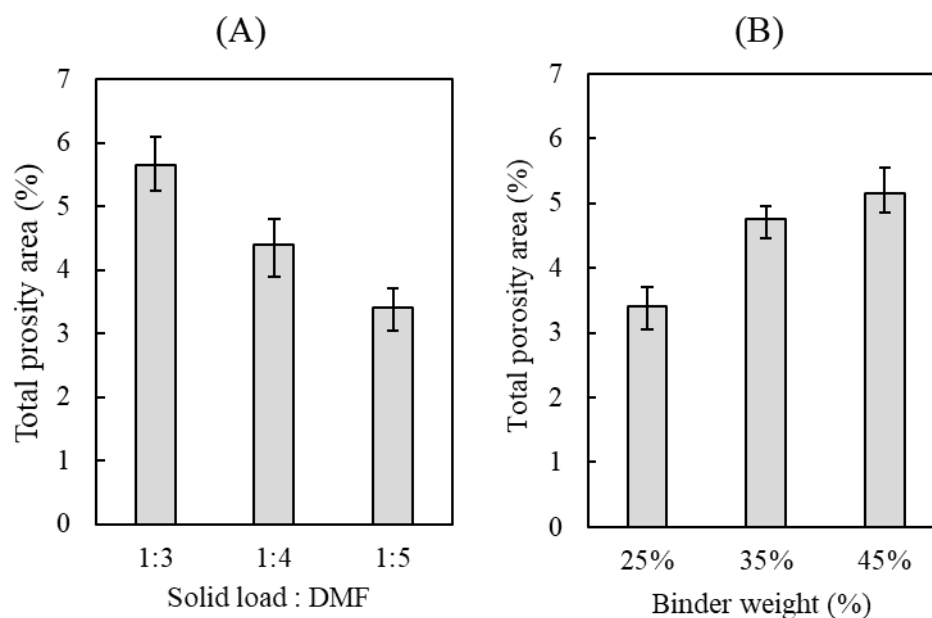


Figure 16. Comparison of the total porosity area within the battery composite deposition for (A) varying viscosity with solid load composition containing 25% binder by weight, and (B) varying binder percentage at fixed solvent volume ratio of 1:4.5.

From Figure 17(A) and Figure 17(B), it is apparent that for the samples printed with cathode slurry having lowest viscosities (solid black bar in Figure 17(A) and solid gray bar in Figure 17(B)), there is a complete absence of voids exceeding equivalent circular diameter of 10  $\mu\text{m}$ . On the other hand, smaller pores of < 5  $\mu\text{m}$  are predominantly present across all the samples; occupying almost same area within the deposition in the samples with identical cathode slurry composition, as illustrated in Figure 17(A).

The small pore occupation of the area within the deposition decreases with increasing binder percent, as illustrated in Figure 17(B). The amount of binder within the cathode slurry also controls the presence of the smaller pores ( $< 10 \mu\text{m}$ ) within the polymerized cathode matrix for current composition, with increase in binder percent correlating with the decrease in the presence of smaller pores. On the other hand, the permeability of the cathode slurry in the reinforcing fiber anode, is largely dictated by the viscosity of the cathode slurry and has a profound effect on the presence of larger pores.

This helps in explaining the observations made through the electrochemical and mechanical analyses. For example, sample printed with 45% binder has a higher tendency to have prominent voids within the deposition. This is due to lower permeability which is a result of increased cathode slurry viscosity. Additionally, the same sample has reduced likelihood to form micro-pores during polymerization, thus, impeding lithium-ion mobility. Thus, negatively affecting the electrochemical performance of the sample. This helps explain why the sample printed with 45 % binder has the lowest battery capacity amongst the studied compositions, as observed in Figure 10 (A), besides a lower loadings of active and conductive materials.

This microstructural characteristic also negatively effects the mechanical performance of the printed battery composite, with minimal improvement in its strength or modulus for the sample with 45% binder, compared to the samples with 40% binder, in spite of having mechanically superior cathode with higher binder weight percentage within the solid load, as observed in Figure 12(B). On the other hand, sample printed with 1:5 solid load:DMF solvent ratio with just 25% binder exhibits highest mechanical strength compared to samples with identical solid load composition.

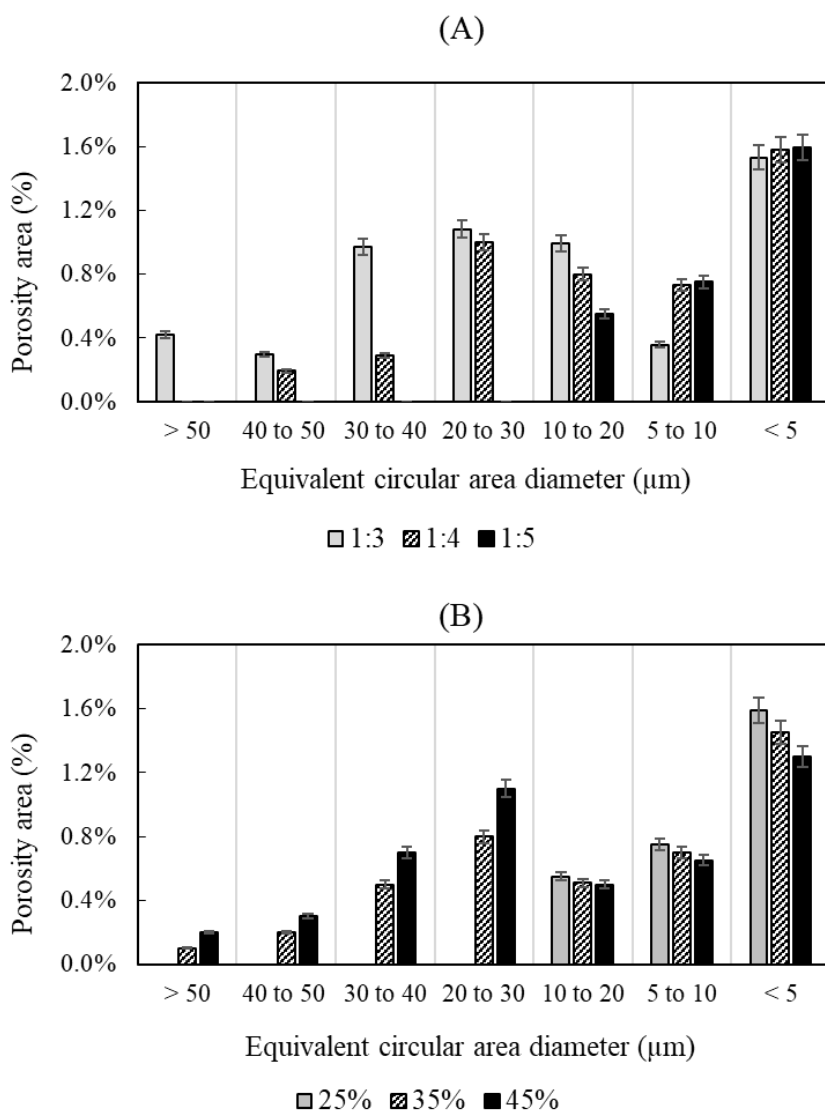


Figure 17. Weighted histogram illustrating average changes in pore size distribution within the battery composite deposition for samples with (A) varying viscosity with solid load composition containing 25% binder by weight, and (B) varying binder percentage at fixed solvent volume ratio of 1:4.5.

At the same time, it also measures highest discharge capacity. Based on the microstructural analyses and the conclusions thus drawn, with improved permeability, this cathode slurry composition yields a relatively high mechanical and electrochemical performance for a given solid load composition, just by moderating the viscosity of the

slurry prior to deposition. Therefore, it can be concluded that while additively fabricating a fiber reinforced structural battery composite, through apt modulation of viscosity of the cathode slurry and the binder weight percent within it, it is possible to optimize the electrochemical and mechanical performance of the resulting multifunctional composite.

## 5. CONCLUSIONS

This paper demonstrates coextrusion based additive manufacturing approach to 3D print functional structural battery using energy composites. Presence of continuous carbon fiber anode embedded within fluoropolymer thermoplastic PVDF cathode acts as a reinforcement improving the mechanical characteristics of inherently weaker PVDF polymer electrode structure. Extrusion based deposition technique allows higher amount of active and conductive fillers being added to the thermoplastic cathode with minimal binder volume. This helps in imbuing multifunctionality within the composites without negatively affecting their printability. The viscosity moderation via solvents assists in improving the permeability of cathode material within the coated carbon fiber bundles, dramatically improving the surface contact between battery components. This helps in thorough integration of coated carbon fiber anode with solid polymer electrolyte and separator within cathode matrix, where each individual carbon fiber can directly act as one battery electrode and current collector. The proposed fabrication process enables additive fabrication via coextrusion deposition of net-shaped, full lithium-ion structural batteries, as illustrated in Figure 18 by printing and assembling (A) disc-shaped, (B)

triangular shaped and (C) square shaped battery composites to light up LEDs. The practical usability of these battery composite was demonstrated by using the 3D printed disc-shaped battery to power a digital caliper. This first-generation, 3D printed structural battery with conductive fiber anode, illustrates capacities notably higher than previously reported attempts at 3D printed lithium-ion batteries.

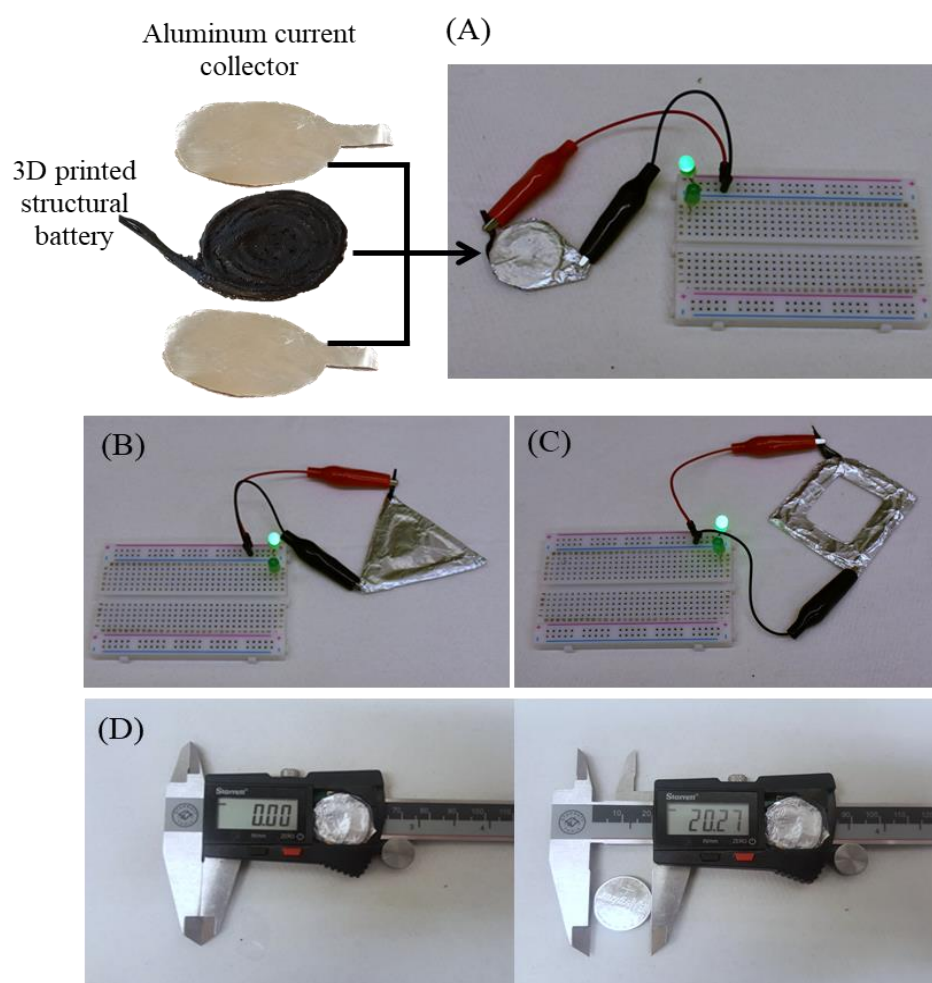


Figure 18. (A) Printed disc-shaped structural battery composite assembled with aluminum current collector, illuminating LED, along with (B) triangular and (C) square shaped 3D batteries illustrating the capability of the proposed fabrication process. (D) The disc-shaped structural battery composite being used as a replacement for CR2032 lithium coin cell battery.

## REFERENCES

- [1] B. Fleming, “An Overview of Advances in Automotive Electronics [Automotive Electronics],” *IEEE Veh. Technol. Mag.*, vol. 9, no. 1, pp. 4–9, Mar. 2014.
- [2] J. P. Thomas and M. A. Qidwai, “The design and application of multifunctional structure-battery materials systems,” *JOM*, vol. 57, no. 3, pp. 18–24, Mar. 2005.
- [3] N. Singh *et al.*, “Paintable Battery,” *Sci. Rep.*, vol. 2, p. 481, Jun. 2012.
- [4] NatureWorks, “Crystallizing and Drying of PLA,” *Technical Resources*, 2007. [Online]. Available: <http://www.natureworkslc.com/Technical-Resources/4-Series.aspx>. [Accessed: 13-Oct-2020].
- [5] B. Moore, T. Jaglinski, D. S. Stone, and R. S. Lakes, “Negative incremental bulk modulus in foams,” *Philos. Mag. Lett.*, vol. 86, no. 10, pp. 651–659, 2006.
- [6] N. Shirshova *et al.*, “Structural composite supercapacitors,” *Compos. Part A Appl. Sci. Manuf.*, vol. 46, pp. 96–107, Mar. 2013.
- [7] Q. Chen, R. Xu, Z. He, K. Zhao, and L. Pan, “Printing 3D Gel Polymer Electrolyte in Lithium-Ion Microbattery Using Stereolithography,” *J. Electrochem. Soc.*, vol. 164, no. 9, pp. A1852–A1857, 2017.
- [8] B. Grzesik *et al.*, “Integration of energy storage functionalities into fiber reinforced spacecraft structures,” *Acta Astronaut.*, vol. 166, pp. 172–179, 2020.
- [9] E. L. Wong, D. M. Baechle, K. Xu, R. H. Carter, J. F. Snyder, and E. D. Wetzel, “Design and processing of structural composite batteries,” in *International SAMPE Symposium and Exhibition (Proceedings)*, 2007, pp. 1–20.
- [10] E. Senokos *et al.*, “Energy storage in structural composites by introducing CNT fiber/polymer electrolyte interleaves,” *Sci. Rep.*, vol. 8, no. 1, p. 3407, Dec. 2018.
- [11] L. E. Asp and E. S. Greenhalgh, “Structural power composites,” *Compos. Sci. Technol.*, vol. 101, pp. 41–61, Sep. 2014.
- [12] L. E. Asp, M. Johansson, G. Lindbergh, J. Xu, and D. Zenkert, “Structural battery composites: a review,” *Funct. Compos. Struct.*, vol. 1, no. 4, pp. 1–19, 2019.
- [13] W. Johannisson *et al.*, “Multifunctional performance of a carbon fiber UD lamina electrode for structural batteries,” *Compos. Sci. Technol.*, vol. 168, pp. 81–87, Nov. 2018.

- [14] A. Lendlein and R. S. Trask, "Multifunctional materials: concepts, function-structure relationships, knowledge-based design, translational materials research," *Multifunct. Mater.*, vol. 1, no. 1, p. 010201, Aug. 2018.
- [15] P. Liu, E. Sherman, and A. Jacobsen, "Design and fabrication of multifunctional structural batteries," *J. Power Sources*, vol. 189, no. 1, pp. 646–650, 2009.
- [16] Y. Yu *et al.*, "Multifunctional structural lithium ion batteries based on carbon fiber reinforced plastic composites," *Compos. Sci. Technol.*, vol. 147, pp. 62–70, 2017.
- [17] M. H. Kjell, E. Jacques, D. Zenkert, M. Behm, and G. Lindbergh, "PAN-Based Carbon Fiber Negative Electrodes for Structural Lithium-Ion Batteries," *J. Electrochem. Soc.*, vol. 158, no. 12, p. A1455, 2011.
- [18] S. Ekstedt, M. Wysocki, and L. E. Asp, "Structural batteries made from fibre reinforced composites," *Plast. Rubber Compos.*, vol. 39, no. 3–5, pp. 148–150, Jun. 2010.
- [19] J. W. Fergus, "Ceramic and polymeric solid electrolytes for lithium-ion batteries," *J. Power Sources*, vol. 195(15), pp. 4554–4569, 2010. <https://doi.org/10.1016/j.jpowsour.2010.01.076>, *J. Power Sources*, 2010.
- [20] J. F. Snyder, E. D. Wetzel, and C. M. Watson, "Improving multifunctional behavior in structural electrolytes through copolymerization of structure- and conductivity-promoting monomers," *Polymer (Guildf.)*, vol. 50, no. 23, pp. 4906–4916, 2009.
- [21] B. K. Deka, A. Hazarika, J. Kim, Y. Bin Park, and H. W. Park, "Recent development and challenges of multifunctional structural supercapacitors for automotive industries," *Int. J. Energy Res.*, vol. 41, no. 10, pp. 1397–1411, 2017.
- [22] S. H. Kim, K. H. Choi, S. J. Cho, S. Choi, S. Park, and S. Y. Lee, "Printable Solid-State Lithium-Ion Batteries: A New Route toward Shape-Conformable Power Sources with Aesthetic Versatility for Flexible Electronics," *Nano Lett.*, vol. 15, pp. 5168–5177, 2015.
- [23] L. Hu, H. Wu, F. La Mantia, Y. Yang, and Y. Cui, "Thin, flexible secondary Li-ion paper batteries," *ACS Nano*, vol. 4, no. 10, pp. 5843–5848, 2010.
- [24] J. Ren *et al.*, "Elastic and wearable wire-shaped lithium-ion battery with high electrochemical performance," *Angew. Chemie - Int. Ed.*, vol. 53, no. 30, pp. 7864–7869, 2014.

- [25] A. J. Blake *et al.*, “3D Printable Ceramic–Polymer Electrolytes for Flexible High-Performance Li-Ion Batteries with Enhanced Thermal Stability,” *Adv. Energy Mater.*, vol. 7, no. 14, pp. 1–10, 2017.
- [26] C. Reyes *et al.*, “Three-Dimensional Printing of a Complete Lithium Ion Battery with Fused Filament Fabrication,” *ACS Appl. Energy Mater.*, vol. 1, no. 10, p. acaem.8b00885, Oct. 2018.
- [27] E. H. Kil *et al.*, “Imprintable, bendable, and shape-conformable polymer electrolytes for versatile-shaped lithium-ion batteries,” *Adv. Mater.*, vol. 25, pp. 1395–1400, 2013.
- [28] K. K. Sairajan, G. S. Aglietti, and K. M. Mani, “A review of multifunctional structure technology for aerospace applications,” *Acta Astronautica*. 2016.
- [29] C. W. Schwingshackl, G. S. Aglietti, and P. R. Cunningham, “Experimental determination of the dynamic behavior of a multifunctional power structure,” *AIAA J.*, vol. 45, no. 2, pp. 491–496, 2007.
- [30] A. D. B. L. Ferreira, P. R. O. Nóvoa, and A. T. Marques, “Multifunctional Material Systems: A state-of-the-art review,” *Compos. Struct.*, vol. 151, pp. 3–35, 2016.
- [31] J. Li, M. C. Leu, R. Panat, and J. Park, “A hybrid three-dimensionally structured electrode for lithium-ion batteries via 3D printing,” *Mater. Des.*, vol. 119, no. 5, pp. 417–424, 2017.
- [32] R. D. Farahani *et al.*, “Direct-write fabrication of freestanding nanocomposite strain sensors,” *Nanotechnology*, vol. 23, no. 8, p. 085502, Mar. 2012.
- [33] C.-W. Wang, K. A. Cook, and A. M. Sastry, “Conduction in Multiphase Particulate/Fibrous Networks,” *J. Electrochem. Soc.*, vol. 150, no. 3, pp. 385–397, 2003.
- [34] A. Thakur and X. Dong, “Printing with 3D continuous carbon fiber multifunctional composites via UV-assisted coextrusion deposition,” *Manuf. Lett.*, vol. 24, pp. 1–5, Apr. 2020.
- [35] E. Jacques, M. H. Kjell, D. Zenkert, and G. Lindbergh, “The effect of lithium-intercalation on the mechanical properties of carbon fibres,” *Carbon N. Y.*, vol. 68, pp. 725–733, Mar. 2014.
- [36] J. Hagberg *et al.*, “Lithium iron phosphate coated carbon fiber electrodes for structural lithium ion batteries,” *Compos. Sci. Technol.*, vol. 162, pp. 235–243, 2018.

- [37] G. Fredi *et al.*, “Graphitic microstructure and performance of carbon fibre Li-ion structural battery electrodes,” *Multifunct. Mater.*, vol. 1, no. 1, pp. 1–6, 2018.
- [38] E. Jacques, M. H. Kjell, D. Zenkert, and G. Lindbergh, “Piezo-electrochemical effect in lithium-intercalated carbon fibres,” *Electrochem. commun.*, vol. 35, pp. 65–67, 2013.
- [39] S. K. Martha, N. J. Dudney, J. O. Kiggans, and J. Nanda, “Electrochemical Stability of Carbon Fibers Compared to Aluminum as Current Collectors for Lithium-Ion Batteries,” *J. Electrochem. Soc.*, vol. 159, no. 10, pp. 1652–1658, 2012.
- [40] N. Shirshova *et al.*, “Multifunctional structural energy storage composite supercapacitors,” *Faraday Discuss.*, vol. 172, pp. 81–103, 2014.
- [41] T. Carlson, “Multifunctional Composite: Materials Design, Manufacture and Experimental Characterisation,” Luleå University of Technology, 2013.
- [42] E. B. K. Neudecker B. J. Benson M.H., “Power Fibers: Thin-Film Batteries On Fiber Substrates,” in *Proceedings of the 14th International Conference on Composite Materials (ICCM 14). San Diego, CA*, 2003.
- [43] K. Moyer, N. A. Boucherbil, M. Zohair, J. Eaves-Rathert, and C. L. Pint, “Polymer reinforced carbon fiber interfaces for high energy density structural lithium-ion batteries,” *Sustain. Energy Fuels*, 2020.
- [44] K. Moyer *et al.*, “Carbon fiber reinforced structural lithium-ion battery composite: Multifunctional power integration for CubeSats,” *Energy Storage Mater.*, 2020.
- [45] N. Li, Y. Li, and S. Liu, “Rapid prototyping of continuous carbon fiber reinforced polylactic acid composites by 3D printing,” *J. Mater. Process. Technol.*, vol. 238, pp. 218–225, Dec. 2016.
- [46] X. Yao, C. Luan, D. Zhang, L. Lan, and J. Fu, “Evaluation of carbon fiber-embedded 3D printed structures for strengthening and structural-health monitoring,” *Mater. Des.*, vol. 114, pp. 424–432, Jan. 2017.
- [47] X. Tian, T. Liu, C. Yang, Q. Wang, and D. Li, “Interface and performance of 3D printed continuous carbon fiber reinforced PLA composites,” *Compos. Part A Appl. Sci. Manuf.*, vol. 88, pp. 198–205, Sep. 2016.
- [48] R. Matsuzaki *et al.*, “Three-dimensional printing of continuous-fiber composites by in-nozzle impregnation,” *Sci. Rep.*, vol. 6, no. 1, p. 23058, Sep. 2016.

- [49] T. A. Dutra, R. T. L. Ferreira, H. B. Resende, and A. Guimarães, "Mechanical characterization and asymptotic homogenization of 3D-printed continuous carbon fiber-reinforced thermoplastic," *J. Brazilian Soc. Mech. Sci. Eng.*, vol. 41, no. 3, p. 133, Mar. 2019.
- [50] M. Heidari-Rarani, M. Rafiee-Afarani, and A. M. Zahedi, "Mechanical characterization of FDM 3D printing of continuous carbon fiber reinforced PLA composites," *Compos. Part B Eng.*, vol. 175, p. 107147, 2019.
- [51] P. Parandoush, C. Zhou, and D. Lin, "3D Printing of Ultrahigh Strength Continuous Carbon Fiber Composites," *Adv. Eng. Mater.*, vol. 21, no. 2, pp. 1–8, 2019.
- [52] A. Todoroki *et al.*, "Tensile property evaluations of 3D printed continuous carbon fiber reinforced thermoplastic composites," *Adv. Compos. Mater.*, vol. 29, no. 2, pp. 147–162, 2020.
- [53] M. Ueda *et al.*, "3D compaction printing of a continuous carbon fiber reinforced thermoplastic," *Compos. Part A Appl. Sci. Manuf.*, vol. 137, p. 105985, 2020.
- [54] M. Zhang *et al.*, "Printable Smart Pattern for Multifunctional Energy-Management E-Textile," *Matter*, vol. 1, no. 1, pp. 168–179, Jul. 2019.
- [55] J. Peng *et al.*, "3D extruded composite thermoelectric threads for flexible energy harvesting," *Nat. Commun.*, vol. 10, no. 1, p. 5590, Dec. 2019.
- [56] A. Lund, K. Rundqvist, E. Nilsson, L. Yu, B. Hagström, and C. Müller, "Energy harvesting textiles for a rainy day: woven piezoelectrics based on melt-spun PVDF microfibrils with a conducting core," *npj Flex. Electron.*, vol. 2, no. 1, p. 9, Dec. 2018.
- [57] Y. Abe, N. Hori, and S. Kumagai, "Electrochemical Impedance Spectroscopy on the Performance Degradation of LiFePO<sub>4</sub>/Graphite Lithium-Ion Battery Due to Charge-Discharge Cycling under Different C-Rates," *Energies*, vol. 12, no. 23, p. 4507, Nov. 2019.
- [58] S. Sarkar and S. Mitra, "Carbon coated submicron sized-LiFePO<sub>4</sub>: Improved high rate performance lithium battery cathode," *Energy Procedia*, vol. 54, pp. 718–724, 2014.
- [59] C. Su, X. Bu, L. Xu, J. Liu, and C. Zhang, "A novel LiFePO<sub>4</sub>/graphene/carbon composite as a performance-improved cathode material for lithium-ion batteries," *Electrochim. Acta*, vol. 64, pp. 190–195, 2012.
- [60] Z. Zhang *et al.*, "Cycle performance improvement of LiFePO<sub>4</sub> cathode with polyacrylic acid as binder," *Electrochim. Acta*, vol. 80, pp. 440–444, 2012.

- [61] H. Shobukawa, J. Alvarado, Y. Yang, and Y. S. Meng, "Electrochemical performance and interfacial investigation on Si composite anode for lithium ion batteries in full cell," *J. Power Sources*, vol. 359, pp. 173–181, 2017.
- [62] D. E. Spahr, K. Friedrich, J. M. Schultz, and R. S. Bailey, "Microstructure and fracture behaviour of short and long fibre-reinforced polypropylene composites," *J. Mater. Sci.*, vol. 25, pp. 4427–4439, 1990.
- [63] I. V. Thorat, V. Mathur, J. N. Harb, and D. R. Wheeler, "Performance of carbon-fiber-containing LiFePO<sub>4</sub> cathodes for high-power applications," *J. Power Sources*, vol. 162, pp. 673–678, 2006.
- [64] A. K. Padhi, W. B. Archibald, K. S. Nanjundaswamy, and J. B. Godenough, "Ambient and High-Pressure Structures of LiMnVO<sub>4</sub> and Its Mn<sup>3+</sup>/Mn<sup>2+</sup> Redox Energy," *J. Solid State Chem.*, vol. 128, no. 2, pp. 267–272, 1997.
- [65] Y. Hu, M. M. Doeff, R. Kosteki, and R. Fiñones, "Electrochemical Performance of Sol-Gel Synthesized LiFePO<sub>4</sub> in Lithium Batteries," *J. Electrochem. Soc.*, vol. 151, no. 8, pp. 1279–1285, 2004.
- [66] N. Ravet, Y. Chouinard, J. F. Magnan, S. Besner, M. Gauthier, and M. Armand, "Electroactivity of natural and synthetic triphylite," *J. Power Sources*, vol. 97, pp. 503–507, 2001.
- [67] H. Huang, S.-C. Yin, and L. F. Nazar, "Approaching Theoretical Capacity of LiFePO<sub>4</sub> at Room Temperature at High Rates," *Electrochem. Solid-State Lett.*, vol. 4, no. 10, pp. 170–172, 2002.
- [68] S. S. Sekhon and H. P. Singh, "Ionic conductivity of PVdF-based polymer gel electrolytes," *Solid State Ionics*, vol. 152, pp. 169–174, 2002.
- [69] F. Font, B. Protas, G. Richardson, and J. M. Foster, "Binder migration during drying of lithium-ion battery electrodes: Modelling and comparison to experiment," *J. Power Sources*, vol. 393, pp. 177–185, 2018.
- [70] M. Stein, A. Mistry, and P. P. Mukherjee, "Mechanistic Understanding of the Role of Evaporation in Electrode Processing," *J. Electrochem. Soc.*, vol. 164, no. 7, pp. 1616–1627, 2017.
- [71] J. Xu *et al.*, "Characterization of the adhesive properties between structural battery electrolytes and carbon fibers," *Compos. Sci. Technol.*, vol. 188, p. 107962, Mar. 2020.
- [72] S. Leijonmarck, T. Carlson, G. Lindbergh, L. E. Asp, H. Maples, and A. Bismarck, "Solid polymer electrolyte-coated carbon fibres for structural and novel micro batteries," *Compos. Sci. Technol.*, vol. 89, pp. 149–157, Dec. 2013.

- [73] M. H. Kjell, T. G. Zavalis, M. Behm, and G. Lindbergh, "Electrochemical characterization of lithium intercalation processes of PAN-based carbon fibers in a microelectrode system," *J. Electrochem. Soc.*, vol. 160, no. 9, pp. 1473–1481, 2013.
- [74] J. F. Snyder, E. L. Wong, and C. W. Hubbard, "Evaluation of Commercially Available Carbon Fibers, Fabrics, and Papers for Potential Use in Multifunctional Energy Storage Applications," *J. Electrochem. Soc.*, vol. 156, no. 3, p. A215, 2009.
- [75] R. Kanno, Y. Takeda, T. Ichikawa, K. Nakanishi, and O. Yamamoto, "Carbon as negative electrodes in lithium secondary cells," *J. Power Sources*, vol. 26, no. 3, pp. 535–543, 1989.
- [76] S. J. Park and B. J. Kim, *Carbon fibers and their composites*. 2015.
- [77] F. Severini, L. Formaro, M. Pegoraro, and L. Posca, "Chemical modification of carbon fiber surfaces," *Carbon N. Y.*, vol. 40, no. 5, pp. 735–741, 2002.
- [78] M. Sharma, S. Gao, E. Mäder, H. Sharma, L. Y. Wei, and J. Bijwe, "Carbon fiber surfaces and composite interphases," *Compos. Sci. Technol.*, vol. 102, pp. 35–50, 2014.
- [79] E. Pérez-Pacheco, J. I. Cauich-Cupul, A. Valadez-González, and P. J. Herrera-Franco, "Effect of moisture absorption on the mechanical behavior of carbon fiber/epoxy matrix composites," *J. Mater. Sci.*, vol. 48, no. 5, pp. 1873–1882, Mar. 2013.
- [80] Sigma-Aldrich, "Poly(ethylene glycol) methyl ether methacrylate," *Merck KGaA*, 2019. [Online]. Available: <https://www.sigmaaldrich.com/catalog/product/aldrich/447943?lang=en&region=US>. [Accessed: 05-Oct-2020].
- [81] M. Willgert, M. H. Kjell, E. Jacques, M. Behm, G. Lindbergh, and M. Johansson, "Photoinduced free radical polymerization of thermoset lithium battery electrolytes," *Eur. Polym. J.*, vol. 47, no. 12, pp. 2372–2378, 2011.
- [82] S. Gabriel, R. Jérôme, and C. Jérôme, "Cathodic electrografting of acrylics: From fundamentals to functional coatings," *Prog. Polym. Sci.*, vol. 35, no. 1, pp. 113–140, 2010.
- [83] L. E. Asp, "Multifunctional composite materials for energy storage in structural load paths," *Plast. Rubber Compos.*, vol. 42, no. 4, pp. 144–149, May 2013.
- [84] C. Yang, X. Tian, T. Liu, Y. Cao, and D. Li, "3D printing for continuous fiber reinforced thermoplastic composites: Mechanism and performance," *Rapid Prototyp. J.*, vol. 23, no. 1, pp. 209–215, 2017.

- [85] J. Bruneaux, D. Therriault, and M. C. Heuzey, "Micro-extrusion of organic inks for direct-write assembly," *J. Micromechanics Microengineering*, vol. 18, pp. 1–10, 2008.
- [86] S. G. Hatzikiriakos and K. B. Migler, *Polymer processing instabilities: Control and understanding*. 2004.
- [87] G. Postiglione, G. Natale, G. Griffini, M. Levi, and S. Turri, "Conductive 3D microstructures by direct 3D printing of polymer/carbon nanotube nanocomposites via liquid deposition modeling," *Compos. Part A Appl. Sci. Manuf.*, vol. 76, pp. 110–114, 2015.
- [88] J. Xu, "Structural Composite Lithium-ion Battery: Effect of intercalation induced volumetric changes on micro-damage," Luleå University of Technology, 2019.
- [89] M. Park, X. Zhang, M. Chung, G. B. Less, and A. M. Sastry, "A review of conduction phenomena in Li-ion batteries," *J. Power Sources*, vol. 195, no. 24, pp. 7904–7929, 2010.
- [90] Y. Gao *et al.*, "Consecutive solvent evaporation and co-rolling techniques for polymer multilayer hollow fiber preform fabrication," *J. Mater. Res.*, 2006.
- [91] A. Thakur and X. Dong, "Additive manufacturing of 3D structural battery composites with coextrusion deposition of continuous carbon fibers," *Manuf. Lett.*, vol. 26, pp. 42–47, Oct. 2020.
- [92] K. W. Chew, T. C. Ng, and Z. H. How, "Conductivity and microstructure study of PLA-based polymer electrolyte salted with lithium perchloride, LiClO<sub>4</sub>," *Int. J. Electrochem. Sci.*, vol. 8, pp. 6354–6364, 2013.
- [93] K. W. Chew, "Development of Novel Bio-Degradable Electrolyte Based on Polylactide (PLA) for Lithium Rechargeable Battery," *Adv. Mater. Res.*, vol. 853, pp. 270–275, 2013.
- [94] A. Manuel Stephan and K. S. Nahm, "Review on composite polymer electrolytes for lithium batteries," *Polymer (Guildf.)*, vol. 47, no. 16, pp. 5952–5964, 2006.
- [95] R. Koksang, I. I. Olsen, and D. Shackle, "Review of hybrid polymer electrolytes and rechargeable lithium batteries," *Solid State Ionics*, vol. 69, pp. 320–335, 1994.
- [96] K. S. Ngai, S. Ramesh, K. Ramesh, and J. C. Juan, "A review of polymer electrolytes: fundamental, approaches and applications," *Ionics (Kiel)*, vol. 22, pp. 1259–1279, 2016.

- [97] C. V. Subba Reddy, M. Chen, W. Jin, Q. Y. Zhu, W. Chen, and S. Il Mho, "Characterization of (PVDF + LiFePO<sub>4</sub>) solid polymer electrolyte," *J. Appl. Electrochem.*, vol. 37, pp. 637–642, 2007.
- [98] E. Jacques, M. H. Kjell, D. Zenkert, G. Lindbergh, M. Behm, and M. Willgert, "Impact of electrochemical cycling on the tensile properties of carbon fibres for structural lithium-ion composite batteries," *Compos. Sci. Technol.*, vol. 72, no. 7, pp. 792–798, 2012.
- [99] J. Vetter *et al.*, "Ageing mechanisms in lithium-ion batteries," *J. Power Sources*, vol. 147, no. 1–2, pp. 269–281, Sep. 2005.
- [100] J. Hagberg, S. Leijonmarck, and G. Lindbergh, "High Precision Coulometry of Commercial PAN-Based Carbon Fibers as Electrodes in Structural Batteries," *J. Electrochem. Soc.*, vol. 163, no. 8, pp. 1790–1797, 2016.
- [101] Toray, "Toray Industries, Inc." [Online]. Available: <https://www.torayca.com/en/download/pdf/torayca.pdf>. [Accessed: 09-Oct-2020].
- [102] Sigma-Aldrich, "Poly(vinylidene fluoride)," *Merck KGaA*, 2020. [Online]. Available: <https://www.sigmaaldrich.com/catalog/product/aldrich/182702?lang=en&region=US>. [Accessed: 05-Oct-2020].
- [103] ThermoFischer Scientific, "Carbon black, Super P," *Alfa Aesar*, 2020. .
- [104] Sigma-Aldrich, "Lithium iron(II) phosphate." .
- [105] M. Luo, X. Tian, J. Shang, W. Zhu, D. Li, and Y. Qin, "Impregnation and interlayer bonding behaviours of 3D-printed continuous carbon-fiber-reinforced poly-ether-ether-ketone composites," *Compos. Part A Appl. Sci. Manuf.*, vol. 121, pp. 130–138, Jun. 2019.

## SECTION

### 2. CONCLUSIONS AND RECOMMENDATIONS

This research focuses on the fabrication and characterization of multifunctional composites using carbon fiber reinforcement. Coextrusion based additive manufacturing techniques were simultaneously developed to shorten the design manufacturing cycle, reduce production costs and improve competitiveness through flexible, tool-less, and mold-less fabrication of the structures using the proposed multifunctional composites.

The first part of this research focused on improving the mechanical properties of the composites through carbon fiber inclusions. In Paper I, a fabrication process that enables manufacturing of ceramic composites with precision placement of microscopic carbon fiber inclusions was introduced. This capability facilitates manufacturing of composite specimens with different patterns (and spacing) of inclusion arrays to tailor the overall toughness and fracture pathways within the inherently strong but brittle ceramics. A closed-form analytical model for the mixed-mode stress intensity factor in a composite with selected inclusion arrangements was also presented. This model, with the help of fracture initiation calculations, expedites the analysis for various composite designs, approximating crack propagation with computational efficiency with minimal loss in accuracy. The prediction of fracture propagation was validated using a phase-field model, as well as a 4-point bending experiment. Accelerated analyses and consequent inclusion motif optimization has facilitated designing and fabrication of high-strength and high-

toughness ceramic composites with quasi-predictable mechanical behavior, having specialized applications in automotive and aerospace industry.

In Paper II, an extrusion deposition based additive manufacturing approach to enable customized, cost-effective fabrication of high-performance polymers with high strength, high modulus reinforcing carbon fibers was presented. A high deposition rate was achieved by the implementation of a single-screw extruder, which directly uses thermoplastic pellets and continuous fiber tows as feedstock materials. The feasibility of the extrusion deposition additive manufacturing approach to fabricate short fiber reinforced (SFRC), long fiber reinforced (LFRC) and continuous fiber reinforced (CFRC) thermoplastic composites was also conducted by printing fiber reinforced composite samples and was further demonstrated by fabricating large-volume components with complex geometries. These samples were compared against their pure thermoplastic counterpart through the microstructural analyses and mechanical testing, with SFRC, LFRC, and CFRC reporting flexural strength increment of 11%, 28%, and 52%, respectively, compared to the pure thermoplastic specimen. With capabilities to 3D print at high deposition rate (up to 0.8 kg/hr) and low material costs (<\$10/kg), the result of this study can potentially be used as a guidance in design and fabrication of large-volume fiber reinforced structural components of high strength to be used in aerospace, automotive, and other industries.

In the second part of this research, the component level strength-to-weight improvement that was achieved via carbon fiber reinforced composites, was elevated to the system level performance-to-weight improvement by formulating and constructing multifunctional composites. Structural energy composites were investigated as a

technology to potentially replace auxiliary power systems, simultaneously catering electrical and structural requirements. Using contemporary additive manufacturing techniques, customized to fit battery form factors superseding the archetypal compromise between the mechanical and electrical performance in polymer structural batteries were designed and manufactured. In Paper III, the multi-axis extrusion deposition process that was developed to 3D print continuous fiber reinforced thermoplastic composites was permuted to print 3D structural battery composites with continuous carbon fibers coated by solid polymer electrolyte (SPE). The SPE-coated carbon fibers were coextruded with cathode doped thermoplastic matrix materials to 3D print complex structural battery composites capable of simultaneous load bearings while working as batteries to store electrical energy. In Paper IV, a new printing method for multifunctional composites with 3D continuous carbon fibers via UV-assisted coextrusion deposition was demonstrated. Using this approach, continuous carbon fibers could be simultaneously deposited with doped functional photopolymer resin, subsequently rapidly cured by an ultraviolet laser. The technique allowed for direct printing of free-standing compliant carbon fiber reinforced composite structures and composites with conductive channeling. In particular, a novel functional, full lithium-ion structural battery was successfully printed in one single step, with each coated carbon fiber acting as a micro-battery cell. The electrochemical as well as the mechanical properties of the structural battery composites with polymer cathode and 3D continuous carbon fiber anode is largely dictated by the extent of integration of cathode matrix within the reinforcing carbon fiber anode, and by the solid load (active-conductive material) content within the cathode matrix. Thermoplastic cathode matrix allows addition of large volume of solid load. However, its

permeability within the carbon fiber anode tow is hampered due to the viscous nature of the thermoplastic binder. UV curable thermoset cathode matrix allow excellent permeability and consequently, improved contact between the polymer cathode and SPE coated carbon fiber anode. However, exceeding certain volume of solid load in the matrix renders it incurable using U.V. laser. Therefore, in Paper V, a thermoplastic fluoro polymer (polyvinylidene fluoride PVDF) was used as a binder to prepare cathode matrix for the additively manufactured structural energy composites. Use of PVDF as a binder allowed incorporation of large volume of solid load within the cathode matrix, without compromising with its permeability or curing process. A cathode slurry prepared by mixing the solid load (active material, conductive material and PVDF binder) in Dimethylformamide (DMF) solvent was coextruded with the SPE coated continuous carbon fibers to deposit full-cell composition, fabricating a complete lithium-ion structural battery in single deposition. Microstructural analyses was conducted to investigate the effect of cathode slurry viscosity and composition on the electrochemical and mechanical performance of the energy composites. The proposed process yields structural energy composites with excellent mechanical and electrochemical properties with added benefit of customizability facilitated by 3D printing. Thus, establishing the potential of the proposed method to directly print functional structural energy composites aimed to provide mass-less energy storage for electrically powered structural systems, especially in aerospace, automotive and consumer electronic applications where large capacities and low weights are desired.

The research presented in this dissertation can be extended in several ways. Although, the electrochemical properties of the structural energy composites are

significantly elevated by the use of PVDF as binder within the cathode matrix, the PVDF binder itself has inherently weak flexural properties. By incorporating ceramic electrolyte within the composite composition, this compromise could potentially be addressed. Use of superior conductive dopants like graphene, carbon nanotubes and MXene, instead of carbon black and short carbon fibers could help in further improving the electrochemical performance of the proposed multifunctional composite without requiring excessive amounts of dopants that are proven to be detrimental to the mechanical properties of the cathode matrix. Carbon fiber electrodes have illustrated capabilities to potentially allow piezo-electrochemical energy harvesting due to lithium-intercalation. This property could be further explored through our proposed multifunctional composite that unlike typical pouch cells, are capable of simultaneous load bearing and energy storage.

**BIBLIOGRAPHY**

- [1] B. K. Donaldson, *Analysis of Aircraft Structures*. Cambridge: Cambridge University Press, 2008.
- [2] M. Mehdikhani, L. Gorbatikh, I. Verpoest, and S. V. Lomov, “Voids in fiber-reinforced polymer composites: A review on their formation, characteristics, and effects on mechanical performance,” *J. Compos. Mater.*, vol. 53, no. 12, pp. 1579–1669, May 2019.
- [3] A. Lendlein and R. S. Trask, “Multifunctional materials: concepts, function-structure relationships, knowledge-based design, translational materials research,” *Multifunct. Mater.*, vol. 1, no. 1, p. 010201, Aug. 2018.
- [4] H. Gao, B. Ji, I. L. Jager, E. Arzt, and P. Fratzl, “Materials become insensitive to flaws at nanoscale: Lessons from nature,” *Proc. Natl. Acad. Sci.*, vol. 100, no. 10, pp. 5597–5600, May 2003.
- [5] R. O. Ritchie, M. J. Buehler, and P. Hansma, “Plasticity and toughness in bone,” *Phys. Today*, vol. 62, no. 6, p. 41, 2009.
- [6] K. Gall, M. Mikulas, N. A. Munshi, F. Beavers, and M. Tupper, “Carbon fiber reinforced shape memory polymer composites,” *J. Intell. Mater. Syst. Struct.*, vol. 11, no. 11, pp. 877–886, Nov. 2000.
- [7] A. Kelly and C. Zweben, “Comprehensive composite materials,” *Mater. Today*, 1999.
- [8] E. T. Thostenson, W. Z. Li, D. Z. Wang, Z. F. Ren, and T. W. Chou, “Carbon nanotube/carbon fiber hybrid multiscale composites,” *J. Appl. Phys.*, vol. 91, no. 9, pp. 6034–6037, May 2002.
- [9] J. F. Snyder, E. L. Wong, and C. W. Hubbard, “Evaluation of commercially available carbon fibers, fabrics, and papers for potential use in multifunctional energy storage applications,” *J. Electrochem. Soc.*, vol. 156, no. 3, p. A215, 2009.
- [10] J. P. Lewicki *et al.*, “3D-printing of meso-structurally ordered carbon fiber/polymer composites with unprecedented orthotropic physical properties,” *Sci. Rep.*, vol. 7, p. 43401, Mar. 2017.
- [11] D. D. L. Chung, *Carbon Fiber Composites*. Elsevier, 1994.
- [12] S. Chand, “Carbon fibers for composites,” *J. Mater. Sci.*, vol. 35, pp. 1303–1313, 2000.

- [13] Y. Liu, B. Zwingmann, and M. Schlaich, "Carbon Fiber reinforced polymer for cable Structures - A Review," *Polymers (Basel)*, vol. 7, no. 10, pp. 2078–2099, Oct. 2015.
- [14] T. Hofstätter, D. B. Pedersen, G. Tosello, and H. N. Hansen, "State-of-the-art of fiber-reinforced polymers in additive manufacturing technologies," *J. Reinf. Plast. Compos.*, vol. 36, no. 15, pp. 1061–1073, Aug. 2017.
- [15] P. Parandoush and D. Lin, "A review on additive manufacturing of polymer-fiber composites," *Compos. Struct.*, vol. 182, pp. 36–53, Dec. 2017.
- [16] X. Wang, M. Jiang, Z. Zhou, J. Gou, and D. Hui, "3D printing of polymer matrix composites: A review and prospective," *Compos. Part B Eng.*, vol. 110, pp. 442–458, Feb. 2017.
- [17] R. Danzer, "A general strength distribution function for brittle materials," *J. Eur. Ceram. Soc.*, vol. 10, no. 6, pp. 461–472, Jan. 1992.
- [18] A. G. Evans and S. M. Wiederhorn, "Proof testing of ceramic materials: an analytical basis for failure prediction," *Int. J. Fract.*, vol. 26, no. 4, pp. 355–368, Dec. 1984.
- [19] C. E. Duty *et al.*, "Structure and mechanical behavior of Big Area Additive Manufacturing (BAAM) materials," *Rapid Prototyp. J.*, vol. 23, no. 1, pp. 181–189, Jan. 2017.
- [20] B. Huang and S. Singamneni, "Raster angle mechanics in fused deposition modelling," *J. Compos. Mater.*, vol. 49, no. 3, pp. 363–383, Feb. 2015.
- [21] S. S. Sekhon and H. P. Singh, "Ionic conductivity of PVDF-based polymer gel electrolytes," *Solid State Ionics*, vol. 152, pp. 169–174, 2002.

## VITA

Aditya Raghvendra Thakur was born in Maharashtra, India. He enrolled for Bachelor of Engineering degree at Coventry University, United Kingdom in 2010 and graduated in 2013 securing BEng (Hons.) Aerospace Technology with a First Class. In 2015, he completed his Master of Science from Cranfield University, United Kingdom in Aerospace Vehicle Design specializing in Aircraft Design. During his masters he conducted research in the area of Unmanned Aerial Vehicles (UAV) and wrote a thesis on Ultra Long Range UAV Systems Development.

Aditya enrolled for his Ph.D. in Aerospace Engineering in Fall 2016 at Missouri University of Science and Technology in United States of America. With Dr. Charles S. Wojnar, he focused on research dedicated towards ceramic toughening via engineering heterogeneity. In Spring 2019, Aditya commenced his research with Dr. Xiangyang Dong with the focus on additive fabrication and characterization of fiber reinforced multifunctional composites, upon which he based his dissertation. With preliminary focus on 3D printing of carbon fiber reinforced polymers, his research promptly evolved into additive manufacturing of structural energy composites with 3D continuous carbon fiber reinforcement. This study laid the foundation for the 3D printing of functional structural lithium-ion batteries. Aditya also actively participated in the study investigating laser direct deposition of ceramics with Dr. Dong.

Aditya received his Ph.D. in Aerospace Engineering from Missouri University of Science and Technology in December 2020.